Optimization of Heat Sinks with Flow Bypass Using Entropy Generation Minimization

by

MD RAKIB HOSSAIN

A thesis
presented to the University of Waterloo
in fulfilment of the
thesis requirement for the degree of
Master of Applied Science
in
Mechanical Engineering

Waterloo, Ontario, Canada, 2006

I hereby declare that I am the sole author of this thesis. This is a true copy of the thesis, including any required final versions, as accepted by my examiners.

I understand that my thesis may be made electronically available to the public.

Md Rakib Hossain

Abstract

Forced air cooling of electronic packages is enhanced through the use of extended surfaces or heat sinks that reduce boundary resistance allowing heat generating devices to operate at lower temperatures, thereby improving reliability. Unfortunately, the clearance zones or bypass regions surrounding the heat sink, channel some of the cooling air mass away from the heat sink, making it difficult to accurately estimate thermal performance. The design of an "optimized" heat sink requires a complete knowledge of all thermal resistances between the heat source and the ambient air, therefore, it is imperative that the boundary resistance is properly characterized, since it is typically the controlling resistance in the path. Existing models are difficult to incorporate into optimization routines because they do not provide a means of predicting flow bypass based on information at hand, such as heat sink geometry or approach velocity.

A procedure is presented that allows the simultaneous optimization of heat sink design parameters based on a minimization of the entropy generation associated with thermal resistance and fluid pressure drop. All relevant design parameters such as geometric parameters of a heat sink, source and bypass configurations, heat dissipation, material properties and flow conditions can be simultaneously optimized to characterize a heat sink that minimizes entropy generation and in turn results in a minimum operating temperature of an electronic component.

An analytical model for predicting air flow and pressure drop across the heat sink is developed by applying conservation of mass and momentum over the bypass regions and in the flow channels established between the fins of the heat sink. The model is applicable for the entire laminar flow range and any type of bypass (side, top or side and top both) or fully shrouded configurations. During the development of the model, the flow was assumed to be steady, laminar, developing flow. The model is also correlated to a simple equation within $\pm 8\%$ confidence level for an easy implementation into the entropy generation minimization procedure. The influence of all the resistances to heat transfer associated with a heat sink are studied, and an order of magnitude analysis is carried out to include only the influential resistances in the thermal resistance model. Spreading and material resistances due to the geometry of the base plate, conduction and convection resistances associated with the fins of the heat sink and convection resistance of the wetted surfaces of the base plate are considered for the development of a thermal resistance model. The thermal resistance and pressure drop model are shown to be in good agreement with the experimental data over

a wide range of flow conditions, heat sink geometries, bypass configurations and power levels, typical of many applications found in microelectronics and related fields. Data published in the open literature are also used to show the flexibility of the models to simulate a variety of applications.

The proposed thermal resistance and pressure drop model are successfully used in the entropy generation minimization procedure to design a heat sink with bypass for optimum dimensions and performance. A sensitivity analysis is also carried out to check the influence of bypass configurations, power levels, heat sink materials and the coverage ratio on the optimum dimensions and performance of a heat sink and it is found that any change in these parameters results in a change in the optimized heat sink dimensions and flow conditions associated with the application for optimal heat sink performance.

Acknowledgement

Through out my stay at University of Waterloo, I have been lucky to be a member of the Microelectronics Heat Transfer Laboratory (MHTL). I would like to thank my supervisor Professor J. Richard Culham for giving me the opportunity to work in MHTL, and funding my research throughout my time at MHTL. He gave me the freedom and the encouragement to pursue my own ideas and to manage my own research. His guidance, advice and assistance were invaluable during the course of this work.

I want to thank Professor M. Michael Yovanovich for providing necessary advice whenever needed. He is an incredible source of knowledge and provided excellent guidance on technical details.

People in the MHTL made it a great place to work. In particular Dr. Peter M. Teertstra deserves to be appreciated for his help in experimental setup, data acquisition software development and constructive discussions. I would also like to thank all of the individuals at the MHTL whose assistance and encouragement helped along the way.

I would also like to express my gratitude to Alan Hodgson of Thermal and Fluid Laboratory, John Potzold and John Dobrowski of Student Shop for their cooperation during the preparation of the experimental setup.

People of the Engineering Machine Shop deserve to be credited for their fine craftsmanship in constructing components for the experimental test apparatus.

I would like to thank my parents for their support, encouragement and prayer during this course of time.

Finally, I would like to thank my wife Fouzia and daughter Zarrin for their patience and many sacrifices during this selfish endeavor.

Dedication

For my life, I owe to my parents;

For my knowledge, I owe to my teachers.

Contents

List of Figures

List of Tables

Nomenclature

Symbol	Name	SI Unit
Alphabet- Upper Case		
A_b	area of the bypass	m^2
A_{be}	exposed surface area of the baseplate for heat transfer	m^2
A_{bp}	area of the baseplate	m^2
A_{bs}	area of the side bypass	m^2
A_{bt}	area of the top bypass	m^2
A_{cf}	cross-sectional area of a fin for conduction	m^2
A_{1ch}	frontal area of one channel	m^2
A_{ch}	frontal channel area	m^2
A_d	flow area of the duct	m^2
A_f	virtual heat transfer area of a fin (=$H_c \times L$)	m^2
A_{sh}	heat source area	m^2
A_t	total convection heat transfer area of a heat sink	m^2
B	heat sink foot print width	m
Bi	Biot number	$-$
CB	duct width	m
CH	duct height	m
C_D	dimensionless pressure drop	$-$
C_p	specific heat	$J/kg \cdot K$
$D_{h_{bs}}$	side bypass hydraulic diameter	m
$D_{h_{bt}}$	top bypass hydraulic diameter	m
$D_{h_{ch}}$	channel hydraulic diameter	m
D_{h_d}	duct hydraulic diameter	m
H	fin height	m
H_c	virtual fin height for assumption of adiabatic fin tip	m
I	current	amp
K_c	channel contraction coefficient	$-$
K_e	channel expansion coefficient	$-$

Symbol	Name	SI Unit
Alphabet- Upper Case$\cdots$ continued		
L	heat sink foot print length	m
L^*	dimensionless length	$-$
L^*_{ch}	channel dimensionless length	$-$
L^*_{bs}	side bypass dimensionless length	$-$
L^*_{bt}	top bypass dimensionless length	$-$
N	number of fins	$-$
Nu_s	Nusselt number using s as characteristic length	$-$
P_1	channel inlet pressure	N/m^2
P_2	channel outlet pressure	N/m^2
P_c	channel contraction pressure drop	N/m^2
P_e	channel expansion pressure drop	N/m^2
P_f	channel frictional pressure drop	N/m^2
Pr	Prandtl number	$-$
Q	heat input	W
R_{th}	total thermal resistance	K/W
R_{hs}	thermal resistance of a heat sink	K/W
R_j	heat sink joint resistance	K/W
R_s	base plate spreading resistance	K/W
R_m	base plate material resistance	K/W
R_c	fin contact resistance	K/W
R_{fin}	fin resistance	K/W
R_{film}	film resistance	K/W
Re_{bs}	Reynolds number of side bypass	$-$
Re_{bt}	Reynolds number of top bypass	$-$
Re_{ch}	channel Reynolds number	$-$
Re_d	duct Reynolds number	$-$
Re_s	Reynolds number using s as characteristic length	$-$

Symbol	Name	SI Unit
Alphabet- Upper Case· · · · continued		
V	voltage	$volt$
V_b	bypass velocity	m/s
V_{ch}	channel velocity	m/s
V_d	duct velocity	m/s
T_a	ambient temperature	K
T_b	base plate temperature	K
Alphabet- lower Case		
a	half-length of heat source	m
a_0	bypass area ratio	$-$
a_{ch}	channel area ratio	$-$
a_{hs}	heat sink area ratio	$-$
b	half-width of heat source	m
c	half-length of a heat sink	m
d	half-width of a heat sink	m
f	Fanning friction coefficient	$-$
f_{app}	apparent friction factor	$-$
$f_{app_{ch}}$	apparent friction factor for channel	$-$
$f_{app_{bs}}$	apparent friction factor for side bypass	$-$
$f_{app_{bt}}$	apparent friction factor for top bypass	$-$
h	convection heat transfer coefficient	$W/m^2 \cdot K$
k	thermal conductivity of a heat sink material	$W/m \cdot K$
k_f	thermal conductivity of cooling fluid or air	$W/m \cdot K$
m, n	indices for summation	$-$
$\dot{m}_{ch}$	mass flow rate through the channel	kg/s
s	fin spacing	m
t	fin thickness	m
t_b	base plate thickness	m
u_{ch}	dimensionless channel velocity	$-$

Symbol	Name	SI Unit
Greek		
α	aspect ratio	–
α_{ch}	channel aspect ratio	–
α_{bs}	side bypass aspect ratio	–
α_{bt}	top bypass aspect ratio	–
β	eigenvalues, $(\sqrt{\delta^2+\lambda^2})$	–
α	aspect ratio	–
α_{ch}	channel aspect ratio	–
α_{bs}	side bypass aspect ratio	–
α_{bt}	top bypass aspect ratio	–
β	eigenvalues, $(\sqrt{\delta^2+\lambda^2})$	–
δ	eigenvalues, $(m\pi/c)$	–
ε	relative contact size	–
ζ	eigenvalue, $(\zeta=\beta=\delta=\lambda)$	–
η_f	fin efficiency	–
η_0	overall efficiency of a heat sink	–
θ_b	differential temperature between base plate and ambient	K
λ	eigenvalues, $(n\pi/d)$	–
μ	viscosity of air	$kg/m\cdot s$
ρ	density of air	kg/m^3
σ	fraction of frontal free flow area of channel	–
τ	dimensionless base plate thickness	–
τ_w	wall shear stress	N/m^2
ϕ	spreading functions	–
ψ	dimensionless spreading resistance	–

Symbol	Name	SI Unit
Other		
ℓ	heat source length	m
ω	heat source width	m
$\forall$	volume flow rate	m^3/s
ΔP_b	pressure drop across bypass region	N/m^2
ΔP_{b_s}	pressure drop across side bypass region	N/m^2
ΔP_{b_t}	pressure drop across top[bypass region	N/m^2
ΔP_{hs}	pressure drop across heat sink	N/m^2
$\mathcal{P}_d$	duct perimeter	m
$\mathcal{P}_{ch}$	channel perimeter	m
$\mathcal{P}_{bs}$	perimeter of side bypass	m
$\mathcal{P}_{bt}$	perimeter of top bypass	m
$\mathcal{P}_f$	perimeter of one fin based on x-sectional area of one fin	m
$\mathcal{L}$	arbitrary length scale	m
$\mathcal{S}_{gen}$	entropy generation	W/K
$\mathcal{S}_f$	hydrodynamic entropy generation	W/K
$\mathcal{S}_t$	thermal entropy generation	W/K

Subscript

Symbol	Name	Symbol	Name
$1ch$	one channel	d	duct
a	ambient	e	expansion
app	apparent	f	friction
b	bypass	hs	heat sink
be	exposed base	j	joint
bp	baseplate	m	material
bs	side bypass	O	overall
bt	top bypass	P	package
c	contraction	s	spreading
ch	channel	t	total

Chapter 1

Introduction

Thermal management of electronic components has been one of the primary areas of focus in advanced heat transfer research and development. This has been especially true in the evolution of microelectronics over the past several decades. Heat transfer behavior is complex, as heat is dissipated in the chip, conducted into the substrate and then transferred to the surroundings by some combination of thermal conduction, convection and radiation. The increase of power density in microelectronic packages has underlined the need for employing effective cooling devices and cooling methods to maintain the operating temperatures of electronic components at a satisfactory level.

1.1 Background

Heat removal from Integrated Circuits (ICs) now ranks among the major technical problems that needs to be solved to achieve higher power densities. For years, the IC industry has been trying to maintain the pace of Moore's prediction, the projection that the number of transistors on integrated circuits would double every eighteen months. Figure 1.1 shows the prediction of the growth of semiconductor transistor density, observed by Intel founder Dr. Gordon Moore. This remarkable rate of advancement has resulted in smaller feature sizes and improved manufacturing techniques, which allow for more efficient circuit designs and materials, that result in better circuit performance.

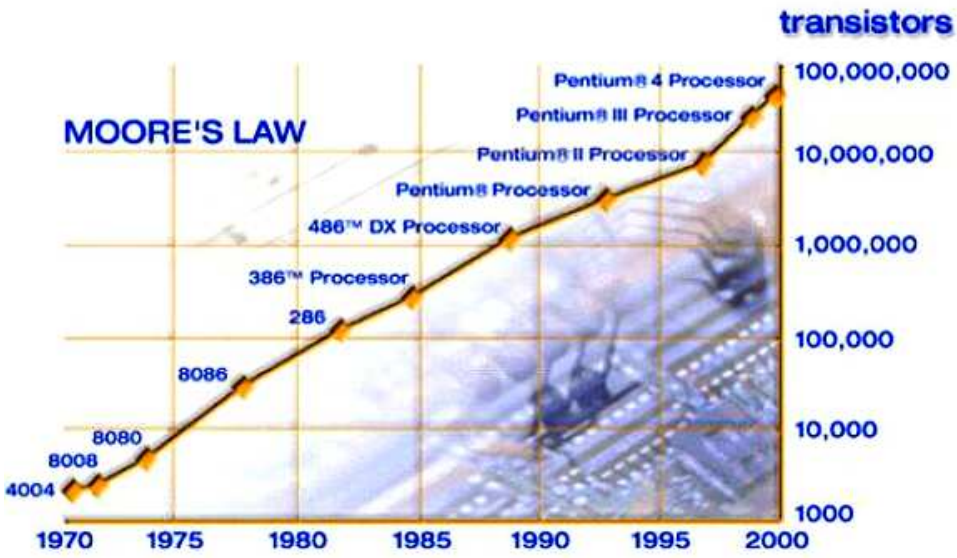

Figure 1.1: Time-line Plot of Transistor Counts on Intel Processors Based on Moore's Prediction [23]

As semiconductors become more complex and new milestones in transistor size and performance are achieved, power consumption and heat dissipation have emerged as limiting factors to the continued pace of new chip designs and manufacturing techniques. There are hundreds of millions, and even billions of smaller and faster transistors which are packed on to a processor, a single piece of silicon the size of a thumbnail. The power consumption and dissipation of heat generated in the processor core become significant technical challenges to the achievement of Moore's prediction. Power and heat have become the biggest technical issue of the decade while the semiconductor industry continues to strive to improve transistor speed and power efficiency.

Forced air cooling through the use of extended surfaces [Fig. 1.3] is being used as a viable technique for cooling microelectronic devices due to its inherent simplicity and cost effectiveness. Designs incorporating such surfaces typically take the form of finned heat sinks. In microelectronic applications, heat sinks are directly mounted on the cases that enclose microelectronic devices to provide extra surface area for heat transfer from the device to the cooling fluid [Fig. 1.2]. However, with the increase in component density within electronic enclosures, combined with ongoing increases in individual component power dissipation, it is apparent that the use of ducting for individual component cooling is not practical. If forced-air heat sinks are going to continue to

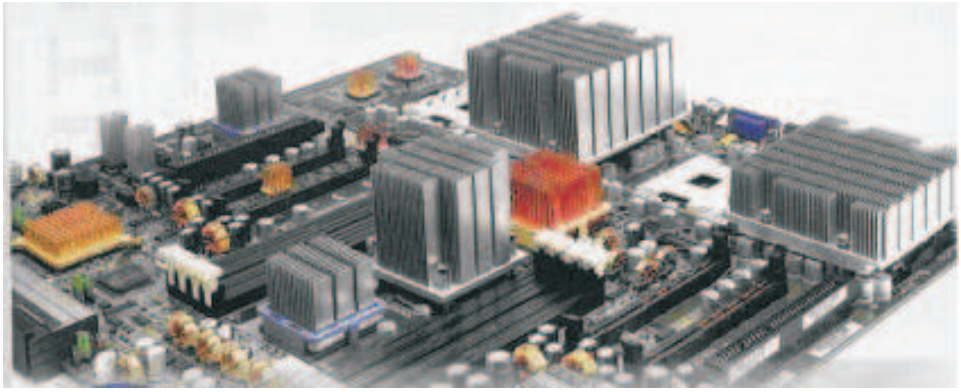

Figure 1.2: Application of Heat Sinks in an Electronic Enclosure [5]

be an effective means of cooling these devices, the thermal engineer must examine more closely the relationship between thermal performance and flow in and around the heat sink.

Heat sinks use a variety of fin arrangements to provide the extra surface area for heat transfer. The presence of closely spaced fins also creates an extra resistance for flow through the heat sinks. In many practical applications, heat sinks are mounted on circuit boards such that there are significant clearances around them [Fig. 1.2]. Because of the higher resistance to flow through a heat sink, the cooling fluid tends to bypass the heat sink and flow through the clearance zones. Since the temperature rise across the heat sink and the heat transfer coefficient depends on the velocity of the flow through the heat sink, the bypassing of the flow adversely affects the heat transfer performance of a heat sink. When the air velocity between the fins of such a heat sink can be well approximated, the thermal engineer can effectively predict the overall thermal resistance and viscous dissipation of the system. Approximating the fin velocity based on the upstream flow rate in the enclosure is often difficult, except in the case of fully shrouded heat sinks. All other ducting scenarios require consideration of flow bypass. Therefore, accurate system-specific analysis of the effect of bypass on the thermal performance of heat sinks is important for satisfying current thermal requirements as well as providing the capability for designing thermal solution for future generation of electronic hardware.

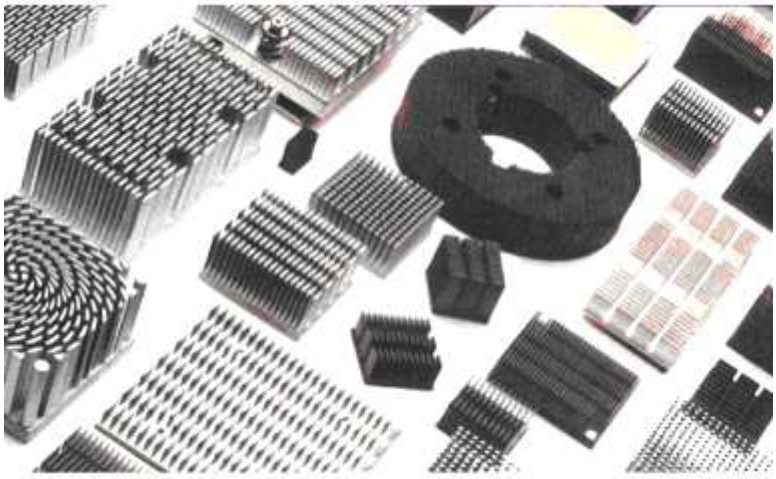

Figure 1.3: Different Types of Extended Surfaces or Heat Sinks [6]

1.2 Problem Statement

The heat produced in an electronic device is conducted into the substrate and then transferred by some combination of thermal conduction, convection and radiation to the outer surface through numerous components such as thermal interface materials (TIMs), heat sinks, air etc. [Fig. 1.4]. Along this flow path, heat encounters various thermal resistances that cause a temperature rise inside the package. Therefore, careful design of heat sinks is extremely important in order to maintain operating temperatures at or below recommended limits.

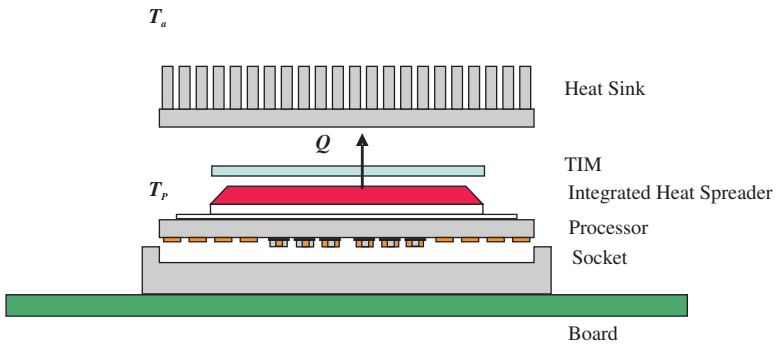

Figure 1.4: Microelectronics Package with Heat Sink

1.2.1 Thermal Resistance in Heat Sinks

Heat sinks are typically designed based on a measure of thermal resistance to heat flow between the heat source and the surrounding cooling medium.

$$R_{th} = \frac{T_P - T_a}{Q} = \frac{\theta_P}{Q} \tag{1.1}$$

where T_P is the package temperature, and θ_P is the temperature access of the package with respect to ambient temperature, T_a for a heat input of Q.

R_{th} can be obtained from a resistor network [Fig. 1.5] formed between the heat source and the cooling medium.

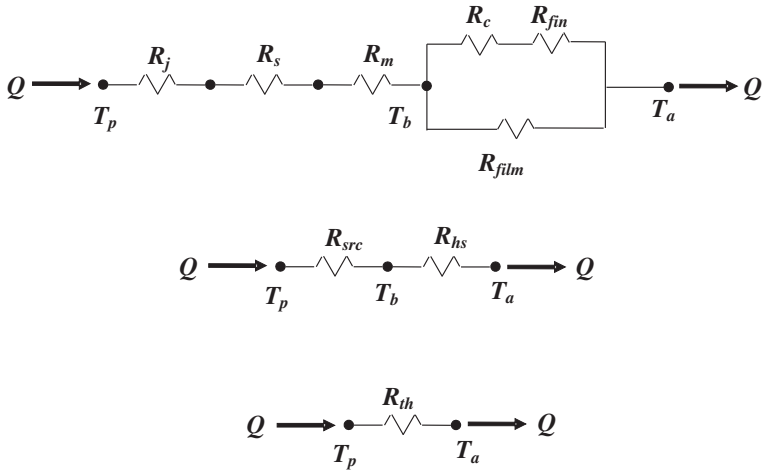

Figure 1.5: Thermal Resistance Network

R_{th} can also be written in the following form:

$$R_{th} = R_{src} + R_{hs}$$

where R_{src} is the resistance between the package and heat sink base and expressed as:

$$R_{src} = R_j + R_s + R_m$$

and R_{hs} is the resistance associated with heat sink fins and exposed surface of the base plate, can be expressed as:

$$R_{hs} = \frac{1}{\frac{N}{R_c + R_{fin}} + \frac{1}{R_{film}}}$$

Thermal Joint Resistance, R_j: The predominant heat flow in a heat sink is by conduction from the source, through the base plate and into the fins, where heat is dissipated to the surrounding by convection. During this process, heat encounters a thermal resistance called joint resistance, R_j because of the surface irregularities between the two adjoining surfaces, and this resistance can be minimized by the use of a Thermal Interface Material (TIM).

Spreading Resistance, R_s: If the package surface area is smaller than the heat sink base area, heat flux spreads as the heat is conducted away from the smaller source area to the larger base area and encounters a thermal resistance called spreading resistance, R_s.

Material Resistance, R_m: The bulk resistance of the material depends on the thermal properties of the base material and the geometry of the base. It can be explained by Fourier's Law of Conduction.

$$R_m = \frac{t_b}{kA_b}$$

where A_b is the cross-sectional flow area, and t_b is the length of the flow path.

Fin Contact Resistance, R_c: If fins are machined as an integral part of the base plate from which they extend, there is no contact resistance at their base. However, more commonly, fins are manufactured separately and are attached to the wall by a metallurgical or adhesive joint. In such cases, there exists a thermal contact resistance, R_c, which may adversely influence overall thermal performance.

Fin Resistance, R_{fin}: Heat is carried out from the base through the fin by conduction and dissipated to the surrounding ambient air by convection. During this process, heat flow encounters a thermal resistance, called fin resistance, because of fin material, geometry, and the convection heat transfer coefficient of the surrounding fluid. R_{fin} is in series with R_c [Fig. 1.5].

Film Resistance, R_{film}: Convection heat transfer from the exposed surface of the base plate also encounters a thermal resistance, called film resistance, R_{film}, because of the convection heat transfer coefficient over the base plate.

The parallel resistance formed between R_c and R_{fin}, and R_{film} is known as heat sink resistance, R_{hs}. The largest and consequently the controlling thermal resistance in the path between the source and the sink is usually R_{hs} [Table D.2]. R_{hs} can account for almost 90% of the total resistance and it depends on the convective heat transfer coefficient (h) inside and over the heat sink. h depends

on the amount of air flowing through the heat sink and is given by the following non-dimensional expression:

$$Nu_{ch} = \frac{hD_{h_{ch}}}{k} = aRe_{ch}^{b}Pr^{c} \tag{1.2}$$

Pr and k_f are the thermophysical properties of the cooling fluid and may vary with the temperature. But in microelectronics, the range of operating temperature is relatively low, and for the low range of temperature, thermophysical properties of the cooling fluid can be assumed constant. $D_{h_{ch}}$ depends on the geometry of a heat sink, therefore, h can be expressed as:

$$h = f(Re_{ch}) \tag{1.3}$$

$$Re_{ch} = f(\rho, V_{ch}, D_{h_{ch}}, \mu)$$

ρ and μ are the thermophysical properties of the cooling fluid, therefore, h can be expressed as:

$$h = f(V_{ch}) \tag{1.4}$$

From Eqs. 1.2 and 1.4, it is clear that an increase in the velocity between the fins could potentially enhance the convective heat transfer coefficient. Accurate prediction of flow between the fins is very important in order to achieve the desired convective heat transfer coefficient. Approximating the fin velocity based on the upstream flow rate in the enclosure is often difficult, except in the case where the heat sink is fully shrouded [Fig. 1.6]. When there is no clearance around the heat sink, the flow velocity through the fins is known from the duct flow mean approach velocity by applying conservation of mass. The use of such a duct is known to minimize the bypass of air around the heat sink, but results in a considerable pressure drop penalty. A higher pressure drop and subsequently the higher pumping power required to push the air through the heat sink restricts the use of high performance heat sinks in industry. Though a higher pumping power may be achieved by using a high power fan, it is often difficult to have the necessary ducting in an electronic enclosure, therefore, use of ducting for individual component cooling is not practical. In addition, noise constraints associated with many electronics applications restrict approach flow velocities to a range of $8 m/s$ or less.

Typically, the heat sink on an electronic module occupies only a fraction of the cross-section of the air flow channel of the card as shown in Fig. 1.7. The air flow areas that exist around the heat sink allow some of the on coming air flow to bypass the heat sink. A flow network model for a heat

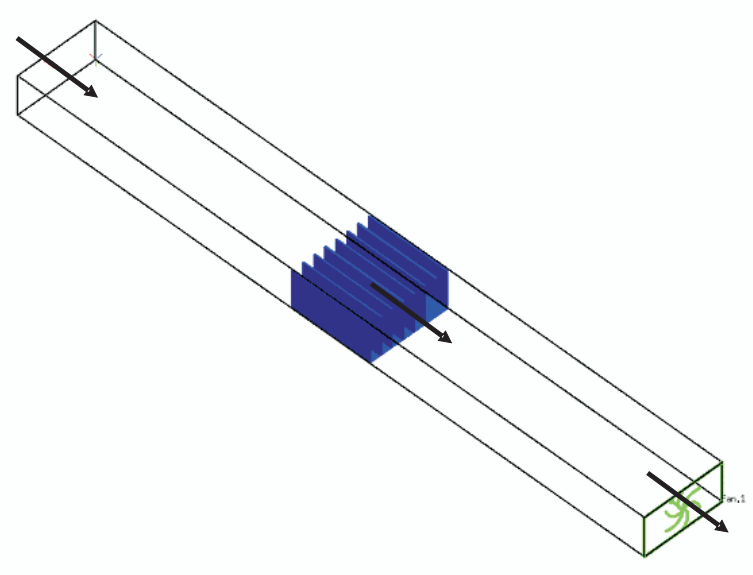

Figure 1.6: Fully Shrouded Heat Sink

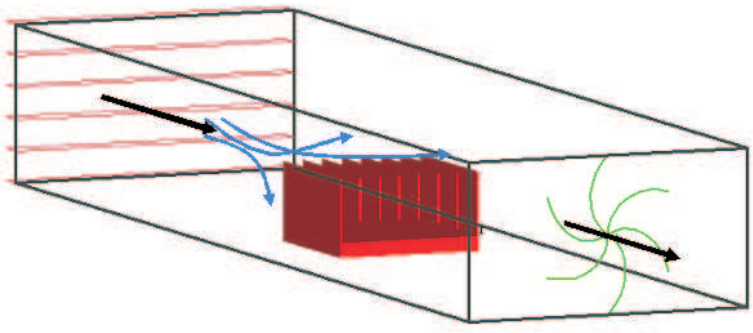

Figure 1.7: Heat Sink with Bypass

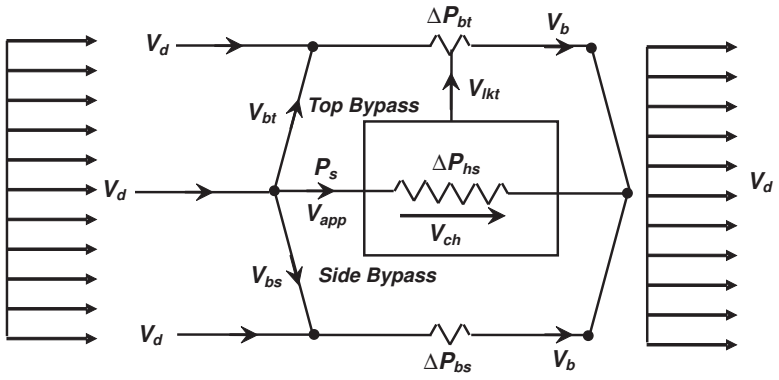

Figure 1.8: Fluid Flow Resistance Network

sink [Fig. 1.8] shows that closely spaced fins create extra resistance to flow through the heat sink due to pressure drop resulting from the frictional drag of the fin walls. As a result of this resistance, the cooling fluid tends to bypass the heat sink and flows through the bypass region. Furthermore, part of the air that does enter the heat sink, following the path of the least resistance, leaks out of the inter-fin spaces into the clearance space above the fin tips. Even when the total air flow from the fan is known, the air speed through the heat sink itself is not known, and therefore, estimation of the thermal performance of a heat sink becomes very difficult. Understanding the phenomenon of bypass is not only necessary to effectively design a heat sink, it is essential for managing the overall thermal performance of the system.

1.2.2 Entropy Generation Minimization (EGM)

It is impossible to design a heat sink of optimized dimension for variable bypass because of the lack of an available model to accurately predict channel velocities in a heat sink. Upon the availability of a compact model to determine the channel velocity, the method of entropy generation minimization, introduced by Bejan (1996), can be used to design an optimized heat sink by simultaneously assessing the parametric relevance of system parameters as they relate to not only the thermal performance but also viscous effects. The entropy generation associated with heat transfer and frictional effects serves as a direct measure of lost potential for work, or in the case of a heat sink, the ability to transfer heat to the surrounding cooling medium.

1.3 Motivation

Heat sink thermal performance characterization has not been standardized to date. This arises from the characterization environment not being representative of the actual application. In addition, characterization methods typically differ between vendors, preventing direct comparison of heat sink performance. Moreover, the performance of a heat sink depends on various factors such as the effects of bypass, spreading resistance, heat sink geometry, fluid and flow properties. These parameters can significantly impact on the measured heat sink thermal performance.

Unfortunately, existing convection heat transfer data in the literature for extended surfaces with bypass invariably require the coolant fluid velocity adjacent to the fin surface be known. Butterbaugh and Kang (1996) and Jonsson and Moshfegh (2001) applied an iterative procedure to estimate the air flow through the channel and bypass by applying pressure balance and mass conservation between heat sink channels and bypass, but they did not provide any system specific detail of their procedure. Lee (1995) developed an equation to find the average inter-fin velocity based on the balance of the mass and momentum equation over the heat sink but without any detail of the pressure drop term that was included in that equation. Moreover, he did not include the bypass pressure drop in his equation, therefore, that model may not be useful for a heat sink with variable bypass. The relationship between thermal resistance and channel flow was hardly addressed in those studies. Wirtz et al. (1994) reported a set of experimental channel flow results that were backed out from the thermal management on longitudinal heat sinks. Recent rapid developments in modern computer technology have resulted in an increased use of three-dimensional numerical simulations or CFD analyses in the field of heat sink design and development. Obinelo (1997), Coetzer and Visser (2003) and Prstic et al. (2000) used CFD methods to characterize the thermal and hydraulic performance of heat sinks with bypass. CFD is unfortunately both time consuming and computationally expensive, which is why the electronics cooling community has identified the need for a compact model. Existing compact models have proved inaccurate and insufficient for accurate convective heat transfer prediction from a heat sink with bypass. Compact modeling of longitudinal fin heat sinks with bypass still remains a topic of interest among thermal researchers.

On the other hand, only a handful of discrete information is available in the literature regarding the optimization of heat sinks with bypass. Most of the work is experimental parametric optimiza-

tion of heat sinks. Because of the lack of a compact model to determine the channel velocity, the simultaneous optimization of heat sink design variables based on minimization of the entropy generation associated with heat transfer and fluid friction with bypass is still missing in the literature.

1.4 Research Goals and Approach

This thesis attempts to address the heat dissipation problem of microelectronics industries by determining the air cooling limit of a parallel plate heat sink under variable bypass conditions. The objectives of this research effort include the following goals:

1. Development of an experimental program that considers the thermal and hydraulic behavior of a heat sink for various duct configurations and flow conditions.

2. Development of a compact model to predict the fluid flow and thermal performance characteristics of a plate fin heat sink under variable bypass conditions.

3. Validation of the model with experimental data from goal 1 and existing literature for thermal and hydraulic performance of a heat sink.

4. Development of an entropy generation minimization model based on the proposed compact model to optimize the overall dimensions and performances of a heat sink for a wide range of parameters such as geometry of the heat sink, heat source and duct, heat load, flow conditions, thermophysical properties of the fluid and heat sink material.

1.5 Thesis Outline

This thesis consists of the following chapters:

- Chapter 1 explains the background, problem statement, motivation and the objectives of this research effort.
- Chapter 2 provides some related information and previous research done by other researchers. It includes a review of recent literature of heat transfer in electronics.
- Chapter 3 describes an experimental program and analysis in order to provide insight into bypass behavior on hydraulic and thermal performance of a heat sink under variable bypass conditions. Experimental data will be used to validate the model described in Chapter 4.
- Chapter 4 presents a valid and reasonable modeling method to predict the channel velocity and thermal characteristics of a heat sink with variable bypass.
- Chapter 5 discusses the design of a heat sink for optimum dimensions and thermal performances based on the compact model developed in Chapter 4 using entropy generation minimization techniques. This chapter also carries out a sensitivity analysis on optimized data for various bypass dimensions, heat sink materials and heat load.
- Chapter 6 summarizes the results and conclusions of this research.

Chapter 2

Literature Review

The performance of heat sinks has been the focus of many investigations in recent years, and the subject has been treated analytically, numerically, and experimentally. Most of the work has dealt with heat sinks in fully shrouded configurations, but several authors have begun to address the issue of heat sinks in ducted flow with tip or lateral clearance or both. The optimal design of heat sinks is also addressed in some research studies using parametric optimization, entropy generation minimization, and least energy optimization techniques.

Depending upon the objectives of this study, the literature review is divided into three main sections; the study of hydrodynamic (fluid flow), heat transfer (thermal) and optimization of plate fin heat sinks with fully shrouded and bypass duct configurations. Each section will review analytical, experimental and numerical studies of plate fin heat sinks. The following flow chart [Fig. 2.1] explains the procedure to review the available literature.

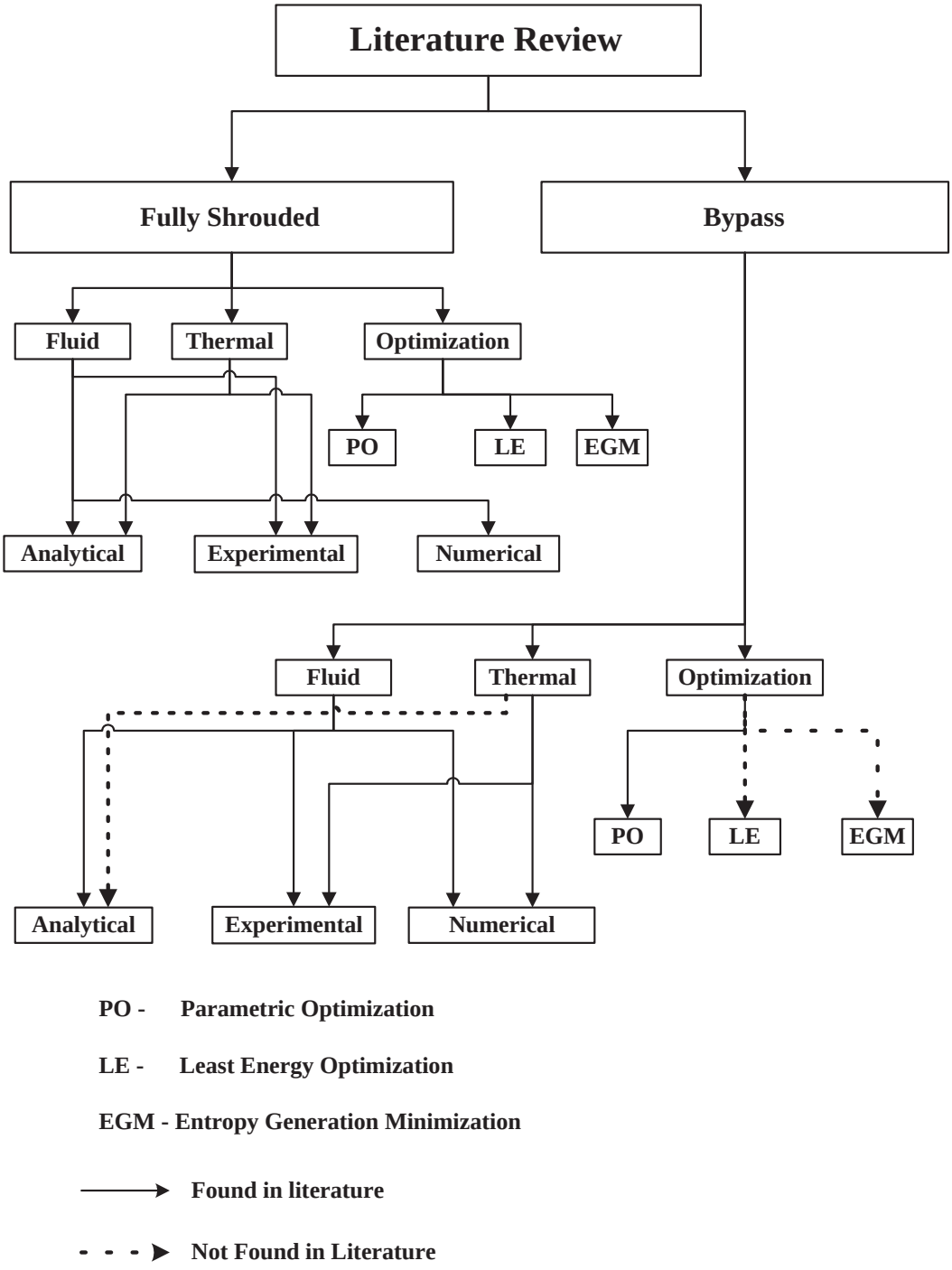

Figure 2.1: Flowchart of Literature Review

2.1 Fully Shrouded Model

Many studies of fully shrouded heat sinks are found in the open literature. The common objective of these studies was to design a heat sink for optimal thermal performance. They studied the influence of fin spacing, fin thickness, number of fins, fin height and fin length on thermal performance of heat sinks. Some of these studies were purely analytical or experimental; some analytical studies with experimental validation were also found. Some studies tried to incorporate fan power in the form of pressure drop in their optimization work. Some of these studies are described below as representations from each category of research.

Experimental

Goldberg (1984) constructed three air cooled, forced convection heat sinks and tested each one. Each heat sink had a different fin thickness, with the channel to fin width ratio restricted to unity, and the flow limited to the laminar regime. The air flow for each heat sink was adjusted to provide a rate of 30 L/min. As expected, the design with the largest pressure drop and smallest channel width yielded the smallest thermal resistance. Only experimental observation was provided in the literature.

Yokono et al. (1988) performed experimental studies of heat transfer from extruded heat sinks of short (height $\leq 5mm$) fins exposed to variable fin spacing, height and air velocity. They suggested that the fin's heat dissipation capability was proportional to the supplied air velocity and heat dissipation was found large with an increase in fin height. The heat transfer coefficient for fins increased with an increase in fin interval and with a decrease in fin width, regardless of fin height. They proposed the following non-dimensional expressions to evaluate cooling performance for small fins.

$$Nu_{2s} = 0.33 \left(Re_{2s} \frac{s}{B} \right)^{0.63}$$

where B and s are width and spacing of a heat sink.

They compared their work with the cooling performance in natural convection, but their work was limited to fins of short height, and the influence of larger fin height ($H > 5mm$) was not examined in their research.

Azar et al. (1992) performed experimental studies on narrow channel ($s = 1.1$ mm) heat sink with air flow arrangement of side-in-side-exit and top-in-side-exit [Fig. 2.2] and found no significant difference in heat sink performance. They performed some experiments with tip clearance and found that the use of heat sinks with tip clearance did not lead to a significant improvement in thermal performance. However, they did not provide any methodology to determine the heat sink thermal performance by experimental correlation or analytical modeling.

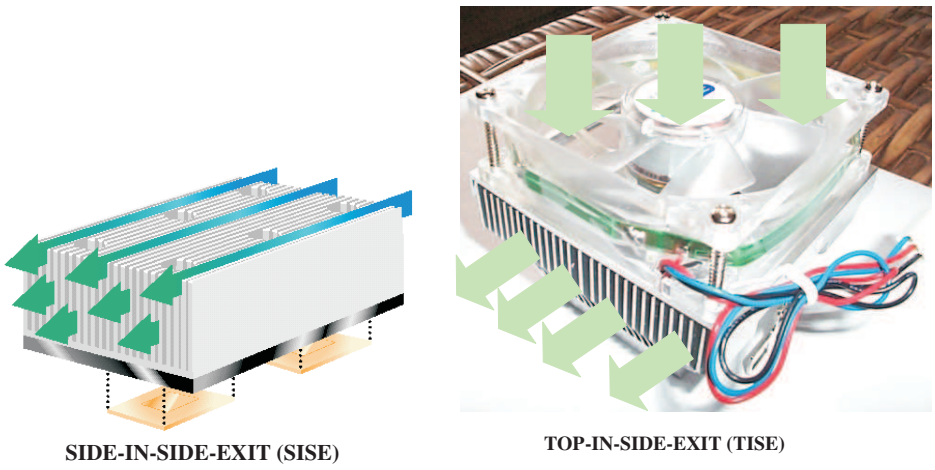

Figure 2.2: Different Types of Flow Arrangement in Heat Sinks

Analytical

Holahan et al. (1996) presented an analytical model for calculating thermal and pressure drop performance in compact, laminar flow parallel plate heat sinks. They adapted laminar convective heat transfer coefficients from existing parallel plate correlations. They also developed a laminar pressure drop model which was applicable for a simple side-inlet-side-exit (SISE) flow pattern and a complex top-inlet-side-exit (TISE) flow pattern [Fig. 2.2]; the model was shown to handle arbitrary flow patterns. TISE model results were found in good agreement with experimental and CFD data. In that model, they also compared the thermal performance of side-inlet-side-exit (SISE) and top-inlet-side-exit (TISE) heat sinks and found that SISE showed better performance at higher pumping power (> 2 watts) and TISE was better at lower pumping power. The model is limited to low Reynolds numbers ranging from 100 to 1000.

Copeland (2000) presented an analysis of simultaneously (hydraulic and thermal) developing flow using compact heat exchanger data fitted to Churchill-Usagi equations [14] for the performance calculation of a plate fin heat sink. They combined laminar fully developed theory to the developing flow (hydraulic and thermal) theory of Shah and London (1978). They also addressed the influence of spreading resistance in their model.

Analytical and Experimental

Teertstra et al. (1999) presented an analytical forced convection asymptotic model for the average heat transfer rate from a plate fin heat sink in a duct flow configuration for the full range of Reynolds number, from fully developed to developing flow. Given a uniform velocity at the heat sink inlet, the model can predict heat transfer from the fin array. No pressure drop model was proposed. Teertstra et al. validated this model with their experiments, and an excellent match (2.1% RMS error) was obtained.

Saini and Webb (2002) proposed a simple model based on developing laminar flow using curve fit data of local friction factor and Nusselt number from Shah and London (1978) and compared their model with experimental hydraulic and thermal performance of two plate fin heat sinks. The model under-predicts thermal resistance and pressure drop by nearly 8% and 20%, respectively.

Kim and Kim (2004) presented a compact modelling method based on the volume-averaging technique and its application to the analysis of fluid flow and heat transfer in straight fin heat sinks. They modelled a straight fin heat sink as a porous medium and developed volume averaged momentum and energy equations for developing flow in shrouded straight fin heat sinks. They determined the permeability, which is related to the viscous shear stress caused by frictional resistance of the fins, analytically from the Poiseuille flow between two infinite parallel plates under a constant heat flux. Using the same method, they also determined the interstitial heat transfer coefficient related to the heat transfer from the fins to the fluid. They compared the model data with the experimental data for pressure drop and heat transfer and showed that the porous medium approach accurately predicts the pressure drop and heat transfer characteristics of straight fin heat sinks.

Analytical and Numerical

Sathyamurthy et al. (1996) investigated inline and staggered parallel-plate arrays and obtained good agreement between their numerical results and experiments. Their results illustrated that the thermal performance of the staggered fin configuration was better than the planar fin configuration over the power and flow ranges examined. This enhanced thermal performance, however, was realized at the expense of an additional pressure drop.

Narasimhan et al. (2003) developed, demonstrated and validated a boundary layer methodology for the application of compact, porous block models for the hydrodynamic behavior of parallel plate heat sinks in laminar flow. They compared the porous block data with the results obtained from several hundred laminar-flow CFD simulations.

2.1.1 Optimization

Heat sink optimization for a fully shrouded case can take the form of parametric optimization, least energy optimization or multi-variable entropy generation minimization.

Parametric Optimization

Azar et al. (1992) reported a method of design optimization and presented contour plots showing the thermal performance of an air cooled narrow channel heat sink in terms of fin thickness and channel spacing parameters. The optimization method was presented assuming the pressure drop across the heat sink was known.

Knight et al. (1992) presented a optimization scheme for thermal design of air cooled finned heat sinks which gave the lowest thermal resistance under specified operating constraints. They examined the influence of number of fins (or fin pitch) on the thermal performance of a particular heat sink. They also validated their scheme with experimental data. Their choice of laminar and turbulent friction factor correlation for calculation of pressure drop in the optimization scheme over predicted the actual flow rate that ended up with lower thermal resistance in the predicted data than the experimentally observed data.

Bejan (1996) and Morega (1993) reported the optimal geometry of an array of fins that minimized the thermal resistance between the substrate and the flow forced through the fins. Staggered

parallel-plate fin arrays were optimized in two steps, first the optimal fin thickness was selected and then the optimal size of fluid channel was determined. They also compared the minimum thermal resistance of staggered parallel-plate arrays and continuous fins. Furthermore, the dimensionless pressure gradient was plotted against Reynolds number.

Copeland (2000) investigated optimum dimensions of fin thickness and pitch for a variety of realistic operating conditions. According to them, fin thickness or pitch does not need to be fully optimized to achieve high performance, but the value of fin thickness or pitch must be near its corresponding optimum value of pitch or thickness.

Iyengar and Bar-Cohen (2000) considered heat sinks of fixed overall dimensions at specific points on fan curves (specific combinations of volume flow rate and pressure drop). Analyses were performed to maximize thermal conductance and conductance per unit mass. A small reduction in thermal performance permitted significant reduction in weight. In addition, aluminum, magnesium and copper were also analyzed. A variety of manufacturing techniques were discussed and dimensional constraints of each were used to perform comparative analyses.

Entropy Generation Minimization

Culham and Muzychka (2001) presented a procedure that allowed the simultaneous optimization of heat sink design parameters based on minimization of the entropy generation associated with heat transfer and fluid friction. The model demonstrated an unconstrained nonlinear procedure for obtaining optimum design conditions without resorting to parametric analysis using repeated iterations with a thermal analysis tool.

Least Energy Optimization

Bar-Cohen and Iyengar (2003) presented a methodology for the least-material and least-energy design of air-cooled heat sinks for the sustainable thermal management of electronic components. They tried to show that the energy invested in the formation and fabrication of such heat sinks can far exceed the pumping power dissipated by commonly used heat sinks. They also proposed a thermal Coefficient of Performance (COP_T) relating the cooling capability of a heat sink to the energy invested in its fabrication/formation (thermal energy) and operation (fluid or pumping

energy). They used the technique of COP_T to determine the degree of sustainability of a specific heat sink design, and compared it to the entropy generation minimization methodology (EGM).

2.2 Bypass Model

Though the issue of bypass was first addressed in the late seventies, there are only a limited number of studies found in open literature. Most of these studies addressed the issue of tip clearance, only a few researchers addressed the issue of both tip and lateral clearance together.

2.2.1 Tip Clearance

Experimental, analytical and numerical studies of a heat sink with tip clearance are found in the literature.

Experimental

Lee et al. (1990) performed experimental studies of heat transfer from extruded heat sinks mounted in a rectangular channel of variable height. Varying the clearance between the tip and the shroud, they determined that the heat transfer coefficient decreases with increasing clearance by up to 20%, but they did not provide any methodology to determine the thermal performance either by experimental correlation or analytical modeling.

Sparrow and Beckley (1981) studied the influence of friction factor on heat transfer and pressure drop characteristics for a longitudinal fin array with tip clearance. They did not provide any methodology to determine the thermal and hydrodynamic performance either by experimental correlation or analytical modeling.

Analytical

Sparrow et al. (1978) presented an analytical work to predict the heat transfer characteristics of a shrouded fin array by simultaneous solution of the governing equations for the fins and the flowing fluid. According to their research, when there is no clearance between the fin tips and the shroud, the fin heat loss distribution attains a maximum between the base and the tip. In the

presence of clearance, the loss increases monotonically along the fin from the base to tip. The main focus of his research was to address the non uniform characteristics of heat transfer coefficient from base to tip with a clearance between the tip and the shroud. This analytical work was carried out by assuming $t \ll s$, therefore, it is not found suitable for compact heat sinks.

Sparrow and Hsu (1981) tried to model the fin-tip heat transfer coefficient in order to provide an accurate representation of the heat transfer process from a heat sink. They carried out their work for a heat sink of fin spacing s $\gg$ t and for a fixed tip clearance. They developed their model assuming laminar fully developed flow, and they did not find any information to validate their model experimentally or numerically.

Analytical and Experimental

Sparrow and Kadle (1986) measured the effect of tip clearance on turbulent heat transfer in relatively long parallel plate heat sinks. Their test data, for turbulent flow conditions, shows a reduction in thermal performance with increasing tip clearance. Their data did not extend to the limit of very large bypass.

Lau and Mahajan (1989) performed experimentally the effects of tip clearance on the performance of a heat sink. They tried to determine the effects of fin density and tip clearance on both thermal resistance and pressure drop. Their data indicate that significant gains in thermal performance can be obtained with high fin density heat sinks for a moderate increase in pressure drop. The data for various values of tip clearances suggest that for higher thermal performance, tip clearance should be kept to a minimum.

Leonard et al. (2002) presented an analytical model to calculate the air leakage from the top of a parallel plate heat sink. They also validated their model with experimental data with an accuracy of 8%. The influence of tip clearance was not included in the model.

Numerical

Coetzer and Visser (2003) investigated the flow behavior in parallel plate heat sinks with tip bypass. They developed a compact model using pressure drop across different heat sinks to predict inter-fin velocity accurately. They also addressed the issue of air leakage from the top by measuring the inlet and outlet inter-fin velocity for various length heat sinks.

Min et al. (2003) presented the effect of tip clearance on the cooling performance of micro-channel heat sinks under the fixed pumping power condition. They showed that the presence of optimal tip clearance can improve the cooling performance of a heat sink; therefore, a heat sink does not need to be fully shrouded to achieve maximum cooling performance.

2.2.2 Tip and Lateral Clearance Model

The influence of bypass with tip and lateral clearance on the performance of a heat sink was studied by some researchers. Most of those were experimental and numerical, and some tried to build compact (analytical) models but those were not found complete or conclusive.

Numerical

Matsushima et al. (1992) measured thermal resistances of finned heat sinks arranged in an in-line array and proposed a prediction technique for their cooling performance. In this technique, the average flow velocity through the fins is estimated based on the assumption that the pressure loss through the fins might be equal to the dynamic pressure difference between the regions immediately upstream and downstream of the heat sink.

Yuan (1996) studied flow bypass effects on straight fin heat sinks in a rectangular duct by computational fluid dynamics modelling. The computational model accuracy was verified by excellent agreement with experimental data of a test problem. Both tip clearance and span-wise spacing which govern the flow bypass were considered. And their significant effects on the heat sink thermal performance were quantified and clearly displayed. Asymptotic conditions represented by a ducted heat sink and the heat sink in an open free space are also considered in the study. Those results were presented and discussed along with the main theme of the flow bypass conditions.

Obinelo (1997) used a CFD method to characterize the thermal and hydraulic performance of heat sinks for system level analysis under flow bypass. They developed a reduced parameter model to increase the speed of the CFD simulation, and results from both the CFD and reduced parameter model were found in good agreement with the measured experimental data.

Experimental

Wirtz et al. (1994) experimentally studied the effect of flow bypass on longitudinal fin heat sinks. They evaluated inter-fin velocity from measured values of fin heat transfer coefficients and used these results to derive a correlation for inter-fin velocity in terms of Reynolds number as a function of the free stream Reynolds number and fin density. They proposed that the overall heat transfer coefficient of these fins could be described by the analytical solution of Shah et al. (1978) for developing flow between parallel plates and suggested a thermal design procedure based on heat transfer correlations. Their experimental results showed up to 60% flow bypass depending on heat sink and duct geometry, and they reported that the effective influence of flow bypass was to reduce the overall heat transfer rate.

Analytical

Iwaski et al. (1994) reported the performance of parallel plate heat sinks with no bypass and at one relatively large value of transverse clearance. They described a flow network method to predict air flow through the heat sink in the presence of lateral bypass but did not report how the various elements of the network could be calculated.

Lee (1995) proposed a prediction technique for inter-fin velocity based on mass and momentum balance between the heat sink and bypass area but without any detail of pressure drop associated with frictional drag, and their prediction technique for inter-fin velocity did not include the frictional pressure drop associated with the bypass region. Therefore, this prediction technique may be applicable with a heat sink of large bypass. Moreover, this study can not provide a clear understanding of the flow and thermal phenomena around the heat sink, and therefore, doubt remains regarding the validity of the model. He compared his data with the experimental data of Wirtz et al. (1994), and the measuring technique of channel velocity by Wirtz et al. (1994) was not conclusive as well.

Simons and Schmidt (1997) proposed a simple hydrodynamic model to predict the inter-fin velocity of a plate fin heat sink by applying mass and momentum balances between fins and bypass area by considering negligible pressure drop in the bypass area, without showing their procedure to calculate pressure drop inside the heat sink. They also did not address the thermal issue in their model.

Analytical and Experimental

Ashiwake et al. (1983) measured and predicted the thermal performance of an array of small finned electronic packages in an air duct. They also studied the influence of thermal wake from upstream modules. Their approach for predicting heat sink performance can be applied only in the limit of very large lateral and tip clearances since the effect of clearances is not included in their method.

Butterbaugh and Kang (1995) investigated the effects of tip and lateral bypass on a heat sink with small fin spacing using compact modelling. Their model used a resistance network approach to balance flow and pressure loss over the heat sink control volumes. Only laminar flow was modelled, and results were found favorable to the experimental data. The predictions of their flow model were within 10% of most of their experimental data. Instead of balancing total energy (kinetic and pressure) of the fluid, they only balanced pressure energy of heat sink and bypass area in their iterative procedure to calculate the inter-fin velocity. They also addressed the issue of air leakage from the top of the heat sink by applying a mass balance between the flow entering the heat sink and leaving from the top (as leakage) and the rear side (as exit) of the heat sink, but no analytical detail of leakage air issue was found in their literature. They did not address the thermal issue of heat sink.

Jonsson and Moshfegh (2001) developed empirical bypass correlations for a plate fin heat sink to predict the dimensionless pressure drop and Nusselt number based on experimental data under variable bypass condition. The correlation for dimensionless pressure drop is in agreement of $\pm 25\%$ with the experimental data, and the correlation for dimensionless Nusselt number is in agreement of $\pm 10\%$ with the experimental data. But the correlation is limited to a certain range of duct Reynolds number, bypass to heat sink area ratio, fin spacing to height ratio and fin thickness to height ratio. They also proposed a physical bypass model for pressure drop, which was found in good agreement with the experimental data considering the simplicity of the model. Other than the correlation for dimensionless Nusselt number, no thermal model was found in their literature.

Analytical and Numerical

Sata et al. (1997) carried out a numerical analysis for the flow and temperature fields around a plate fin array. Based on the knowledge of flow and thermal phenomena around the fin array, they proposed a new technique for predicting the cooling performance of the fins, in which inter-fin velocity is estimated by modelling the energy balances in the flow field around the fin array and between fins under the condition of constant pressure at its downstream edge. Their technique could predict inter-fin velocity with an error level below 20% and the cooling performance with an error level below 30% under practical conditions.

2.2.3 Optimization

Optimization of the dimensions and performance of heat sinks with bypass are found only in the form of parametric optimization models. No literature is found to optimize the design of a heat sink under variable bypass conditions using multi-variable optimization or Entropy Generation Minimization or Least Energy Optimization techniques.

Parametric Optimization

Wirtz et al. (1994), during his experimental work, devised a set of expressions for determining the fin density for different fin geometries and flow conditions. He did not include the influence of bypass and spreading resistance in his optimization work.

Lee (1995) tried to optimize the performance of a plate fin heat sink by studying the parametric behavior of number of fins, fin length and approach velocity under fixed bypass conditions. The effect of bypass was not shown, and the effect of spreading resistance was not considered during the optimization.

2.3 Summary

An extensive literature review of plate fin heat sinks is performed and it is concluded that there are no comprehensive models for accurately determining the thermal performance of a heat sink under bypass conditions. Accurate prediction of thermal performance requires the knowledge of inter-fin velocity, which is very difficult to obtain experimentally as the spacing between the fins is very small (less than 3mm) for compact heat sinks. CFD analysis is assumed to be reasonably accurate, and provides much insight into flow behavior, unfortunately, CFD is both time consuming and computationally expensive, which is why the electronics cooling community has identified the need for a compact model. A compact model for overall heat transfer and pressure drop that incorporates the knowledge of flow bypass around the heat sink, baseplate spreading resistance, baseplate material resistance and thermal contact resistance at the package/heat sink interface can also be applied into an optimization program to design a heat sink of optimum dimensions and performance under variable bypass conditions.

Chapter 3

Experimental Program

3.1 Introduction

The development of analytical or numerical models are inconsequential if they are not based on valid experimental evidence, criticism and rational discussion. One of the important roles of experiments in engineering is to test theories and provide the basis for scientific knowledge. The data obtained from the open literature can be difficult to use because of experimental inconsistencies or the level of uncertainty within the experiments regardless of the agreement between the simulated and the empirical data. Moreover, as discussed in Chapter 2, the current literature contains only a limited set of experimental data for heat sinks with bypass. For this reason, a comprehensive experimental program was conducted to provide insight into the model developed in Chapter 4 and data for evaluating the ability of the models to accurately predict the thermal and hydraulic behavior of heat sinks under a range of design conditions.

3.2 Experimental Objectives

The principal objectives of this experimental program are to obtain the following characteristics of a heat sink:

- Measurement of hydrodynamic characteristics (pressure drop, ΔP_{hs}) under a variable bypass condition.
- Measurement of thermal characteristics (thermal resistance, R_{th}) under a variable bypass condition.

ΔP_{hs} and R_{th} were used to calculate the entropy generation using Eq. 3.1 [11]:

$$\mathcal{S}_{gen} = \mathcal{S}_{th} + \mathcal{S}_{fl} = \frac{Q^2 \times R_{th}}{{T_a}^2} + \frac{\Delta P_{hs} \times \forall_d}{T_a} \qquad \left[\frac{W}{K}\right] \tag{3.1}$$

where

$$\begin{aligned}
\mathcal{S}_{th} &= \text{Thermal entropy generation in } \frac{W}{K} \\
\mathcal{S}_{fl} &= \text{Hydrodynamic entropy generation in } \frac{W}{K} \\
Q &= \text{Heat input in } W \\
R_{th} &= \text{Thermal resistance in } \frac{K}{W} \\
T_a &= \text{Ambient temperature in } K \\
P_{hs} &= \text{Pressure drop in } \frac{N}{m^2} \\
\forall_d &= \text{Duct air flow rate in } \frac{m^3}{s}
\end{aligned}$$

Experimental data were reduced to Q, R_{th}, ΔP_{hs} and $\forall_d$ in order to calculate the entropy generation.

R_{th} was determined using the following relationship:

$$R_{th} = \frac{T_b - T_a}{Q} \qquad \left[\frac{K}{W}\right] \tag{3.2}$$

Q was determined using the following relationship:

$$Q = V\,I \qquad [W] \tag{3.3}$$

3.3 Experimental Facility

An experimental facility was constructed to measure Q, R_{th}, ΔP_{hs} and $\forall_d$ for calculation of entropy generation of a heat sink with variable bypass.

The experimental facility has the following subsections:

- Experimental Setup
- Instruments
- Samples
- Procedure
- Data Acquisition and Recording

3.3.1 Experimental Setup

An experimental setup for measuring the heat transfer and pressure drop characteristics of a parallel plate heat sink was designed and assembled. The setup has the following components:

1. Wind Tunnel Assembly
2. Heater Block Assembly

Wind Tunnel Assembly

The general layout of the wind tunnel is shown in Figs. 3.2 and 3.3. The wind tunnel was fabricated from Plexiglas (thermal conductivity 0.20 W/m·K). The heat sink was installed at the center of the wind tunnel, and air flow was drawn into the wind tunnel through a honeycomb. The honeycomb in the chamber was used to straighten the flow inside the test section.

The top and side walls of the wind tunnel were adjustable [Fig. 3.3] in order to get variable bypass. Pressure taps were mounted in various locations of the duct to measure the pressure drop around the heat sink and bypass area [Fig. 3.1]. Heat sink pressure drop was measured using two

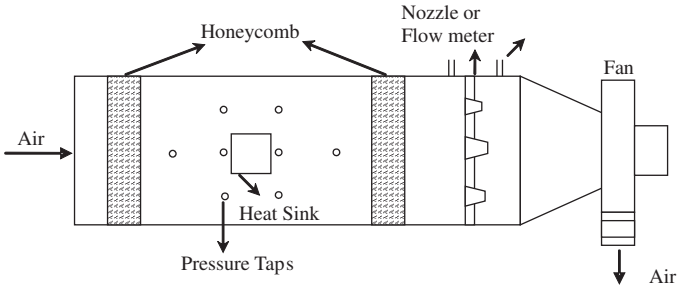

Figure 3.1: Top View of Wind Tunnel Configuration

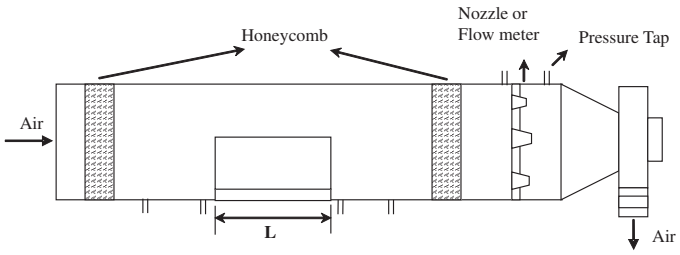

Figure 3.2: Side View of Wind Tunnel Configuration

pressure taps located on the floor of the wind tunnel along the heat sink center line, and they were positioned 5 mm upstream and downstream of the heat sink. A scanivalve [Fig. 3.5] was used to switch from one tap to another.

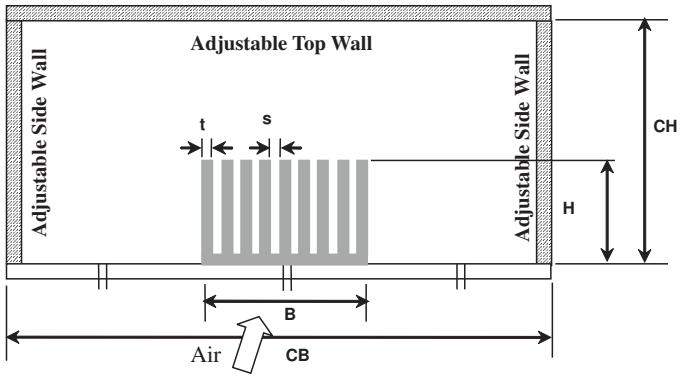

Figure 3.3: Front View of Wind Tunnel Configuration

The air was driven by a fan of Air Flow Measurement System [Fig. 3.5]; The standard flow range of the fan is 3 to 150 CFM. The airflow chamber is designed with multiple nozzles [Fig. 3.4] to cover the required range of airflow. The flow range to be covered is determined by the

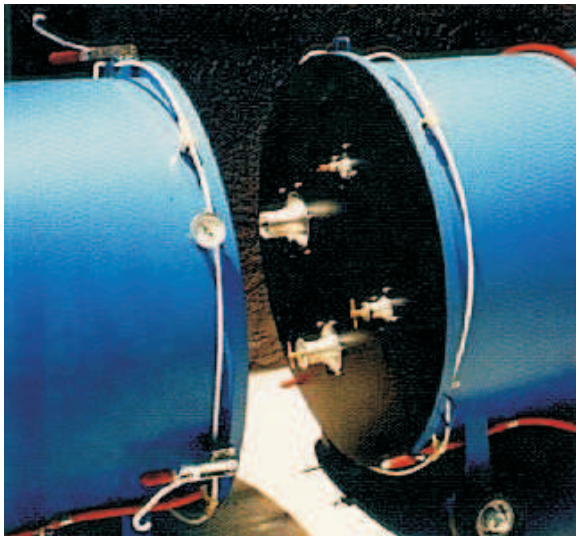

Figure 3.4: Nozzle in Air Flow Chamber [1]

nozzle diameter. The chamber has flow straightening screens installed upstream and downstream of the nozzle array. The screens break up turbulence in the airstream and provide a uniform flow approaching the nozzle array. The nozzle array is accessible through a removable panel for nozzle selection. The flow rate was controlled by the frequency regulation of a motor driving the fan, and the volumetric air flow rate was measured taking the differential pressure across the nozzle of the air flow chamber. For the measurement of inter-fin velocity, a traversing mechanism [Fig. 3.5] was used in order to move the pitot tube horizontally and vertically.

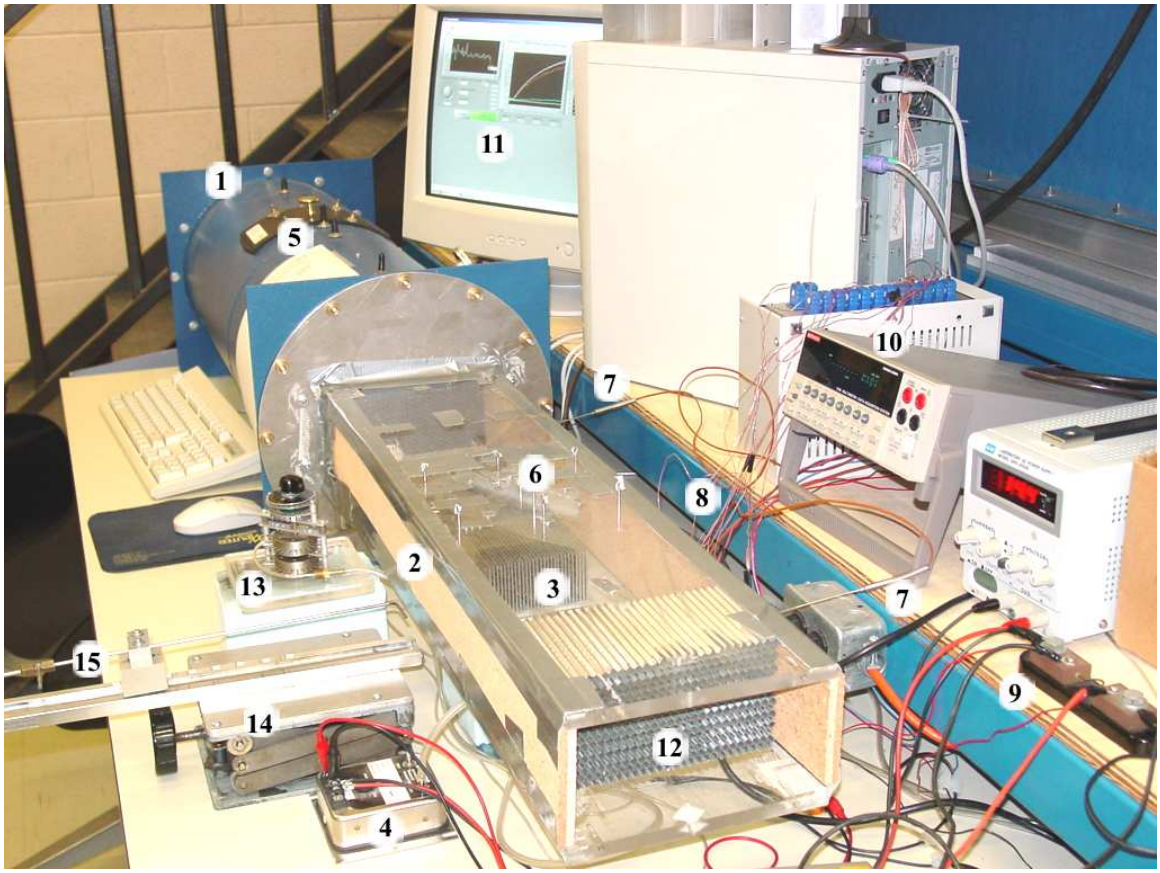

Figure 3.5: Experimental Setup

1	Air Flow Chamber	6	Taps for Pressure	11	Labview Interface
2	Wind Tunnel	7	Thermocouples for T_a	12	Honeycomb
3	Heat Sink	8	Thermocouples for T_b	13	Scannivalve
4	Pressure Transducer	9	Shunt Resistor for I	14	Traverse Mechanism
5	Taps for Nozzle	10	Keithley Data Logger	15	Pitot Tube

3.3.2 Heater Block Assembly

The heat sink was firmly bolted to the heater plates with a thin layer of thermal grease of conductivity 0.7 W/m·K at the interface and a phenolic spacer of thermal conductivity 0.023 W/m·K at the bottom of the heater plate using four countersunk machine screws at an equal distance from the center of the heater plate as shown in Fig. 3.7. The phenolic spacer tried to minimize the heat loss from the bottom of the heater plate, and heat loss from the sides of the heater plate was minimized by applying thermally insulating tapes of conductivity 0.027 W/m·K on each side, as a result, heat was only allowed to flow from the top surface of the heater plate to the heat sink base with a heat loss of 1.5% from the sides and bottom of the heater plate. The heat sink and heater block assembly were mounted on a foamed substrate of thermal conductivity 0.027 W/m·K that insulated all surfaces of the assembly up to the base of the heat sink [Fig. 3.6]. Four 200 W pencil heaters were sandwiched between the top and bottom of the heater plate to provide the necessary heat for the heat transfer test [Fig. 3.7]. The heaters were powered using a regulated DC power supply resulting in line voltages of 19.5, 27.6, 39.1 and 47.9 V at currents of 1.3, 1.8, 2.6 and 3.1 A for a total power output of approximately 25, 50, 100 and 150 W.

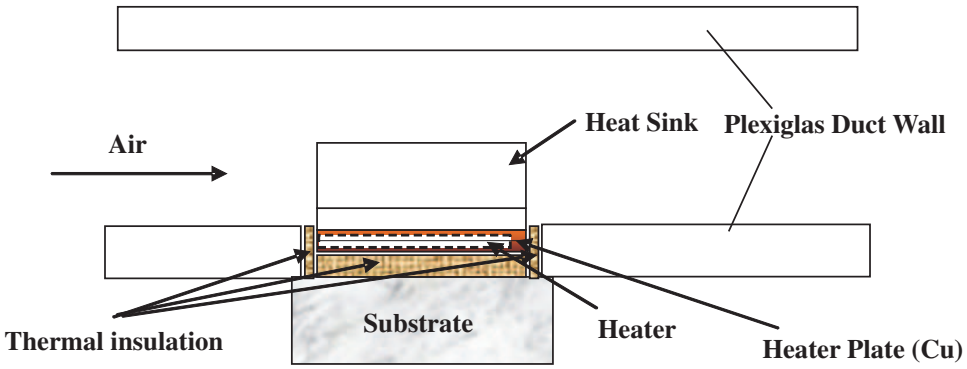

Figure 3.6: Sectional View of Heater Assembly

The baseplate temperature was measured using six T-thermocouples attached to the heat sink baseplate at the locations indicated by $T_1 - T_6$ in Fig. 3.8. Among the six thermocouples, three were placed at three different heights (bottom, middle, top) on the front side of the baseplate facing the air stream, and the remaining three were placed at the same locations of the rear side of base plate. This arrangement was done because for two reasons. First, a temperature gradient exists from bottom to top due to the thickness of the base plate. Second, along the length of the base

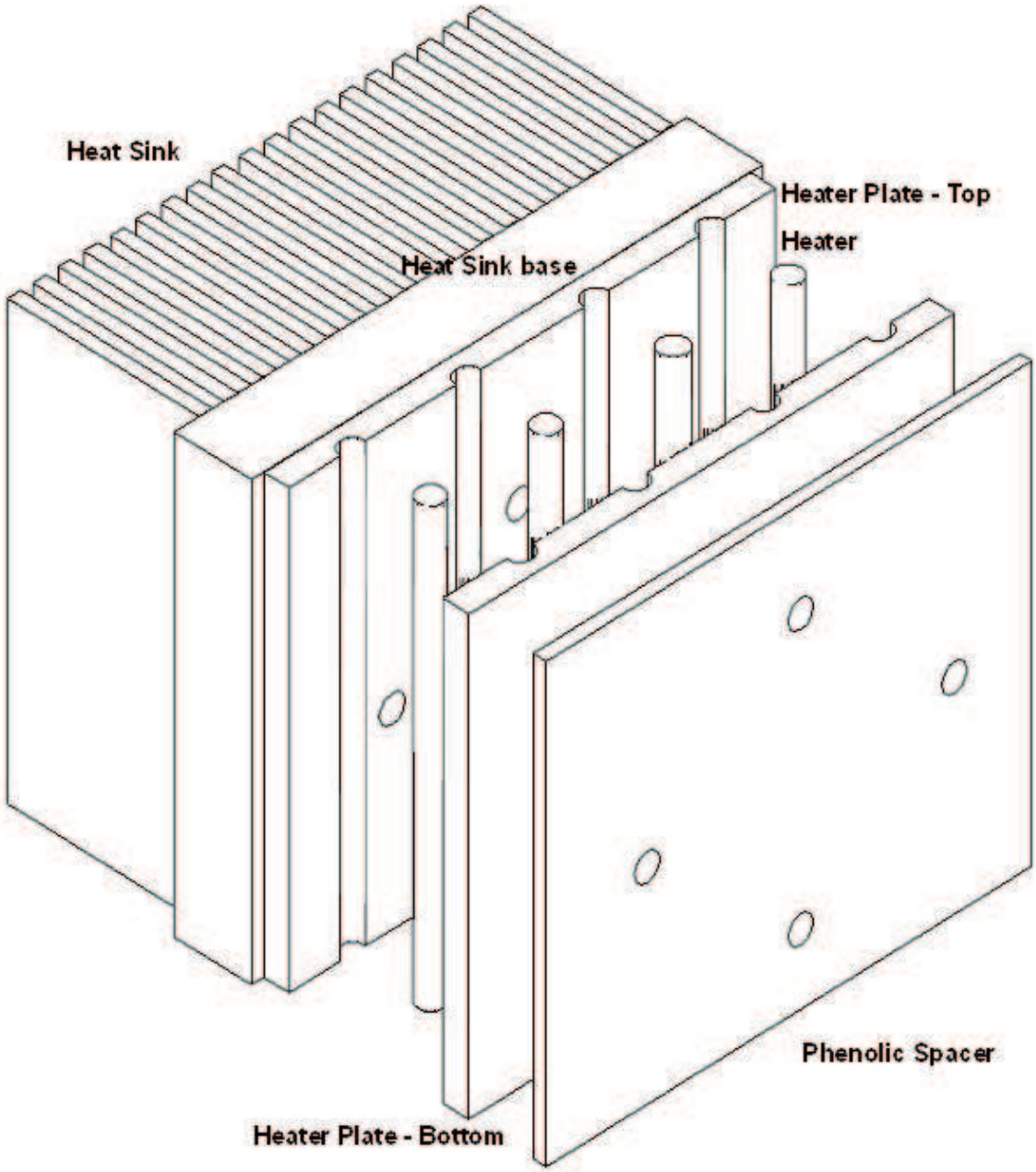

Figure 3.7: Complete Heater Assembly

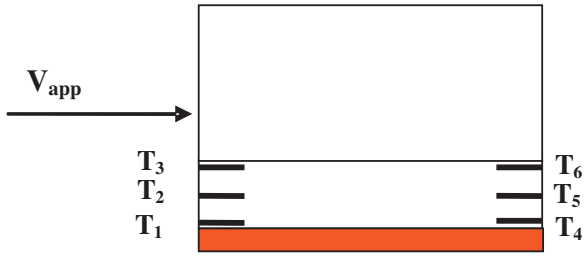

Figure 3.8: Location of Thermocouples at Base Plate

plate, another temperature gradient exists as air receives heat all the way to the exit and gradually transitions from cold to hot as it moves from the front to the exit of the heat sink. An arithmetic average of these measured values provides a better representative value for the mean baseplate temperature, T_b.

3.3.3 Instrumentation

Instruments were used for this experiment to measure the temperature, pressure, flow rate, voltage and current of the power supply.

Temperature Measurement

All temperature measurements for the heat sink base were performed using T-type copper constantan thermocouples attached with aluminium filled epoxy. Conduction losses through the leads were assumed to be negligible because of the small diameter of wires and relatively large value of Q. These thermocouples were glued in shallow, small diameter holes drilled into the base plate [Fig. 3.5]. The ambient temperature in the test section was monitored using two thermocouples [Fig. 3.5] mounted just inside the inlet and exit of the wind tunnel. The accuracy of the thermocouples is found $\pm 0.2\,^0C$.

Pressure Measurement

Pressure transducers (Model-PX653 of Omega) with full scale readings of 0.25, 2 and 10 inches H_2O were used to measure pressures and pressure differentials. To maximize measurement precision, pressure transducers were matched with the smallest suitable range for a given measurement. Transducers were calibrated with the Betz water manometer and a negligible percentage of deviation was observed. Vinyle tubes were used to communicate the ports of a pressure transducer with

the pressure taps of the wind tunnel. The maximum error of the transducers is specified as $\pm 0.25\%$ of the full scale reading by the manufacturer.

Flow Measurement

Pressure taps across the nozzle [Fig. 3.5] of air flow chamber were connected to Omega (Model-PX653) pressure transducers in order to monitor the differential pressure in meter H_2O that was later used along with the system temperature in ^0C and the nozzle diameter in m to calculate the flow rate in m^3/s using the vendor supplied excel spread sheet. The accuracy of temperature and pressure drop measurements remain the same as described before.

Measurement of Heat Input to Heaters

The heaters were powered using a regulated DC power supply capable of 60 V and 7.5 A. The current was measured using a calibrated 5 ampere shunt resistor [Fig. 3.5] of $10 m\Omega$ resistance for a total power output of approximately 25, 50, 100 W.

Inter-fin Velocity Measurement

The inter-fin velocity was calculated by measuring the flow rate through the heat sink. The flow through the heat sink was measured by subtracting the out side (bypass) flow rate from the total flow rate of the wind tunnel obtained from a orifice meter at the back of the wind tunnel. Bypass air velocity was measured using the pressure difference of static and dynamic port of a pitot tube connected to Omega (Model-PX653) pressure transducer.

All data were read in voltages by a Keithley Data Acquisition System model 2700 DMM [Fig 3.5], converted and recorded in desired output parameters such as temperature, pressure, flow rate and heat input through Labview data acquisition software [Fig. 3.5].

Accuracy of Instruments

Instrument	Accuracy
T-Thermocouple	$\pm 0.2^0C$
Omega Pressure Transducer	$\pm 0.25\%$ FS
Keithley Data Acquisition	$\pm 0.005\%$ FS + 300μV

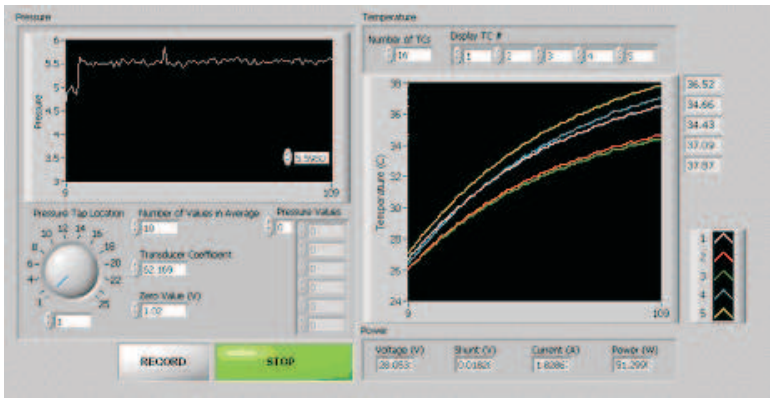

Figure 3.9: Labview Representation of Unsteady State Data of Experiment

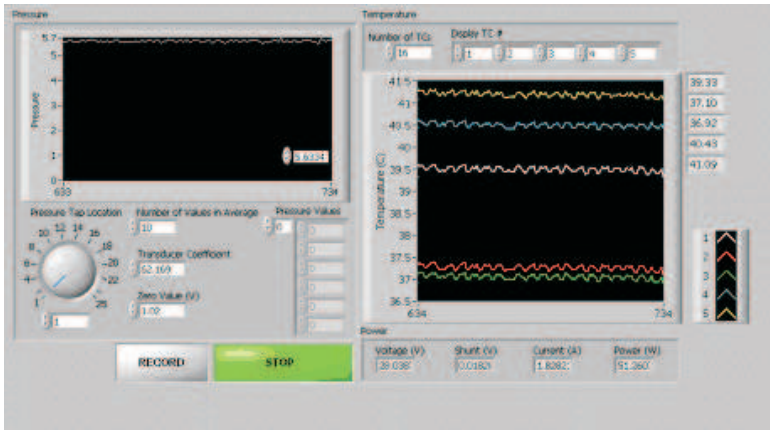

Figure 3.10: Labview Representation of Steady State Data of Experiment

3.3.4 Data Acquisition and Control of Experiment

All measurements were performed using a Keithley 2700 data acquisition system with a 20 channel analog input module. Output terminals of all instruments were connected to this module. The data logger was programmed and controlled using a Windows based PC computer running Labview v.5.1 software.

Labview was selected as the programming language for the data acquisition software because of its compatibility with the instrumentation, the availability of driver files for the Keithley data logger, and its powerful computational and graphical features. All data were recorded to text files in a tab delimited format, which is easily imported into a spreadsheet for analysis. Figures 3.9 and 3.10 present screen images of the Labview data acquisition programs.

3.3.5 Test Procedure:

Experiments were performed using the samples provided in Table 3.1. The effect of base plate material and fin spacing on the thermal performance of a heat sink were examined during the experiment. Bypass was ensured by adjusting the side and top walls to obtain the desired clearance ratio. The duct configurations of Table 3.2 were used during the experiment. For a particular heat sink and duct geometry, the test was started by adjusting the flow rate of the blower through a frequency modulator. Flow rates corresponding to duct velocities 1, 1.5, 2, 2.5, 3 m/s were used during the experiment. For each flow rate, the heat was then supplied to the heater block through a regulated DC power supply to have heat input of 25, 50, 100, 150 W. Each test was allowed to reach thermal steady state over a certain period of time that was confirmed by Labview graphics for base plate temperatures [Fig. 3.10], and the results for pressure drop and temperature were recorded when the heat sink temperatures remain unchanged for a period of 30 minutes.

Table 3.1: Specification of Heat Sinks

Sample	Name	Material		t_b	L	H	B	t	N	s
		Base	Fin	*mm*	*mm*	*mm*	*mm*	*mm*		*mm*
1	AAS2	Al	Al	8	101.5	50	101	1.2	30	2.25
2	CAS2	Cu	Al	8	101.5	50	101	1.2	30	2.25
3	AAS4	Al	Al	8	101.5	50	101	1.2	19	4.3
4	CAS4	Cu	Al	8	101.5	50	101	1.2	19	4.3
5	AAS2.1	Al	Al	8	101.5	50	96	1.2	28	2.25

Pressures were measured using an Omega pressure transducer in which voltage reading is converted to a pressure head, h_P (m) using the following vendor supplied relationship.

$$h_P = \frac{V_{measured} - V_0}{V_{full} - V_0} \times \frac{h_{full}}{39.37} \quad [mH_2O] \tag{3.4}$$

V_0 corresponds to the voltage when both ports of the pressure transducer are exposed to the atmosphere. V_{full} is 5 V and h_{full} is the capacity of the transducers, which are 0.25, 2 and 10 inch H_2O and depend on the requirement of the experiment.

Temperatures were monitored using thermocouples, and the current (I) supplied to the heaters was measured by converting the voltage of shunt resistor.

Table 3.2: Duct Configurations for Experiments [Fig. 3.11]

CB/B	CH/H				
	1	1.25	1.5	1.75	2
1	x				
1.25		x			
1.5			x		
1.75				x	
2					x

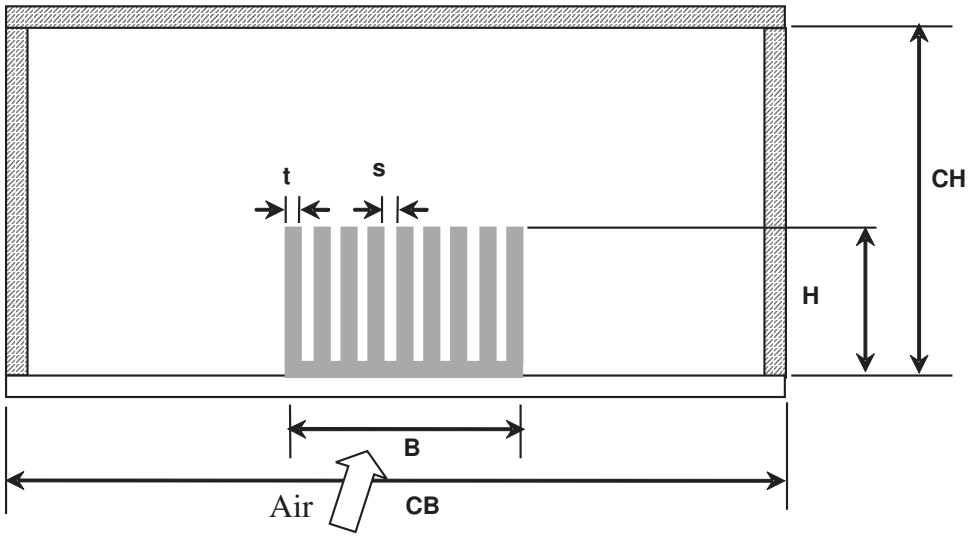

Figure 3.11: Dimensions for Experimental Configurations

3.4 Data Reduction

Experimental data recorded for temperature, pressure, current, voltage were reduced for the following hydrodynamic and thermal properties of a heat sink.

3.4.1 Duct velocity, V_d

Duct flow rate, $\forall_d$ was used to calculate the duct velocity, V_d. $\forall_d$ was found from the vendor supplied excel program using the differential pressure measured across the nozzle of the air flow chamber. From $\forall_d$, V_d is calculated by the following expression:

$$\begin{aligned} V_d &= \frac{\forall_d}{A_d} \\ A_d &= CH \times CB \end{aligned}$$

3.4.2 Pressure Drop, ΔP_{hs}

The pressure drop across the heat sink was measured by taking the difference of upstream and downstream pressure of the heat sink corresponding to the voltage output of the pressure transducer. Equation 3.4 was then used to convert the voltage into a pressure head, h_P(m).

The following relationship was then applied to calculate the pressure in pascal (N/m^2)

$$P = h_P \rho g \qquad [Pa]$$

where g is a constant (9.8 m/s^2) and ρ can be calculated from the following expression assuming that air is an ideal gas,

$$\rho = \frac{p}{R T_a} \qquad \left[\frac{kg}{m^3}\right]$$

where p is the atmospheric pressure measured from a barometer, R is the gas constant (287 J/kg·K) for air at 300 K, and T_a is ambient temperature of the test section monitored using two thermocouples mounted just inside the inlet and outlet of the wind-tunnel.

Figure 3.12 shows the influence of V_d on ΔP_{hs} under variable bypass condition. It is found that ΔP_{hs} gradually decreases from fully shrouded to increasing bypass for a particular V_d.

For internal flow, the pressure drop is defined as:

$$\Delta P_{hs} = \frac{2 f_{ch} L \rho V_{ch}^2}{D_{h_{ch}}}$$
$$f_{ch} \propto \frac{1}{Re_{ch}}$$

From the above equations, it is clear that ΔP_{hs} is a function of V_{ch} only when all other parameters are kept constant. With the increase in bypass, a smaller volume of air flows through the channel that causes a decrease in V_{ch} which in turn results in a decrease in ΔP_{hs}.

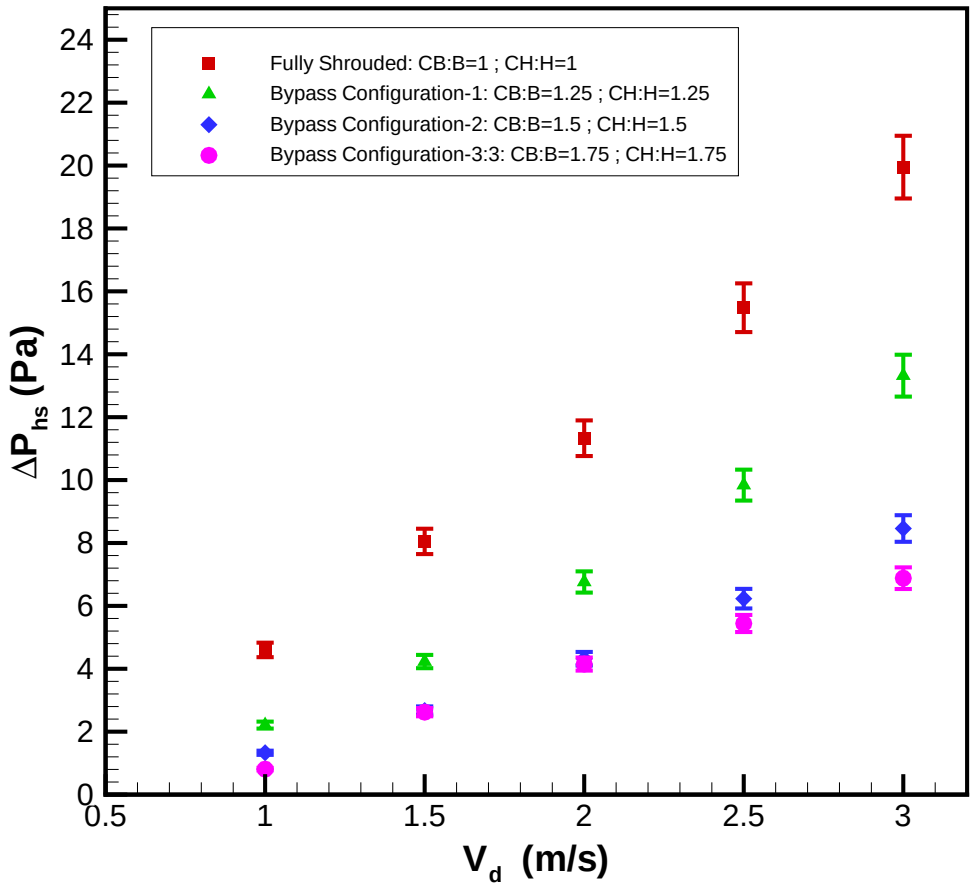

Figure 3.12: Pressure Drop (ΔP_{hs}) vs Duct Velocity (V_d)

3.4.3 Duct Reynolds Number, Re_d

Re_d is measured using the following expression:

$$Re_d = \frac{\rho V_d D_{h_d}}{\mu} \tag{3.5}$$

from Fig. 3.11,

$$\begin{aligned} D_{h_d} &= \frac{4A_d}{\mathcal{P}_d} \\ A_d &= CH \times CB \\ \mathcal{P}_d &= 2\,(CB + CH) \end{aligned}$$

where V_d can be calculated using subsection 3.4.1, ΔP_{hs} and ρ are calculated using subsection 3.4.2, and μ can be calculated from the following relation [41]:

$$\frac{\mu}{\mu_0} = \left(\frac{T}{T_0}\right)^{0.7}$$

where T_0 = 273 K, $\mu_0 = 1.71 \times 10^{-5}\, kg/m \cdot s$, and T is in kelvin. T can be obtained from thermocouple readings for ambient temperature (T_a).

3.4.4 Dimensionless Pressure Drop, C_D

C_D can be written as:

$$C_D = \frac{\Delta P_{hs}}{\frac{1}{2}\rho {V_d}^2}$$

ΔP_{hs} and ρ can be measured using subsection 3.4.2, and V_d can be measured using subsection 3.4.1.

3.4.5 Inter-fin velocity, V_{ch}

In a compact heat sink, channel spacing is very small (less than 3 mm), and it is very difficult to estimate the channel velocity using a pitot tube. Potential blockage effects restrict the use of smaller diameter pitot tubes. The control volume approach was applied to measure the flow rate through the heat sink in this research. The total flow rate of the duct was first obtained through the nozzle or flow meter of the air flow chamber and then, the flow rate of each control volume [CV 1, CV 2 and CV 3 of Fig. 3.13] was measured using a pitot tube by applying procedure described in [18] to measure the average velocity of a rectangular duct. This procedure proved to be lengthy and was not very good for predicting the very small amount of flow through the heat sink because the amount of flow through the heat sink lies within the uncertainty associated with the experiment.

In accordance with [18], the velocity was measured at different locations of each control volume [CV 1, CV 2 and CV 3 of Fig. 3.13] using a pitot tube, and from these velocities, an average velocity through the heat sink was determined using the following calculation.

Total flow rate of the duct from Fig. 3.13 can be given as:

$$\forall_d = \forall_{hs} + 2\forall_1 + 2\forall_2 + \forall_3$$

$$\forall_{hs} = \forall_d - (2\forall_1 + 2\forall_2 + \forall_3)$$

$$\forall_{hs} = \forall_d - \left(2A_1 \frac{1}{25} \sum_{i=1}^{25} V_i + 2A_2 \frac{1}{25} \sum_{j=1}^{25} V_j + A_3 \frac{1}{25} \sum_{k=1}^{25} V_k \right)$$

$$\bar{V}_{hs} = \frac{1}{A_{hs}} \left[\forall_d - \left(2A_1 \frac{1}{25} \sum_{i=1}^{25} V_i + 2A_2 \frac{1}{25} \sum_{j=1}^{25} V_j + A_3 \frac{1}{25} \sum_{k=1}^{25} V_k \right) \right]$$

where

$$A_{hs} = (N-1)\,sH, A_1 = \tfrac{1}{2}(CB-B)\,H,$$

$$A_2 = \tfrac{1}{2}(CB-B)\,(CH-H), A_3 = B\,(CH-H)$$

$\forall_d$ can be obtained using the procedure described in the subsection 3.2. V_i, V_j and V_k are measured using the principle of static pitot tube.

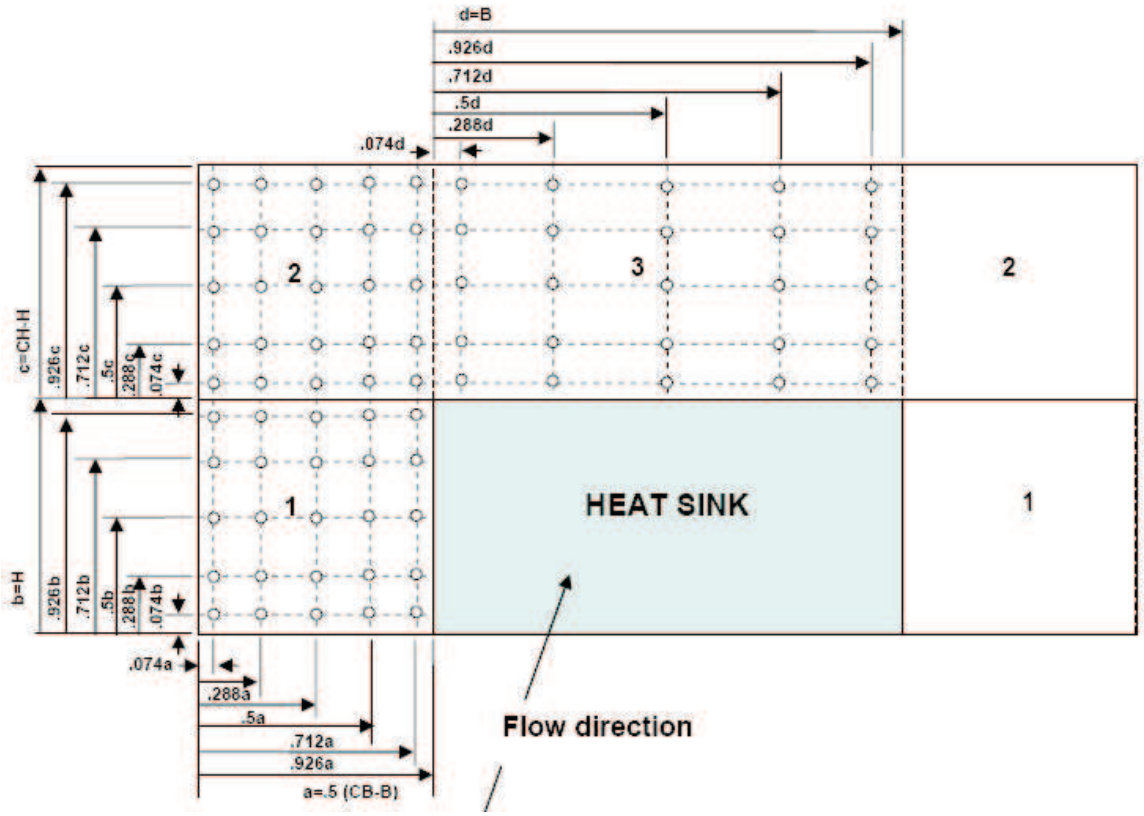

Figure 3.13: Locations of Pitot Tube to Measure Inter-fin Velocity of a Heat Sink

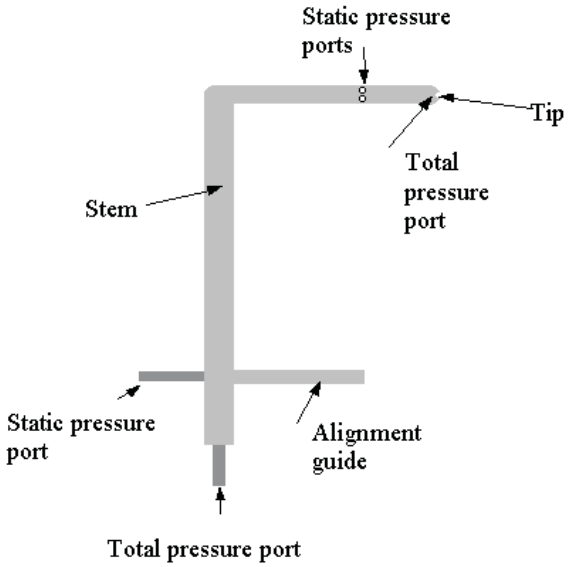

Figure 3.14: Configuration of a Pitot Tube

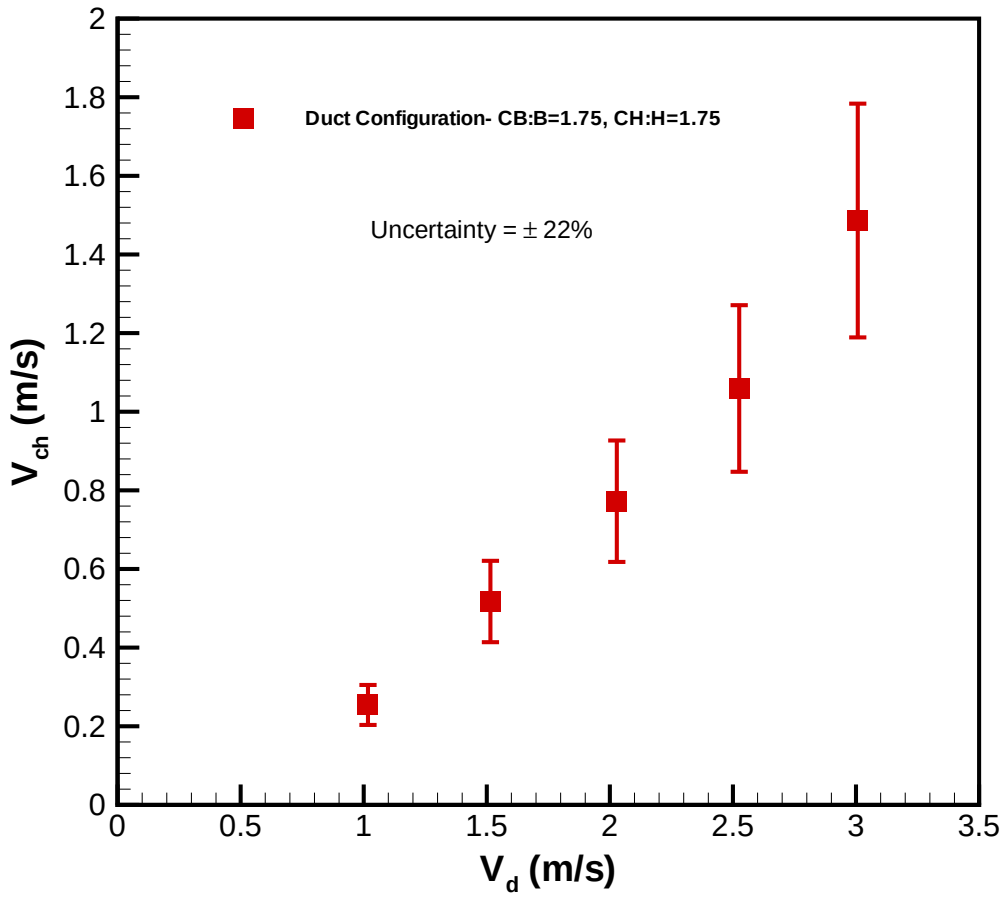

Figure 3.15: Channel Velocity (V_{ch}) vs Duct Velocity (V_d)

Principle of a Pitot Static Tube: The Pitot Static tube measures the difference of the total pressure (or impact pressure) at the nose of the Pitot tube and the static pressure of the air stream at the side ports; from which, we get dynamic pressure [Fig. 3.14]. From this dynamic pressure, air velocity was calculated using the following expression:

$$V_{i,j,k,} = \sqrt{\frac{2P_{dynamic}}{\rho}} \tag{3.6}$$

$P_{dynamic}$ was measured by connecting the total pressure port and static pressure port to a pressure transducer. The procedure described in subsection 3.4.2 was used to convert the voltage reading of pressure transducer to pascal (N/m^2) and calculate the density of air (ρ).

Figure 3.15 shows the measured channel velocity (V_{ch}) for various duct velocities (V_d) and one duct configuration. It was found that the flow through the channel was less for lower duct velocities, and it gradually increased with higher duct velocities.

3.4.6 Thermal Resistance, R_{th}

The expression for thermal resistance is given as:

$$R_{th} = \frac{T_b - T_a}{Q} = \frac{\Delta T}{Q} \qquad \left[\frac{K}{W}\right] \tag{3.7}$$

Heat flow was applied to the heat sink base through a resistance heater, and in the case of a resistance heater, measured values of voltage and current were used to determine the electrical energy dissipated by the heater. The total heat transfer rate was determined by:

$$Q = V \times I \qquad [W] \tag{3.8}$$

T_b was measured by taking the average of six thermocouples attached to the heat sink base.

Heat losses from the bottom and sides of the heater were restricted by putting thermal insulation at these sides. As a result, heat was only allowed to flow from the top surface of the heater. The joint resistance between the heater and the bottom of the heat sink was minimized by applying a thin layer of thermal grease (TIM). To avoid spreading resistance, the heater surface area was the same as the base plate area.

T_a was monitored using two thermocouples mounted just inside the inlet and outlet of the wind-tunnel.

3.4.7 Convective Heat Transfer Coefficient, h

The convection heat transfer rate can be expressed by Newton's Law of Cooling:

$$Q = hA_s\left(T_b - T_a\right) \tag{3.9}$$

$$h = \frac{Q}{T_b - T_a} \times \frac{1}{A_t} = \frac{1}{R_{th}A_t} \tag{3.10}$$

R_{th} can be obtained from subsection 3.4.6 and A_t is obtained from the following expression:

$$A_t = 2NLH + (N-1)\,sL \tag{3.11}$$

3.4.8 Nusselt Number, Nu_{2s}

The Nusselt number is a measure of heat transfer when convection takes place. It is a dimensionless number which measures the enhancement of heat transfer from a surface which occurs in a 'real' situation, compared to the heat transfer that would be measured if only conduction could occur. Using the channel hydraulic diameter ($D_{h_{ch}} = 2s$) as a scale length, the dimensionless Nusselt number can be defined as:

$$Nu_{2s} = \frac{hD_{h_{ch}}}{k_f} \tag{3.12}$$

Substituting h from Eq. 3.11 into Eq. 3.13, we get:

$$Nu_{2s} = \frac{QD_{h_{ch}}}{k_f A_s (T_b - T_a)} \tag{3.13}$$

The value of Q, T_b and T_a can be obtained using the same procedure described in subsection 3.4.6.

$$D_{h_{ch}} = \frac{4sH}{2H+s} \cong 2s, \quad as\ H \gg s$$

A_s was obtained by using Eq. 3.12.

The thermal conductivity of air, k_f, was taken at T_m, which was obtained by the following expression:

$$T_m = \frac{T_b + T_a}{2}$$

where T_m is the mean temperature of air.

Figure 3.16 shows the influence of Re_d on Nu_{2s} under variable bypass conditions. It was found that for a particular Re_d, Nu_{2s} is higher when the heat sink is fully shrouded i.e. clearance around the heat sink is zero, and Nu_{2s} gradually decreases from fully shrouded to increasing bypass because of the lower convective heat transfer coefficient associated with less air flowing through the heat sink channels with increasing bypass.

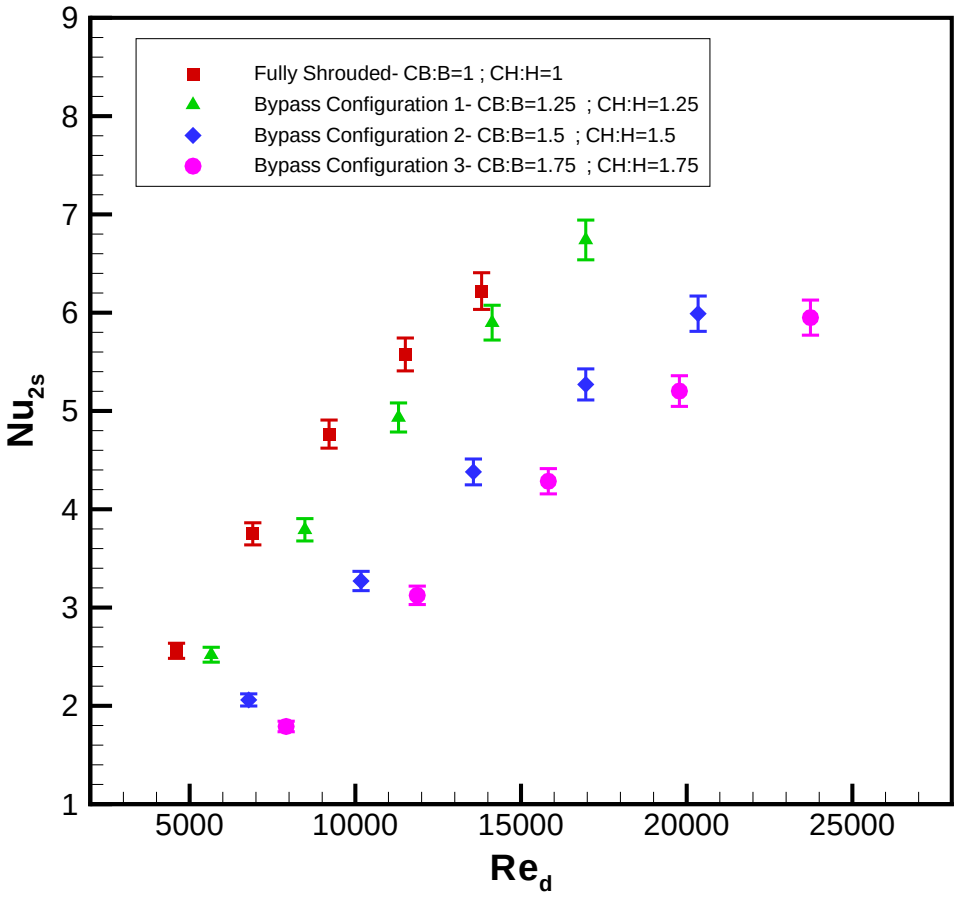

Figure 3.16: Nusselt Number (Nu_{2s}) vs Duct Reynolds Number (Re_d)

3.4.9 Entropy Generation Rate, $\mathcal{S}_{gen}$

Using Eq. 3.1, the entropy generation can be written as:

$$\mathcal{S}_{gen} = \mathcal{S}_{th} + \mathcal{S}_{fl} = \frac{Q^2 \times R_{th}}{{T_a}^2} + \frac{\Delta P_{hs} \times \forall_d}{T_a} \tag{3.14}$$

Q, R_{th}, T_a, ΔP_{hs} and $\forall_d$ were obtained using the procedure described in the previous section.

Figure 3.17 shows the influence of the duct velocity on entropy generation for various duct configurations. It is found that entropy generation increases with increasing bypass because of higher thermal resistance due to reduced channel flow.

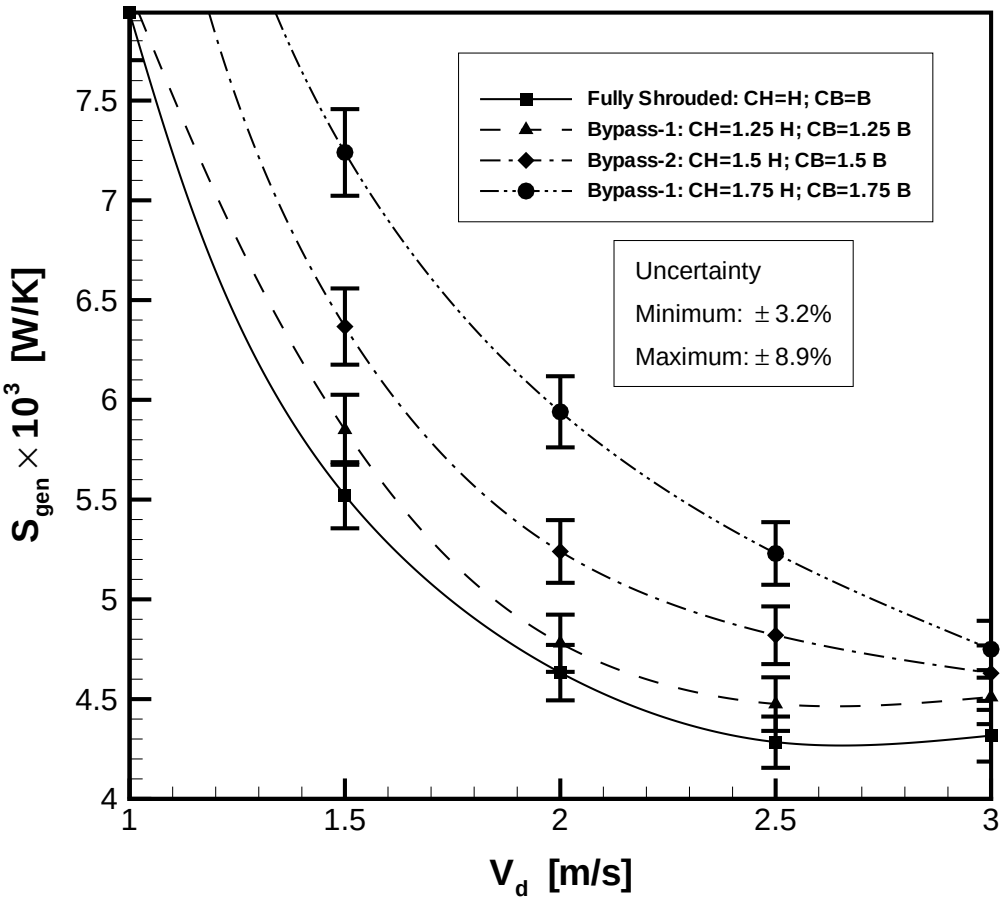

Figure 3.17: Entropy Generation $(\mathcal{S}_{gen})$ vs Duct Velocity (V_d)

3.5 Experimental Uncertainty

The experimental uncertainties in ΔP, R_{th} (or h or Nu) or $\mathcal{S}_{gen}$ were the result of uncertainties in the experimental measurement of temperature, pressure, flow rate, voltage, current and uncertainty in the thermal and fluid properties of the test fluids. A detailed uncertainty analysis was carried out in Appendix D. The result of that analysis is summarized in Table 3.3 when the temperatures are accurately measured within $\pm 0.2^0 C$ and pressures are accurately measured within $\pm 1\%$.

Table 3.3: Uncertainties of Parameters

Parameter	Uncertainty	
	Minimum	Maximum
	%	%
ΔP_{hs}	± 0.33	± 1.14
C_D	± 1.34	± 1.73
Re_d	± 0.79	
R_{th}	± 1.44	± 4.96
h	± 1.45	± 4.95
Nu_{2s}	± 1.5	± 4.96
$\mathcal{S}_{gen}$	± 3.2	± 8.9

3.6 Summary

This chapter presented the details of the experimental procedure and data for various heat sink geometries and duct configurations. One of the objectives of this experimental program was to provide insight for the development of an analytical model. From the data, it was observed that pressure drop decreased and thermal resistance increased with the increase in bypass and pressure drop increased and thermal resistance decreased with the increase in duct velocity. There exists an inverse relationship between pressure drop and thermal resistance. Another important observation was that at the down stream of the heat sink, pressure is the same every where inside the duct but at the upstream, pressure is higher in front of the heat sink when there is a bypass. This may be because of the development of a stagnation pressure in front of the heat sink due to higher frictional drag associated with the heat sink channels than the bypass region. There exists a pressure difference between the front of the heat sink and the bypass region that causes a loss of air to the bypass region until the conservation of mass and momentum is established inside the heat sink and bypass region. As a result, less air flows through the heat sink channel when there is a bypass.

Details of the data reduction procedure are presented. The uncertainties associated with the data obtained from data reduction for thermal and hydraulic performance of a heat sink are found within a reasonable range [Table 3.3]. Experimental data for pressure drop and thermal resistance will be used to validate the analytical model presented in Chapter 4.

Chapter 4

Modelling and Analysis

4.1 Introduction

Finned heat sinks are commonly used for enhancing heat transfer from air cooled microelectronics and power electronics components and assemblies. The use of finned heat sinks increases the effective surface area for convective heat transfer and therefore, decreases the thermal resistance as well as operating temperatures in air-cooled microelectronics. The plate fin heat sink is one of the most common configurations used in current applications. The task of selecting the best heat sink for a particular application from the hundreds of configurations available from the various manufacturers can be a formidable task for an engineer. The choice of an optimal heat sink depends on a number of factors, including the performance, dimensional constraints, the available air flow, and cost, where the optimum configuration provides the best balance between all of these factors. In order to optimize these parameters, design tools are required that quickly and easily predict heat sink performance early in the design process, prior to any costly prototyping or time-consuming detailed numerical studies.

Conventional techniques can predict the overall heat transfer coefficient and pressure drop when the air velocity between the fin is well characterized. Approximating the fin velocity based on the upstream flow rate in an enclosure is often difficult, except in the case where the heat sink is fully shrouded. The heat sink in a enclosure commonly occupies only a fraction of the cross-section of the air flow channel. The air flow area that exists around the heat sink allows some

of the oncoming air flow to bypass the heat sink because of the higher resistance to flow through the channel. Furthermore, part of the air that does enter the heat sink, following the path of least resistance, leaks out of the inter-fin spaces into the clearance space above the fin tips. Therefore, the actual flow through the fins is unknown and difficult to estimate, especially when trying to accurately predict the thermal performance of a heat sink.

The accurate prediction of air flow through a heat sink requires a knowledge of the convective heat transfer coefficient for a fin surface using existing forced convection models for a plate fin heat sink assuming developing laminar flow. Laminar flow is a reasonable approximation since the channel hydraulic diameter and flow through the channel are very small, yielding low Reynolds numbers. Using the convection heat transfer coefficient, the total thermal resistance of a heat sink will be modelled using existing models for convection/conduction heat transfer of fins, spreading resistance, thermal joint resistance and conduction resistance for the base plate.

The entropy generation is a unique concept that combines both the heat sink resistance and pressure drop. It can be obtained by combining a mass, force, energy, and entropy balance across a heat sink. It is a function of all system parameters considered in this study. By minimizing entropy generation with respect to each design variable, the overall thermal performance of a heat sink can be optimized. An Entropy Generation Minimization (EGM) model will be discussed in the next chapter for minimizing the entropy associated with thermal and fluid resistances. Models developed in this chapter will be used in the Entropy Generation Minimization (EGM) model.

Based on the above discussions, the present chapter is divided into the following sections:

- Fluid Flow Model
- Thermal Resistance Model
- Entropy Generation Model

4.2 Fluid Flow Model

When a compact plate fin heat sink is placed in a uniform flow field without bypass, the flow entering the channel encounters pressure drop due to contraction, expansion and frictional resistance because of viscous dissipation of the fluid flow along the channel. The system resistance shifts the operating point of the fan curve by lowering the flow. In the case of a heat sink with bypass, the stagnation pressure associated with heat sink resistance builds up in front of the heat sink and tends to bypass some of the flow towards the clearance zones around the heat sink if the resistance in the clearance zone is less than the resistance of the channel. The clearance region can only accommodate a fixed amount of flow until the resistance in clearance region becomes equal to the resistance of the channel. For any additional resistance, the fan starts operating at a lower flow rate in order to establish equilibrium because of the system resistance. Therefore, the influence of clearance needs to be addressed carefully in order to quantify the amount of flow bypass, which may be obtained by modelling the hydrodynamic balance across the heat sink and the bypass region.

4.2.1 Fully Shrouded Model

This analysis will assume a uniform velocity of magnitude V_{ch} through the channel formed between the fins. From the heat sink geometry [Fig. 4.2], we see that $s \ll H$, therefore, the flow field is considered two-dimensional in the x and z direction.

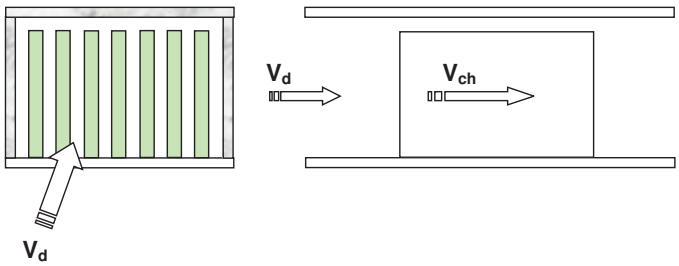

Figure 4.1: Fully Shrouded Configuration

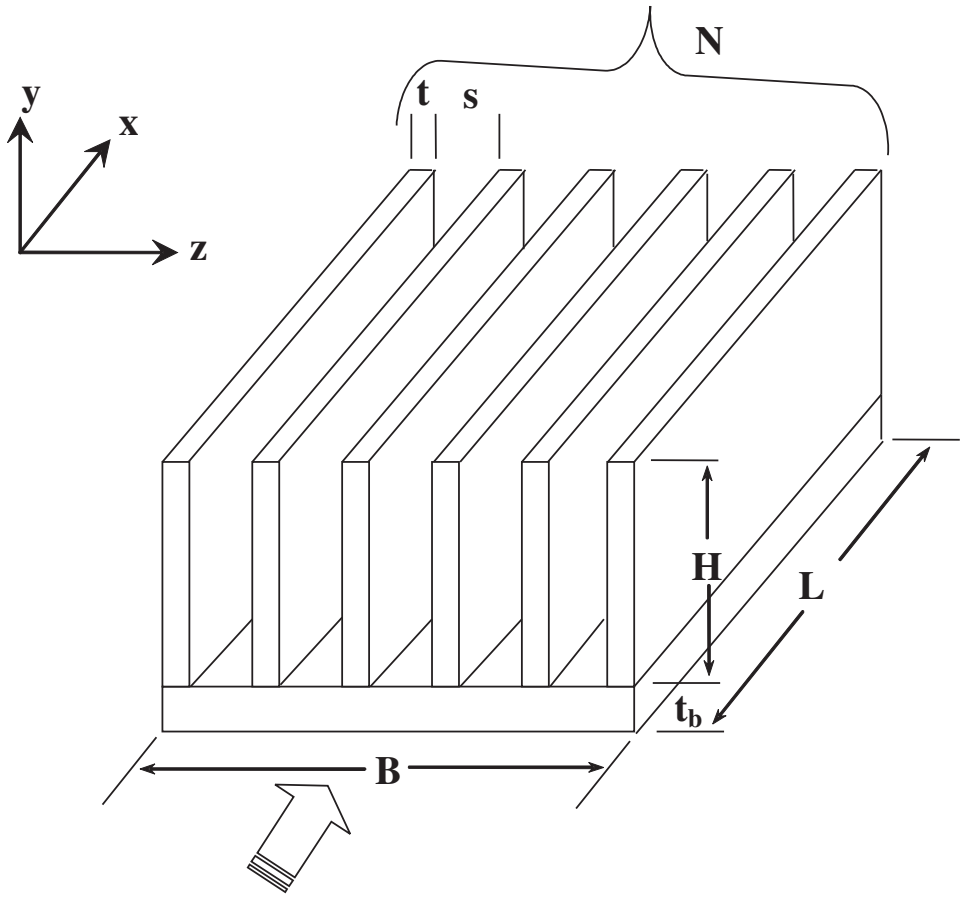

Figure 4.2: Geometry of a Heat Sink

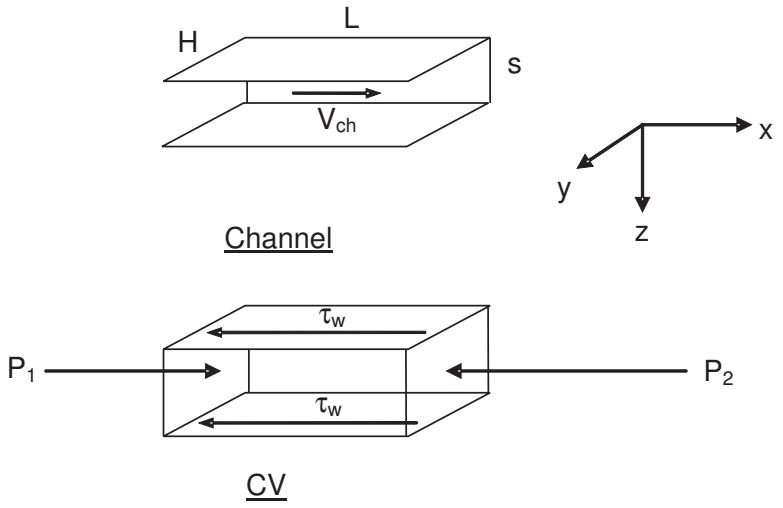

Figure 4.3: Forced Distribution in the Control Volume of a Channel

Laminar Fully Developed Model for Frictional Pressure Drop

Using a control volume analysis [Fig. 4.3], the one dimensional momentum flux is written as:

$$\sum F = \frac{d}{dt}\left(\int_{CV} \vec{V}\, d\forall\right) + \sum\left(\dot{m}_i \vec{V}_i\right)_{out} - \sum\left(\dot{m}_i \vec{V}_i\right)_{in} \tag{4.1}$$

For steady flow, Eq. 4.1 for the CV of channel [Fig. 4.3] is reduced to:

$$(P_1 - P_2)A_{ch} - \tau_w \mathcal{P}_{ch} L = \dot{m}_{ch} V_{ch} - \dot{m}_{ch} V_{ch} = 0 \tag{4.2}$$

Substituting P_1-$P_2 = \Delta P$, we get:

$$\Delta P = \frac{\tau_w \mathcal{P}_{ch} L}{A_{ch}} \tag{4.3}$$

From the definition of hydraulic diameter, we get:

$$D_{h_{ch}} = \frac{4A_{ch}}{\mathcal{P}_{ch}} \tag{4.4}$$

where,

$$\begin{aligned} A_{ch} &= H \times s \\ \mathcal{P}_{ch} &= 2 \times (H + s) \end{aligned}$$

After rearranging Eq. 4.4, we get:

$$\frac{\mathcal{P}_{ch}}{A_{ch}} = \frac{4}{D_{h_{ch}}} \tag{4.5}$$

After substitution, Eq. 4.3 becomes:

$$\Delta P = \frac{4\tau_w L}{D_{h_{ch}}} \tag{4.6}$$

The Fanning friction coefficient is defined as:

$$f = \frac{\tau_w}{\frac{1}{2}\rho V_{ch}^2} \tag{4.7}$$

Rearranging Eq. 4.7, τ_w is found as:

$$\tau_w = f\left(\frac{1}{2}\rho V_{ch}^2\right) \tag{4.8}$$

After substitution of τ_w , Eq. 4.6 becomes:

$$\Delta P = \frac{2fL\rho V_{ch}^2}{D_{h_{ch}}} \tag{4.9}$$

The hydraulic diameter can also be written as:

$$D_{h_{ch}} = \frac{4A_{ch}}{\mathcal{P}_{ch}} = \frac{4sH}{2(H+s)} = \frac{2s}{\left(1+\frac{s}{H}\right)} = \frac{2s}{1+\alpha} \tag{4.10}$$

where the aspect ratio, $\alpha = \frac{s}{H}$; when $H \to \infty$, $\alpha = 0$, the rectangular channel flow becomes flow between parallel plates.

For laminar fully developed parallel flow, the solution of the Navier-Stokes Equation for wall shear stress reduces to the following expression [Eq. A.19 of Appendix A]:

$$\tau_w = \frac{12\mu V_{ch}}{D_{h_{ch}}(1+\alpha)} \tag{4.11}$$

Substituting the value of τ_w from Eq. 4.11 into Eq. 4.6, we get the expression for ΔP:

$$\Delta P = \frac{48L\mu V_{ch}}{D_{h_{ch}}^2(1+\alpha)} \tag{4.12}$$

Comparing Eq. 4.9 and 4.12, we get:

$$\frac{2fL\rho V_{ch}^2}{D_{h_{ch}}} = \frac{48L\mu V_{ch}}{D_{h_{ch}}^2(1+\alpha)} \tag{4.13}$$

After necessary manipulation, the laminar fully developed friction factor for a rectangular duct becomes:

$$f = \frac{24}{Re_{ch}(1+\alpha)} \tag{4.14}$$

$$fRe_{ch} = \frac{24}{1+\alpha} \tag{4.15}$$

Equation 4.15 is found in good agreement [Fig. 4.4] with the existing laminar fully developed friction factor data for a rectangular duct of aspect ratios up to 0.75 [61]. Beyond 0.75 to 1 (square duct), the model falls apart because of the assumption of two dimensional flow fails. The flow in y direction can no longer be ignored beyond aspect ratio 0.75. Typically, in microelectronics industries, the aspect ratio of a heat sink channel is found below 0.25.

For flow between parallel plates, $\alpha = 0$, the expression for friction factor becomes:

$$f = \frac{24}{Re_{ch}} \tag{4.16}$$

$$f Re_{ch} = 24 \tag{4.17}$$

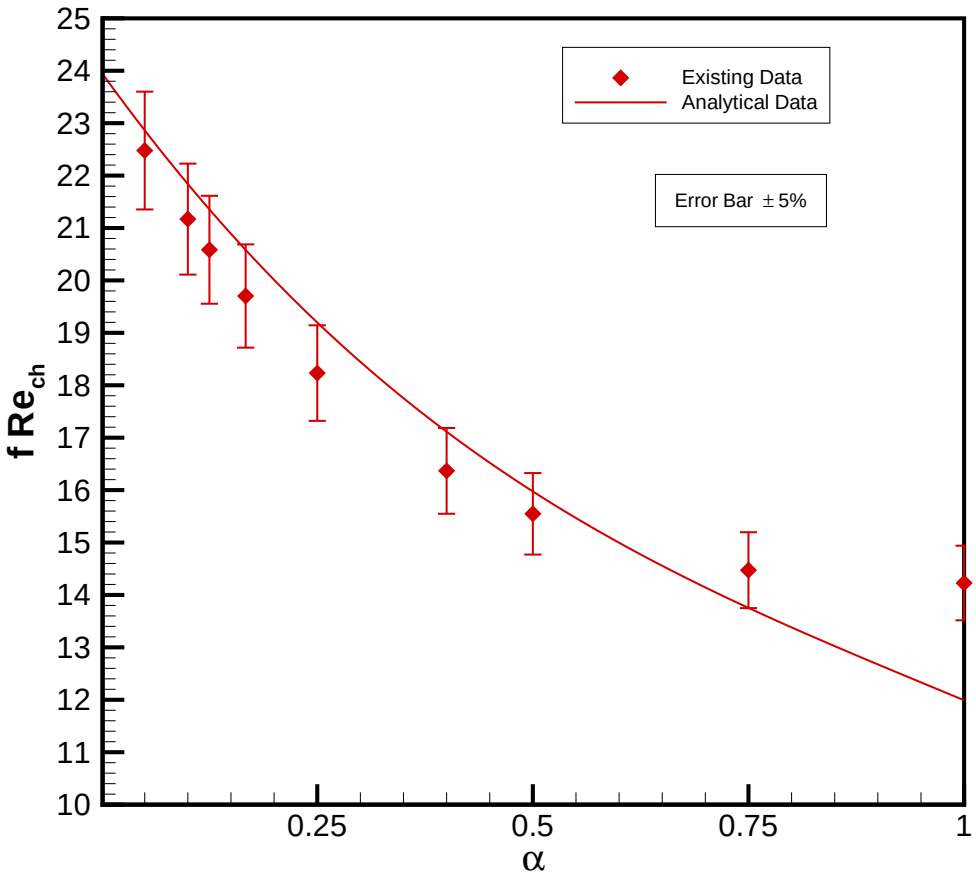

Figure 4.4: Validation of Model with Existing Laminar Fully Developed Friction Factor Data [61]

Laminar Hydrodynamically Developing Model for Frictional Pressure Drop

For laminar hydrodynamically developing flow, the friction factor in the rectangular channel is defined as the apparent friction factor, f_{app}, and it may be computed using a form of the model developed by Muzychka and Yovanovich (1998) :

$$f_{app}Re_{ch} = \left[\left(\frac{3.44}{\sqrt{L^*}}\right)^2 + (fRe_{ch})^2\right]^{\frac{1}{2}} \tag{4.18}$$

fRe_{ch} is the laminar fully developed friction factor and can be substituted from Eq. 4.15 into Eq. 4.18:

$$f_{app}Re_{ch} = \left[\left(\frac{3.44}{\sqrt{L^*}}\right)^2 + \left(\frac{24}{1+\alpha}\right)^2\right]^{\frac{1}{2}} \tag{4.19}$$

where,

$$\begin{aligned} \text{Dimensionless Length,} \quad L^* &= \frac{L}{Re_{ch}D_{h_{ch}}} \\ \text{Channel Aspect Ratio,} \quad \alpha &= \frac{s}{H} \\ \text{Channel Reynolds Number,} \quad Re_{ch} &= \frac{\rho V_{ch} D_{h_{ch}}}{\mu} \end{aligned}$$

Pressure Drop Model for a Heat Sink

The pressure drop across a heat sink is expressed as:

$$\Delta P_{hs} = P_c + P_f + P_e \tag{4.20}$$

The contraction pressure drop, P_c can be expressed by the following:

$$P_c = K_c\left(\frac{1}{2}\rho V_d^2\right) \tag{4.21}$$

where the contraction loss coefficient, K_c is correlated from the graph of Kays and London (1984) for laminar flow:

$$K_c = 1.18 + 0.0015\sigma - 0.395\sigma^2 \tag{4.22}$$

The expansion pressure drop, P_e can be expressed by the following:

$$P_e = K_e \left(\frac{1}{2} \rho V_{ch}^2 \right) \tag{4.23}$$

where the expansion loss coefficient, K_e is correlated from graph of Kays and London (1984) for laminar flow:

$$K_e = 1 - 2.76\sigma + \sigma^2 \tag{4.24}$$

The frictional pressure drop, P_c inside the channel is expressed by Eq. 4.9:

$$P_f = \frac{2 f_{app} L \rho V_{ch}^2}{D_{h_{ch}}} \tag{4.25}$$

The heat sink channel velocity, V_{ch} is expressed by conservation of mass for one channel:

$$V_{ch} = \frac{V_d}{\sigma} \tag{4.26}$$

where σ is expressed by the following:

$$\sigma = \frac{s}{s+t} \tag{4.27}$$

Figure 4.5 compares the fully shrouded model data for pressure drop with experimental data for various channel velocities, and it is found that the model data are in good agreement (RMS error 3.4%) with the experimental data. The experimental data exhibits an uncertainty of $\pm 1.2\%$ because of the accuracy of the measurement apparatus.

Dimensionless Pressure Drop, C_D

The dimensionless pressure drop is defined as:

$$C_D = \frac{\Delta P_{hs}}{\frac{1}{2} \rho V_d^2} \tag{4.28}$$

Figure 4.6 compares the fully shrouded model data for dimensionless pressure drop with experimental data for various duct Reynolds numbers, and it is found that the model data are in good agreement (RMS error 3.5%) with the experimental data. The experimental data exhibits an uncertainty of $\pm 1.2\%$ because of the accuracy of the measurement apparatus.

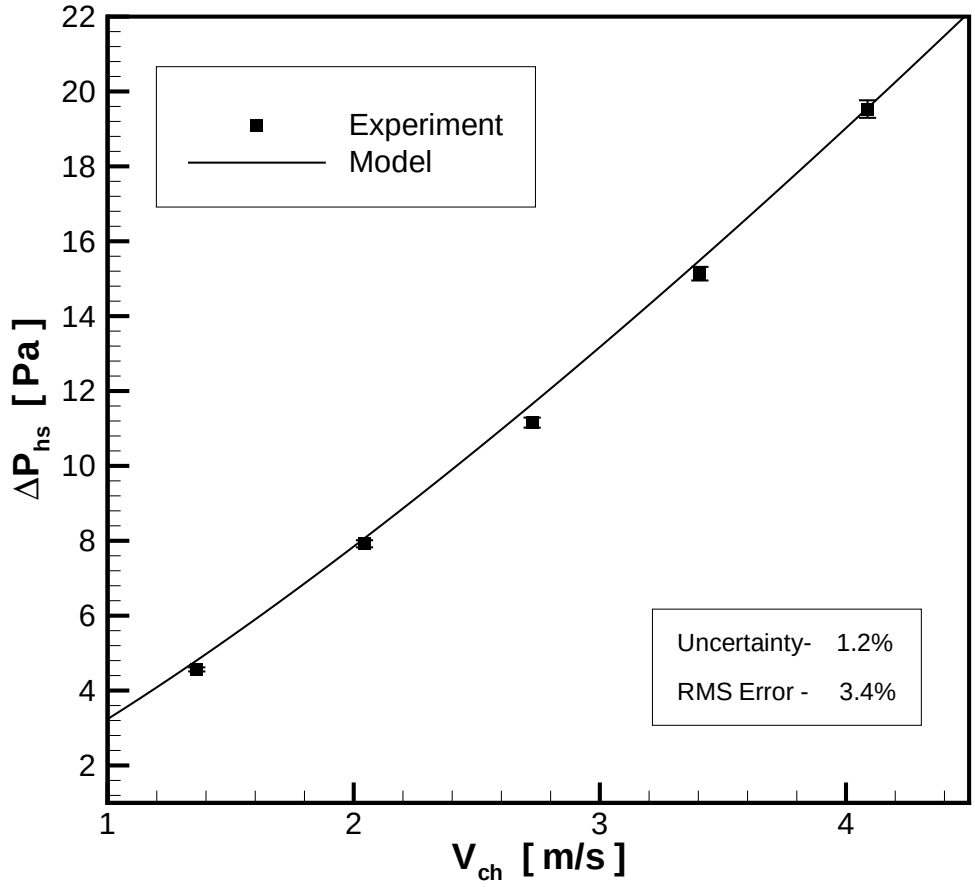

Figure 4.5: Validation of Fully Shrouded Model with Experimental Data for ΔP_{hs} vs V_{ch}

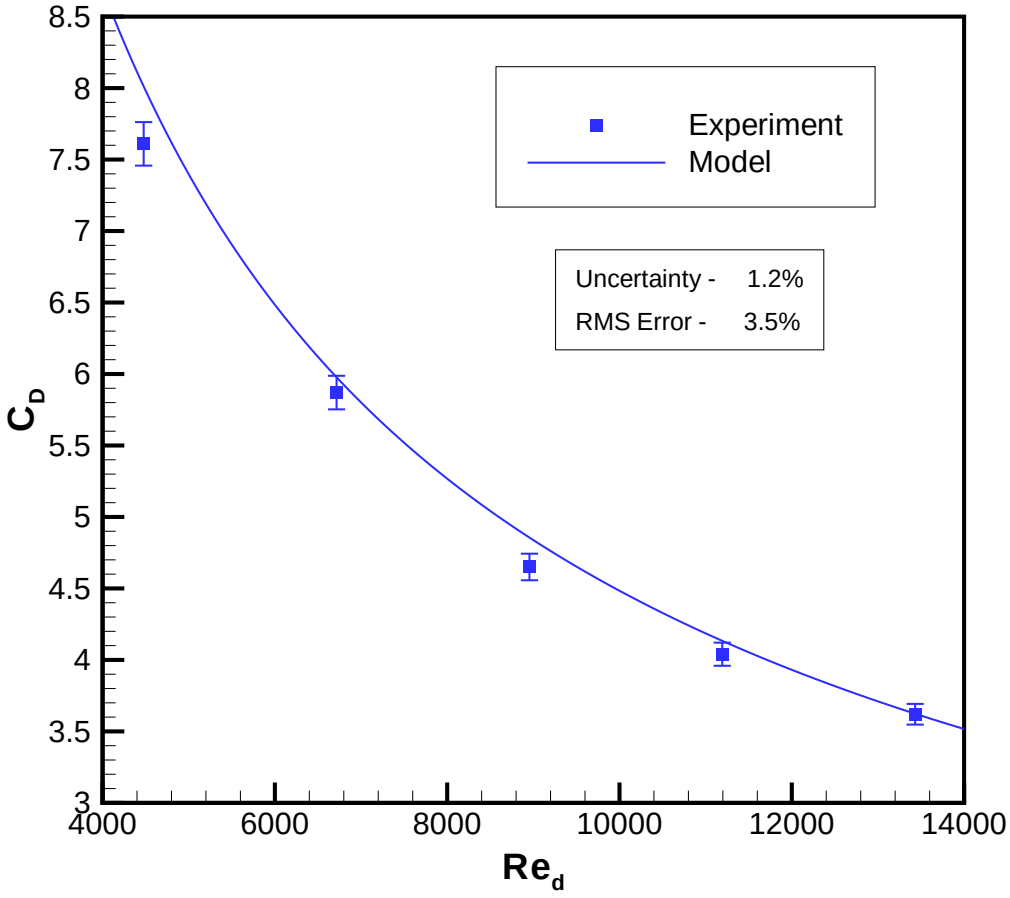

Figure 4.6: Validation of Fully Shrouded Model with Experimental Data for C_D vs Re_d

4.2.2 Bypass Model

In order to precisely predict the cooling performance of a heat sink under bypass, the accurate prediction of the average velocity (V_{ch}) between the fins is important. In this model, V_{ch} is estimated by modelling energy balances in the flow around the heat sink (bypass area) and between fins provided the pressure is assumed constant in the span-wise direction of the duct at the downstream edge of the heat sink (Figs. 4.7, 4.8, 4.9). Downstream of the heat sink, all flow is exposed to the same cross-sectional area of the duct and will yield the same velocity and pressure. The approximation of constant pressure is also found in good agreement with the experimental data.

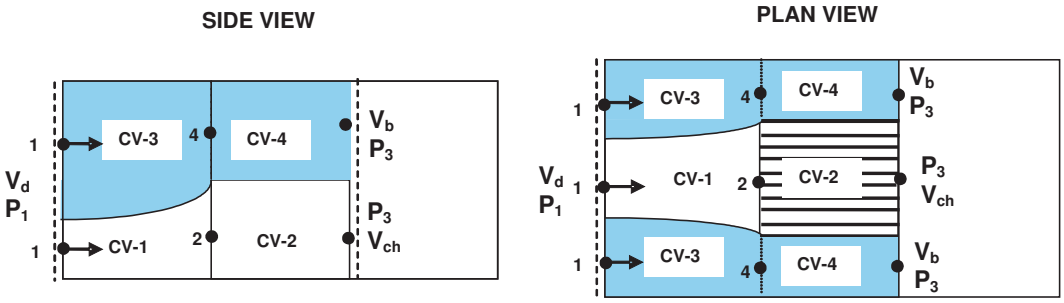

Figure 4.7: Control Volumes for Bypass and Heat Sink

In order to evaluate an energy balance, control volumes in flow zones within the heat sink (CV-1 and CV-2) and bypass area (CV-3 and CV-4) are established (Fig. 4.7). At the upstream boundary of both volumes (CV-1 & CV-3), stream-wise velocity and pressure are fixed at V_d and P_1. The downstream boundaries of both volumes (CV-2 & CV-4) are established at the downstream edge of the heat sink (x=L). Constant outlet velocities V_{ch} and V_b are given for volumes CV-2 and CV-4 respectively, while pressures at the downstream boundaries of both volumes (CV-2 & CV-4) are at P_3. The velocity in the entire bypass area is assumed constant, V_b.

Applying Bernoulli's equation for CV-1 and CV-2:

$$P_1 + \frac{1}{2}\rho V_d^2 = P_2 + \frac{1}{2}\rho V_2^2 = P_3 + \frac{1}{2}\rho V_{ch}^2 + \Delta P_{hs} \tag{4.29}$$

Applying Bernoulli's equation for CV-3 and CV-4:

$$P_1 + \frac{1}{2}\rho V_d^2 = P_4 + \frac{1}{2}\rho V_4^2 = P_3 + \frac{1}{2}\rho V_b^2 + \Delta P_b \tag{4.30}$$

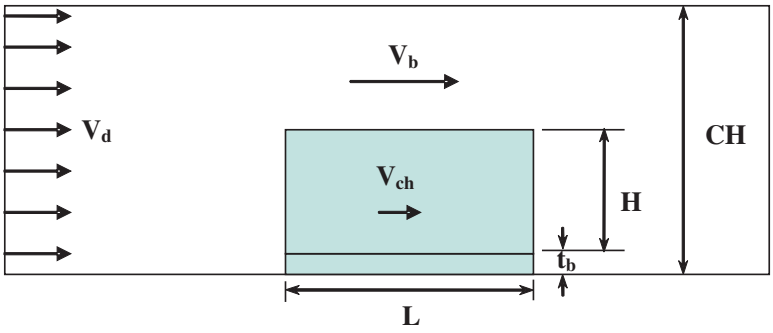

Figure 4.8: Side View of Bypass Configuration

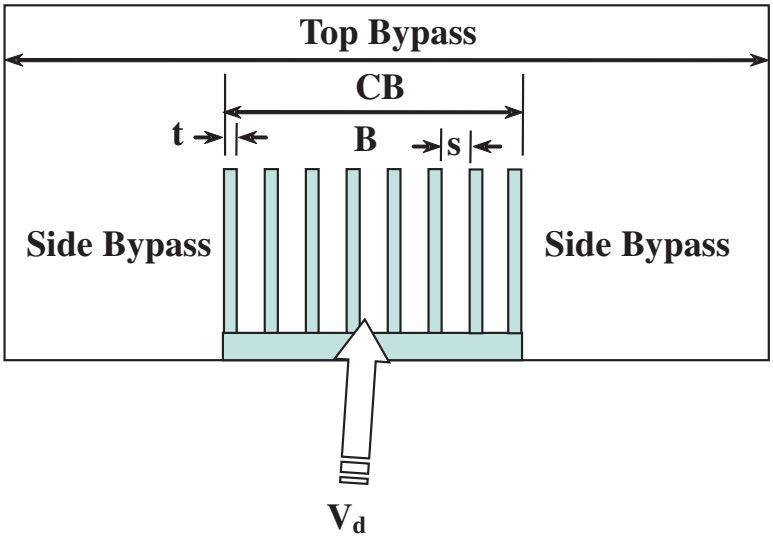

Figure 4.9: Front View of Bypass Configuration

Equating Eqs. 4.29 and 4.30:

$$P_3 + \frac{1}{2}\rho V_{ch}^2 + \Delta P_{hs} = P_3 + \frac{1}{2}\rho V_b^2 + \Delta P_b \tag{4.31}$$

Rearranging Eq. 4.31:

$$V_b^2 - V_{ch}^2 = \frac{2\,(\Delta P_{hs} - \Delta P_b)}{\rho} \tag{4.32}$$

Applying conservation of mass in CV-3 and CV-4:

$$\rho A_d V_d = \rho\,(A_{ch} V_{ch} + A_b V_b) \tag{4.33}$$

Rearranging Eq. 4.33:

$$V_b = \frac{A_d\, V_d - A_{ch} V_{ch}}{A_b} = \frac{A_d\, V_d - A_{ch} V_{ch}}{A_d - A_{hs}} = \frac{V_d - \dfrac{A_{ch}}{A_d} V_{ch}}{1 - \dfrac{A_{hs}}{A_d}} \tag{4.34}$$

or

$$V_b = \frac{V_d - a_{ch} V_{ch}}{1 - a_{hs}} \tag{4.35}$$

where

$$\frac{A_{ch}}{A_d} = a_{ch}; \quad \frac{A_{hs}}{A_d} = a_{hs}; \quad A_d = CB \times CH; \quad A_{hs} = B \times H;$$

$$A_{ch} = (N-1) \times A_{1ch}; \quad A_{1ch} = s \times H$$

Substituting $1 - a_{hs} = a_0$ into Eq. 4.34:

$$V_b = \frac{V_d - a_{ch} V_{ch}}{a_0} \tag{4.36}$$

Substituting V_b from Eq. 4.35 into Eq. 4.32:

$$\frac{(V_d - a_{ch} V_{ch})^2}{a_0^2} - V_{ch}^2 = \frac{2\,(\Delta P_{hs} - \Delta P_b)}{\rho} \tag{4.37}$$

Rearranging Eq. 4.36:

$$(1 - a_{ch} u_{ch})^2 - a_0^2 u_{ch}^2 = \frac{a_0^2\,(\Delta P_{hs} - \Delta P_b)}{\frac{1}{2}\rho {V_d}^2} \tag{4.38}$$

where

$$u_{ch} = \frac{V_{ch}}{V_d}$$

After some manipulation, Eq. 4.37 becomes:

$$\left(a_{ch}^2 - a_0^2\right) u_{ch}^2 - 2\,a_{ch}\,u_{ch} + 1 = \frac{a_0^2\,(\Delta P_{hs} - \Delta P_b)}{\frac{1}{2}\,\rho\,{V_d}^2} \tag{4.39}$$

For the fully shrouded case, a_{hs} = 1 and a_0 = 0, and Eq. 4.39 becomes:

$$\begin{aligned} a_{ch}\,u_{ch} &= 1 \\ V_{ch} = \frac{A_d\,V_d}{A_{ch}} &= \frac{Q_d}{A_{ch}} \qquad \text{(Conservation of mass)} \end{aligned}$$

Using Eq. 4.20, ΔP_{hs} is found:

$$\Delta P_{hs} = P_c + P_f + P_e \tag{4.40}$$

where P_c can be written as:

$$P_c = K_c\,\left(\frac{1}{2}\,\rho\,V_{app}^2\right) \tag{4.41}$$

The heat sink approach velocity, V_{app} can be written as:

$$V_{app} = V_{ch}\,\sigma \tag{4.42}$$

From Eq. 4.22, K_c is found:

$$K_c = 1.18 + 0.0015\,\sigma - 0.395\,\sigma^2 \tag{4.43}$$

where P_e can be written as:

$$P_e = K_e\,\left(\frac{1}{2}\rho V_{ch}^2\right) \tag{4.44}$$

From Eq. 4.24, K_e is found:

$$K_e = 1 - 2.76\,\sigma + \sigma^2 \tag{4.45}$$

σ is expressed by the following:

$$\sigma = \frac{s}{s+t} \tag{4.46}$$

For a compact heat exchanger, the channel spacing is very small, which results in a very small hydraulic diameter, $D_{h_{ch}}$. On the other hand, because of the bypass, the amount of flow through the heat sink channel will be less due to higher resistance to flow through the channel which will result in a low channel velocity. A smaller hydraulic diameter and low channel velocity will yield a low

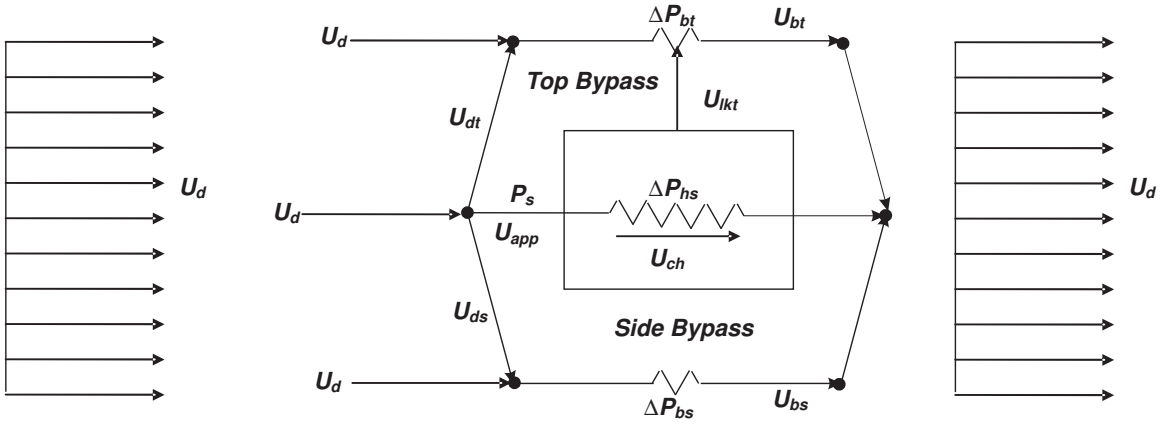

Figure 4.10: Fluid Flow Resistance Network

Reynolds number. Therefore, flow through the heat sink channel is assumed laminar developing flow.

For laminar developing flow, the frictional pressure drop inside the channel is expressed by Eq. 4.9:

$$P_f = \frac{2 f_{app_{ch}} L \rho V_{ch}^2}{Dh_{ch}} \tag{4.47}$$

$f_{app_{ch}}$ is obtained from Eq. 4.19:

$$f_{app_{ch}} Re_{ch} = \left[\left(\frac{3.44}{\sqrt{{L_{ch}}^*}} \right)^2 + \left(\frac{24}{1+\alpha_{ch}} \right)^2 \right]^{\frac{1}{2}} \tag{4.48}$$

where,

$$\text{Channel Dimensionless Length,} \quad {L_{ch}}^* = \frac{L}{Re_{ch} D_{h_{ch}}}$$

$$\text{Channel Aspect Ratio,} \quad \alpha_{ch} = \frac{s}{H}$$

$$\text{Channel Reynolds Number,} \quad Re_{ch} = \frac{\rho V_{ch} D_{h_{ch}}}{\mu}$$

$$\text{Channel Hydraulic Diameter} \quad D_{h_{ch}} = \frac{4 A_{ch}}{\mathcal{P}_{ch}} \approx 2\,s \qquad \text{as } s \ll H$$

After substitution, Eq. 4.40 becomes:

$$\Delta P_{hs} = f\left(V_{ch}\right) \tag{4.49}$$

ΔP_b can be expressed as:

$$\Delta P_b = 2 \times \Delta P_{b_s} + \Delta P_{b_t} \tag{4.50}$$

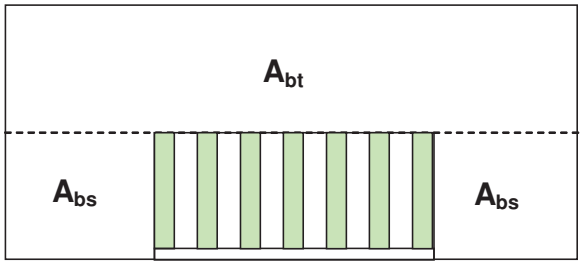

Figure 4.11: Arrangement of Bypass

where,

$$\Delta P_{b_s} = \text{pressure drop in side bypass, and}$$
$$\Delta P_{b_t} = \text{pressure drop in top bypass}$$

Expansion and contraction losses in the bypass channel will be assumed negligible as there is no sharp change of velocity in the bypass region. Therefore, the pressure drop in the bypass region will only be considered for frictional pressure drop.

Using Eq. 4.9, ΔP_{b_s} can be expressed as:

$$\Delta P_{b_s} = \frac{2 f_{app_{bs}} L \rho V_b^2}{D h_{bs}} \tag{4.51}$$

$f_{app_{bs}}$ is obtained from Eq. 4.19:

$$f_{app_{bs}} Re_{bs} = \left[\left(\frac{3.44}{\sqrt{L_{bs}^*}} \right)^2 + \left(\frac{24}{1+\alpha_{bs}} \right)^2 \right]^{\frac{1}{2}} \tag{4.52}$$

where,

$$\text{Side Bypass Dimensionless Length,} \quad L_{bs}^* = \frac{L}{Re_{bs} D_{h_{bs}}}$$
$$\text{Side Bypass Aspect Ratio,} \quad \alpha_{bs} = \frac{CB - B}{2H}$$
$$\text{Side Bypass Reynolds Number,} \quad Re_{bs} = \frac{\rho V_b D_{h_{bs}}}{\mu}$$
$$\text{Side Bypass Hydraulic Diameter,} \quad D_{h_{bs}} = \frac{4A_{bs}}{\mathcal{P}_{bs}} = \frac{4(CB-B)H}{(CB-B)+4H}$$

After substitution, Eq. 4.50 becomes:

$$\Delta P_{b_s} = f(V_b) = f(V_{ch}) \tag{4.53}$$

Using Eq. 4.9, ΔP_{b_t} can be expressed as:

$$\Delta P_{b_t} = \frac{2 f_{app_{bt}} L \rho V_b^2}{D_{h_{bt}}} \tag{4.54}$$

$f_{app_{bt}}$ is obtained from Eq. 4.19:

$$f_{app_{bt}} Re_{bt} = \left[\left(\frac{3.44}{\sqrt{L_{bt}{}^*}} \right)^2 + \left(\frac{24}{1+\alpha_{bt}} \right)^2 \right]^{\frac{1}{2}} \tag{4.55}$$

where,

$$\begin{aligned}
\text{Top Bypass Dimensionless Length,} \quad L_{bt}{}^* &= \frac{L}{Re_{bt} D_{h_{bt}}} \\
\text{Top Bypass Aspect Ratio,} \quad \alpha_{bt} &= \frac{CH - H}{B} \\
\text{Top Bypass Reynolds Number,} \quad Re_{bt} &= \frac{\rho V_b D_{h_{bt}}}{\mu} \\
\text{Top Bypass Hydraulic Diameter,} \quad D_{h_{bt}} &= \frac{4 A_{bt}}{\mathcal{P}_{bt}} = \frac{4CB(CH-H)}{(CB+B+2)(CH-H)}
\end{aligned}$$

After substitution, Eq. 4.53 becomes:

$$\Delta P_{b_t} = f(V_b) = f(V_{ch}) \tag{4.56}$$

Substitution of ΔP_{b_t} and ΔP_{b_s} into Eq. 4.49 gives:

$$\Delta P_b = f(V_{ch}) \tag{4.57}$$

After substituting ΔP_{hs} and ΔP_b into Eq. 4.39, there will be only one unknown in that equation which is V_{ch} and solution of that equation will give the value of V_{ch}.

Figure 4.12 compares the bypass model for pressure drop with experimental data for various duct velocities, and it is found that model data are in good agreement (RMS error ranging from 0.36% to 11%) with the experimental data. The experimental data exhibits an average uncertainty of $\pm 2\%$ because of the accuracy of the measurement apparatus.

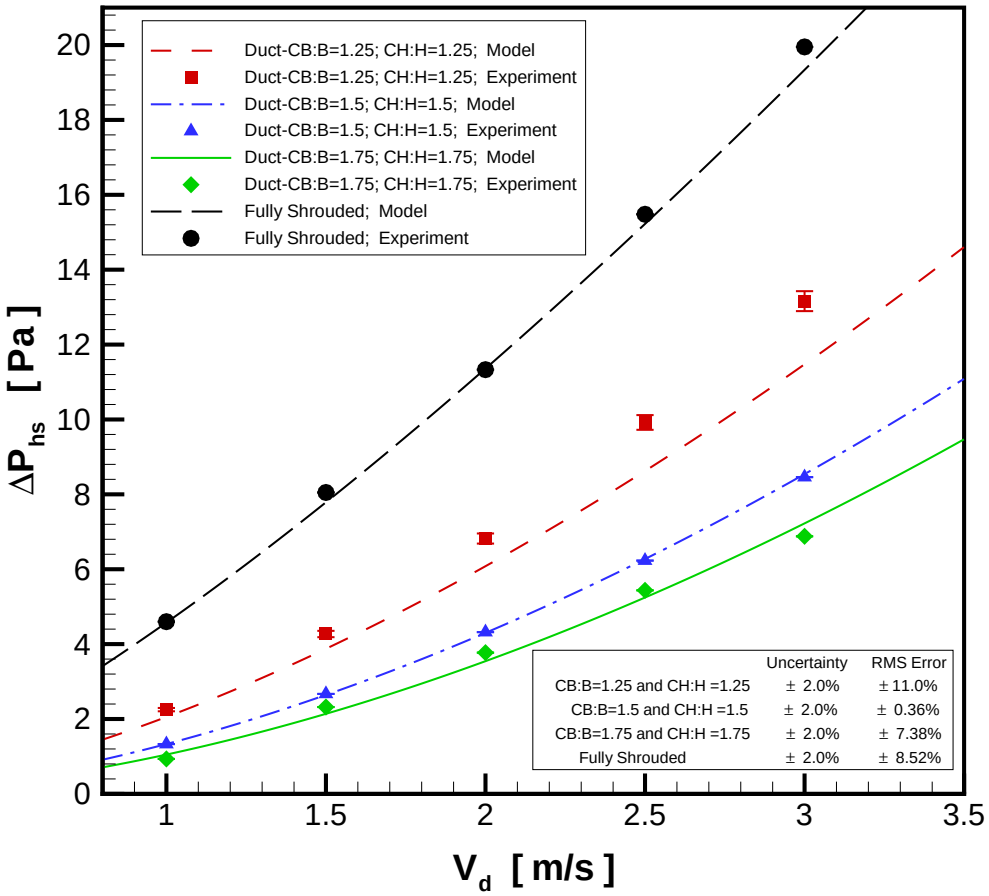

Figure 4.12: Validation of Bypass Model with Experimental Data for ΔP_{hs}

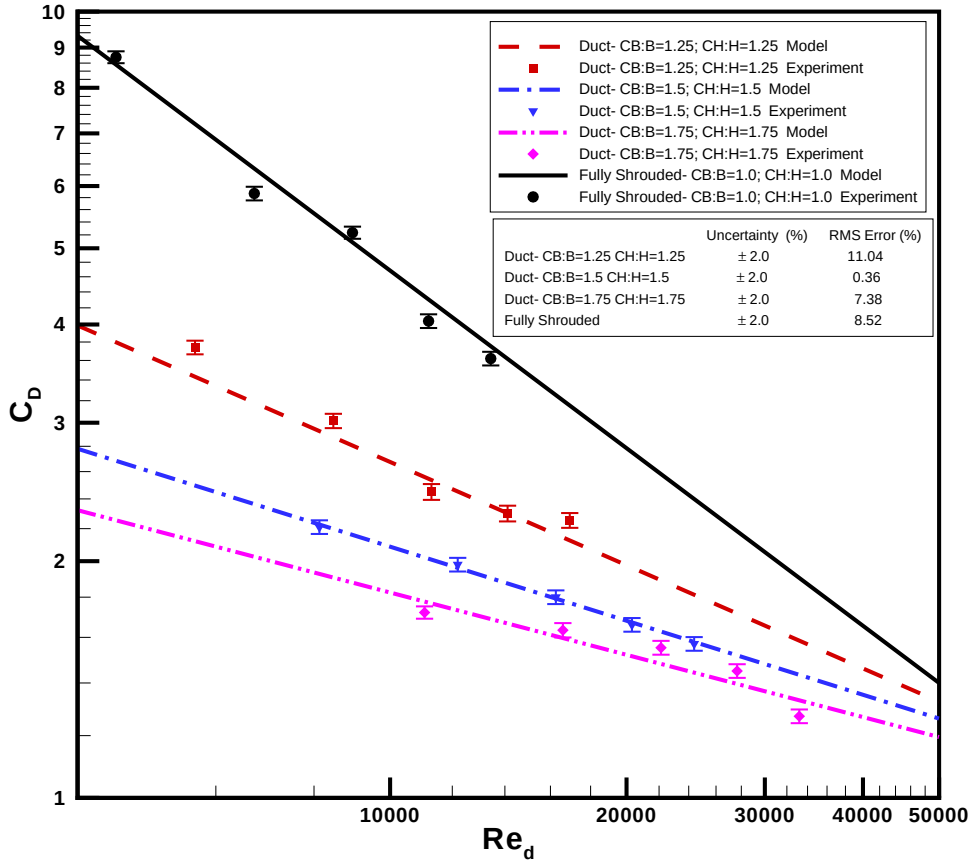

Figure 4.13: Validation of Bypass Model with Experimental Data for C_D

Figure 4.13 compares the bypass model for dimensionless pressure drop with experimental data for various duct Reynolds numbers, and it is found that the model data are in good agreement (RMS error ranging from 0.36% to 11.04%) with the experimental data. The experimental data exhibits an average uncertainty of $\pm 2\%$ because of the accuracy of the measurement apparatus.

Correlation of Channel Velocity, V_{ch}

Since Eq. 4.39 will be difficult to use in the optimization routine, V_{ch} is also correlated in Eq. 4.58 for use in the Entropy Generation Minimization Model.

The correlation of V_{ch} can be expressed by the following expression:

$$V_{ch} = V_d \quad \left(\frac{s+t}{s}\right)\left[1-\left(\left(\frac{1}{Re_d}\right)^{0.34}\left(\frac{D_{h_b}}{D_{h_{ch}}}\right)^{0.85}\right)^{\frac{s}{s+t}}\right] \tag{4.58}$$

where

$$\begin{aligned}
\text{Channel hydraulic diameter,} \quad D_{h_{ch}} &= 2s \\
\text{Duct Reynolds number,} \quad Re_d &= \frac{\rho V_d D_{h_d}}{\mu} \\
\text{Duct hydraulic diameter,} \quad D_{h_d} &= \frac{4CB \times CH}{2(CB+CH)} \\
\text{Bypass hydraulic diameter,} \quad D_{h_b} &= \frac{4(2A_{bs}+A_{bt})}{2P_{bs}+P_{bt}} \\
\text{Area of each side bypass,} \quad D_{h_{ch}} &= \frac{1}{2}(CB-B)\,H \\
\text{Area of top bypass,} \quad A_{bt} &= CB(CH-H) \\
\text{Perimeter of each side bypass,} \quad \mathcal{P}_{bs} &= \frac{1}{2}(CB-B)+2H \\
\text{Perimeter of top bypass,} \quad \mathcal{P}_{bt} &= (CB+B)+2(CH-H)
\end{aligned}$$

When bypass (D_{h_b}) becomes zero, Eq. 4.58 takes the form of conservation of mass for a single channel of the fully shrouded model.

$$V_{ch} = V_d \left(\frac{s+t}{s}\right)$$

Correlated values are found to be within $\pm 8\%$ of model data (Figs. 4.14 & 4.15).

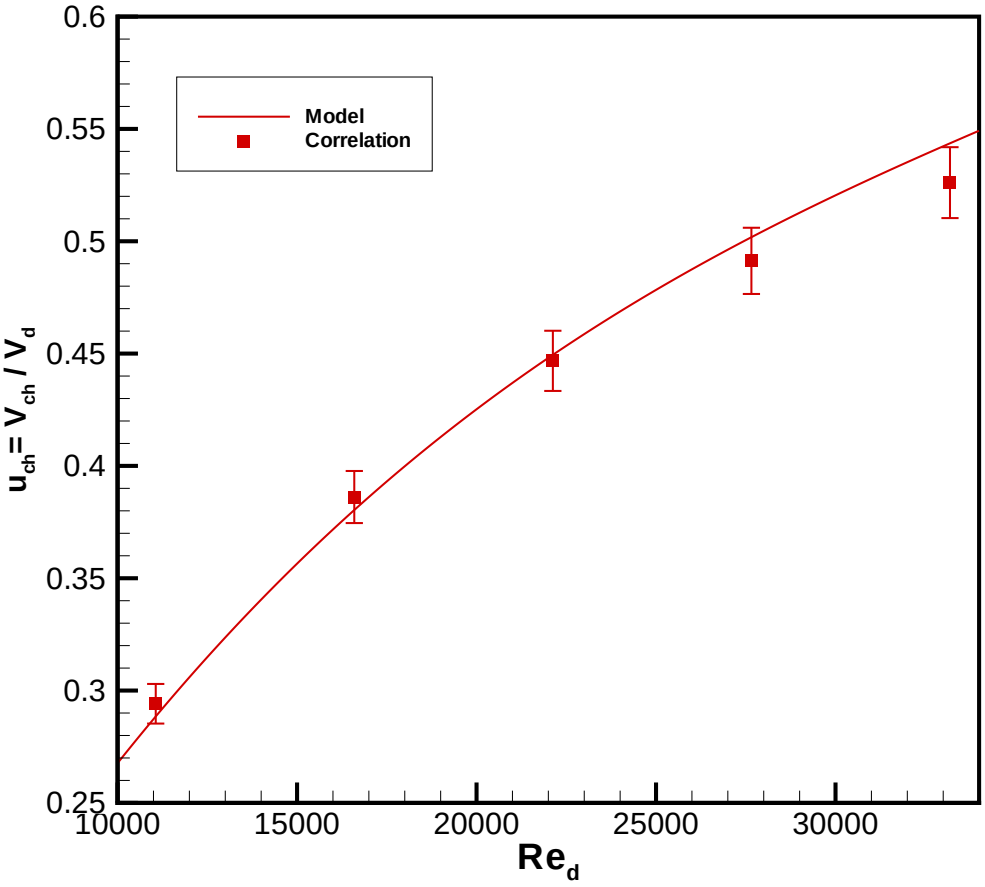

Figure 4.14: Validation of Correlated u_{ch} with Model for Various Re_d.

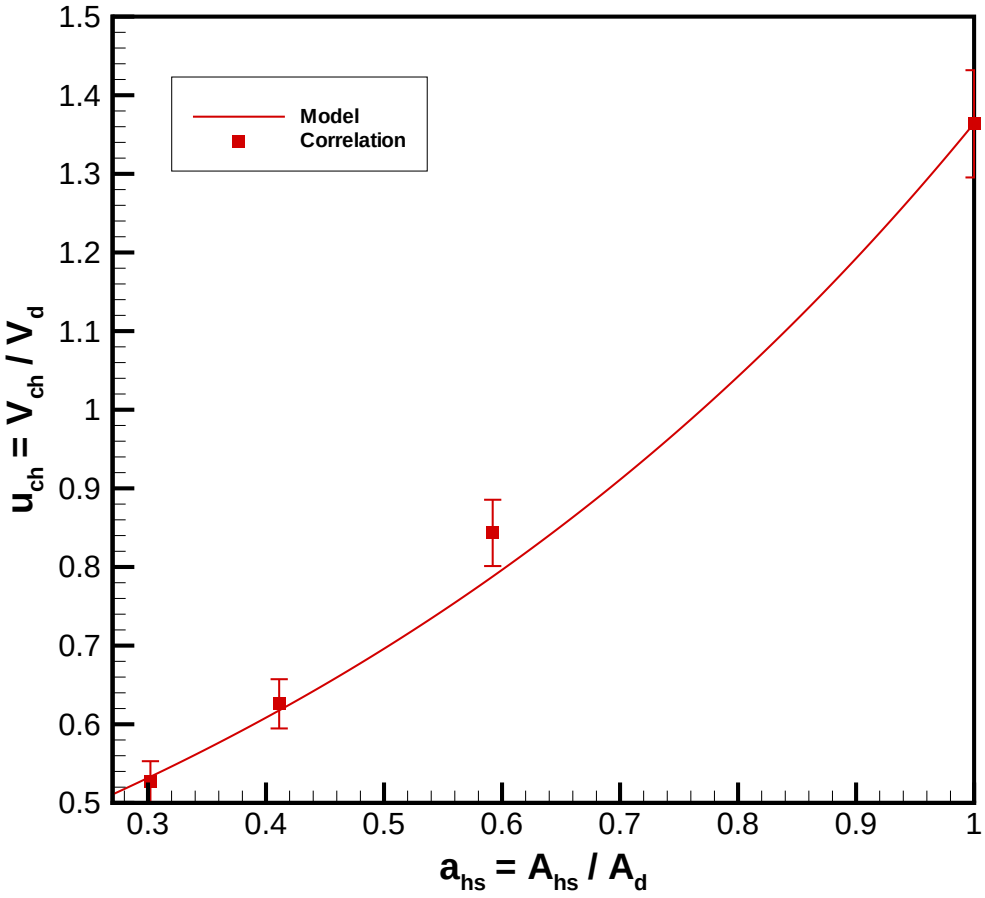

Figure 4.15: Validation of Correlated u_{ch} with Model for Various a_{hs}.

4.2.3 Comparison of Fluid Model - Earlier Literature

A thorough review of the literature revealed some experimental and numerical studies of different heat sink geometries, duct configurations and flow conditions for a good comparison with the present analytical model.

Butterbugh and Kang

Butterbugh and Kang (1995) conducted an experimental study with one sample heat sink to determine the thermal and hydraulic characteristics for various duct configurations and velocities. Their experimental setup and procedure were found almost similar to this research with a difference in the type of instruments and data management.

Table 4.1: Experimental Data (Fluid) of Butterbugh and Kang (1995)

CB-B	CH-(H+tb)	V_d	Fluid	Material		t_b	L	H	B	t	N	s	ΔP_{hs}
mm	mm	m/s		Base	Fin	mm	mm	mm	mm	mm		mm	Pa
0	25	1 2 3 4	Air	Al	Al	6	46	53	45	1.27	13	2.40	2.57 6.93 13 20.40
38	0	1 2 3 4	Air	Al	Al	6	46	53	45	1.27	13	2.40	1.76 5.62 10.50 17.40
51	25	1 2 3 4	Air	Al	Al	6	46	53	45	1.27	13	2.40	1.28 3.47 17.10 10.80

Table 4.1 shows the experimental data used by Butterbugh and Kang (1995). These data are used to compare the proposed model for pressure drop for different duct velocity and configurations. Figure 4.16 shows the comparison between the model data and experimental data of Butterbugh and Kang (1995).

The results of the model show good agreement with the experimental data with overall RMS errors ranging from 6% to 9%.

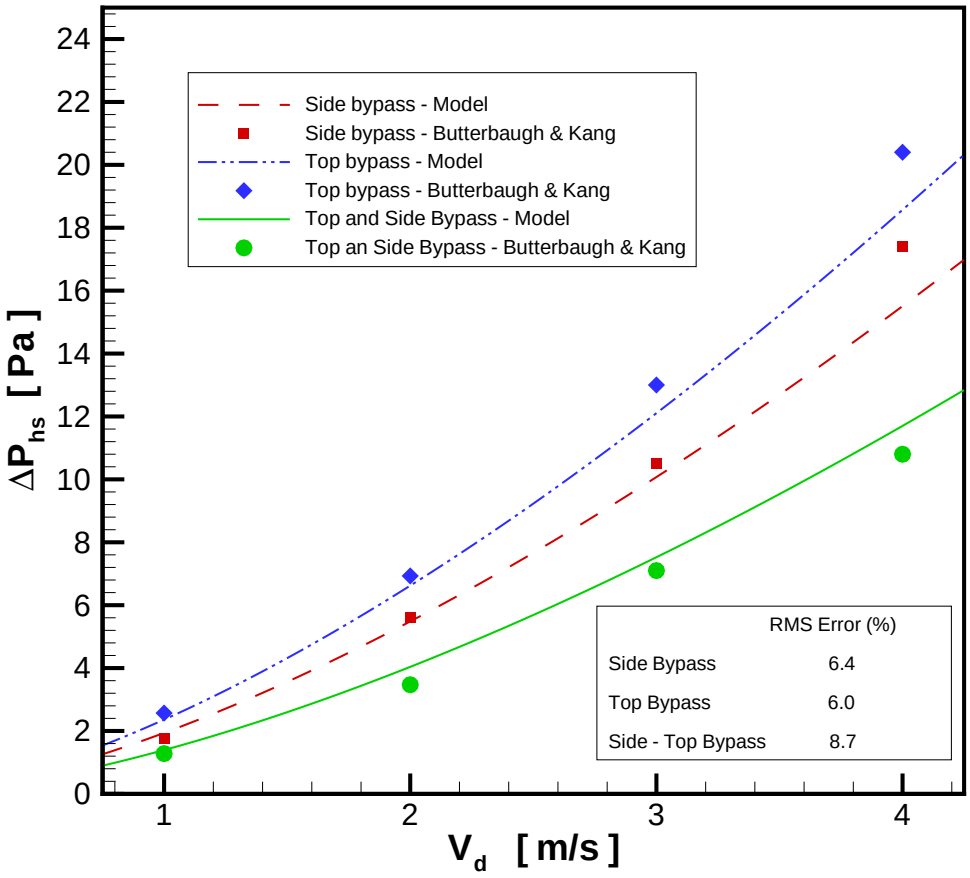

Figure 4.16: Validation of Bypass Model with Experimental Data of Butterbugh and Kang (1995).

Wirtz et al.

Wirtz et al. (1994) conducted an experiment in an open circuit wind tunnel to measure the thermal and hydraulic characteristics of various heat sinks for different duct configurations and Reynolds numbers (Re_L). Their experimental setup and procedure were found almost similar to this research; their flow results were not measured directly but backed out from the thermal measurements of a plate fin heat sinks for different Reynolds number (Re_L) and correlated to the following expression:

$$Re_{ch} = \left(\frac{D_{h_{ch}}}{L} Re_L\right)^{1+1.5D^2} e^{-11.8D^{2.15}} \tag{4.59}$$

where

$$\begin{aligned} Re_{ch} &= \frac{\rho V_{ch} D_{h_{ch}}}{\mu} \\ D_{h_{ch}} &= 2\,s \\ Re_L &= \frac{\rho V_d L}{\mu} \\ D &= \frac{Nt}{B} \end{aligned}$$

The influence of duct geometry, which plays an important role in flow bypass, was not included in the correlation.

Table 4.2: Experimental Data of Wirtz et al. (1994)

CB-B *mm*	CH-(H+tb) *mm*	V_d *m/s*	Fluid	Material		t_b *mm*	L *mm*	H *mm*	B *mm*	t *mm*	N	s *mm*	1-u_{ch}
				Base	Fin								
34	48	0.36	Air	Al	Al	4.06	56	25.60	56	2.33	12	2.55	0.57
		0.54											0.46
		0.90											0.38
		1.07											0.27
		1.43											0.22
		1.70											0.20

Table 4.2 shows the experimental data used by Wirtz et al. (1994) for development of their correlation for normalized bypass flow. These data are used to compare the proposed model for normalized bypass flow for different duct Reynolds numbers. Figure 4.17 shows the comparison between model and correlated data of Wirtz et al. (1994). The results of the model show RMS difference of 10.9% when compared with the correlated data. Wirtz et al. (1994) did not provide

any information regarding pressure drop across the heat sink in support of their work, which could have been an important information to compare the present model for pressure drop.

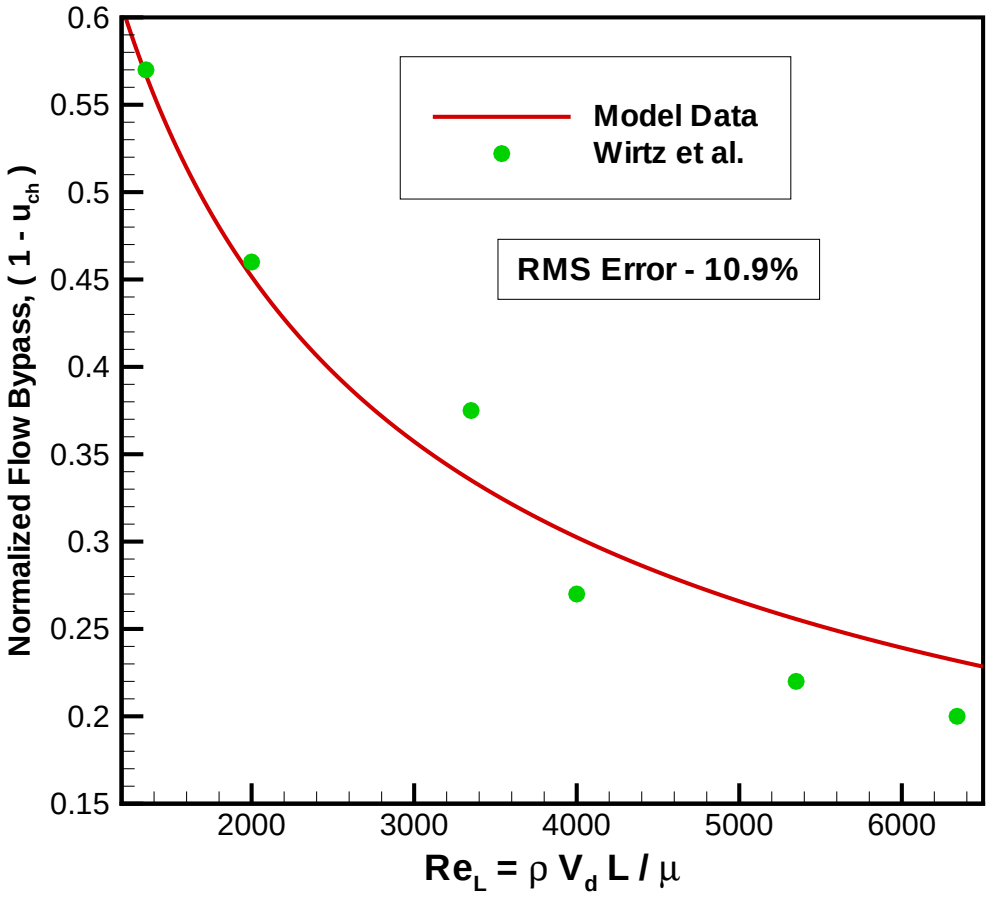

Figure 4.17: Validation of Model with Experimental Data of Wirtz et al. (1994).

Jonsson and Moshfegh

Jonsson and Moshfegh (2001) conducted experiments with various plate fin heat sinks of different fin heights (10, 15 and 20 mm), spacings (3, 5 mm) and fin numbers (12 and 9) for different duct configurations and Reynolds numbers (Re_d). Their experimental setup and procedure were found almost similar to this research with a difference in the type of instruments and data management.

Table 4.3: Experimental Data (Fluid) of Jonsson and Moshfegh (2001)

CB-B	CH-H	Re_d	Fluid	Material		L	H	B	t	N	s	ΔP_{hs}
mm	*mm*			Base	Fin	*mm*	*mm*	*mm*	*mm*		*mm*	*Pa*
		3350										0.80
		5000										1.5
10	40	6700	Air	Al	Al	52.8	20	52.8	1.42	9	5	1.90
		10000										3.72
		13400										5.93
		3350										0.40
		5000										0.65
50	40	6700	Air	Al	Al	52.8	20	52.8	1.42	9	5	1.04
		10000										1.85
		13400										2.87
		3350										0.30
		5000										0.51
107	40	6700	Air	Al	Al	52.8	20	52.8	1.42	9	5	0.82
		10000										1.38
		13400										2.18

Table 4.3 shows the experimental data used by Jonsson and Moshfegh (2001). These data are used to compare the proposed model for pressure drop. Figure 4.18 shows the comparison between the model and experimental data of Jonsson and Moshfegh (2001).

The results of the model show good agreement with the experimental data with overall RMS errors ranging from 5.5% to 11.5%.

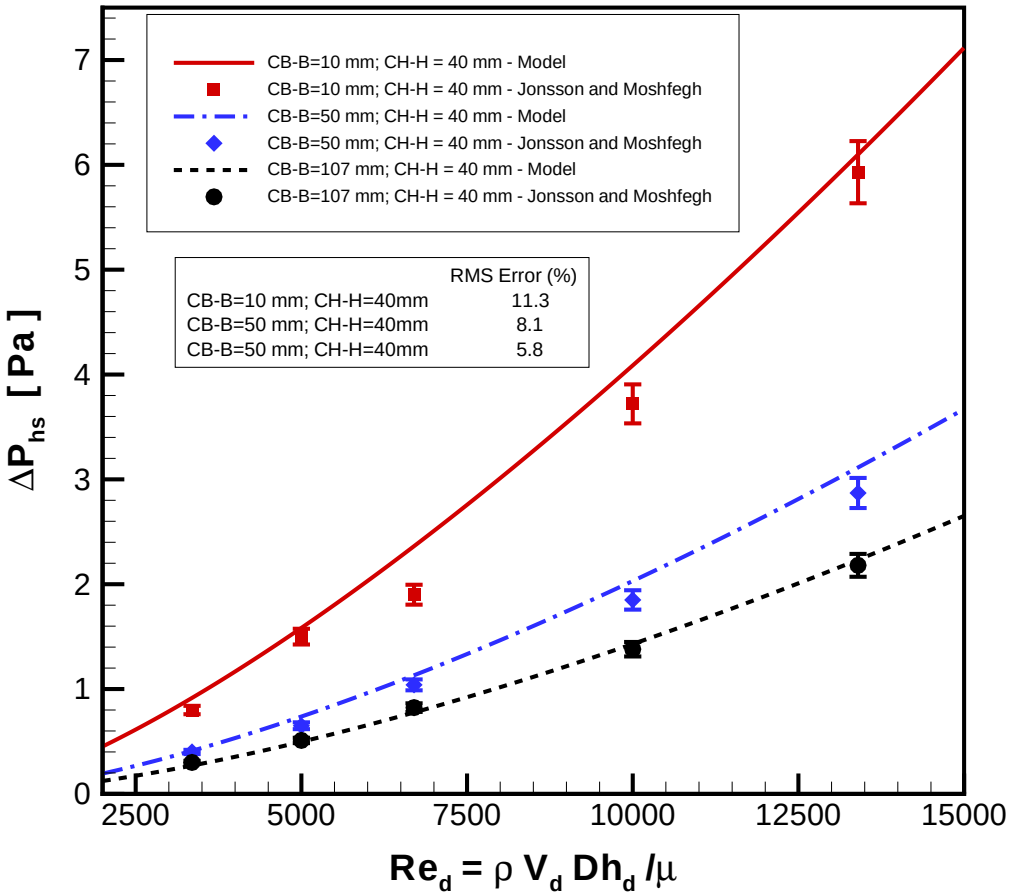

Figure 4.18: Validation of Bypass Model with Experimental Data of Jonsson and Moshfegh (2001).

Coetzer and Visser (2003)

Coetzer and Visser (2003) conducted a CFD modeling using the Flotherm CFD package to gain an understanding of the flow pattern and heat transfer of a heat sink with various tip clearances.

Table 4.4: Numerical Data (Fluid) of Coetzer and Visser (2003)

Sample	CB-B	CH-H	V_d	Fluid	Material		L	H	B	t	N	s	ΔP_{hs}
	mm	*mm*	*m/s*		Base	Fin	*mm*	*mm*	*mm*	*mm*	Guess	*mm*	*Pa*
HS-1	0	25	1 4 8 12	Air	Al	Al	150	53	41.6	1.27	12	2.4	4.1 28.95 85.43 156.32
HS-2	0	27	1 4 8 12	Air	Al	Al	150	20	41.6	5.0	5	5.0	1.53 13.56 41.24 81.43

Table 4.4 shows the numerical data used by Coetzer and Visser (2003). These data are used to compare the proposed model for pressure drop for various duct velocities and configurations. Figure 4.19 shows the comparison between model and numerical data of Coetzer and Visser (2003). The results of the model show good agreement with the numerical data with overall RMS errors ranging from 3.5% to 5.6%

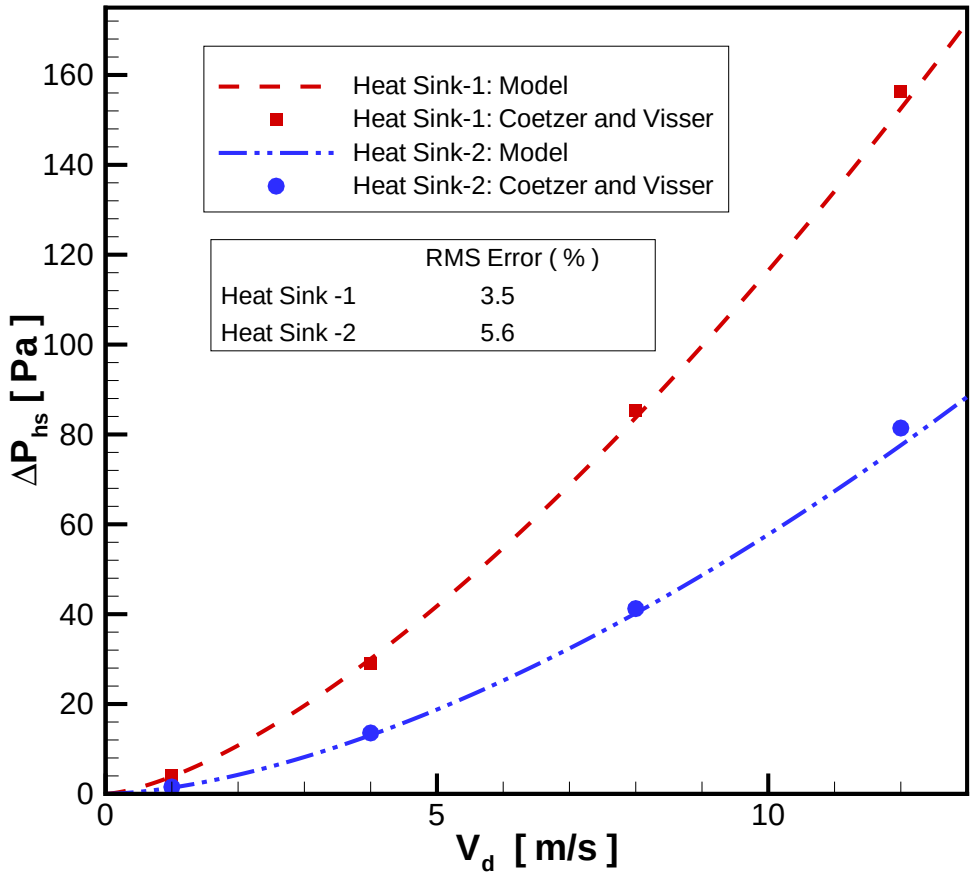

Figure 4.19: Validation of Bypass Fluid Model with Numerical Data of Coetzer and Visser (2003).

4.3 Heat Transfer Model

Forced-air cooling through the use of extended surfaces are being used as an attractive technique for cooling microelectronic devices due to its inherent simplicity and cost effectiveness. Designs incorporating such surfaces typically take the form of finned heat sinks. Typically heat sinks are directly mounted on the cases that enclose micro-electronic packages to provide extra surface area for heat transfer from the device to the cooling fluid. The heat dissipated in the package is conducted into the substrate and then transferred by some combination of thermal conduction, convection and radiation to the surrounding through the application of a heat sink.

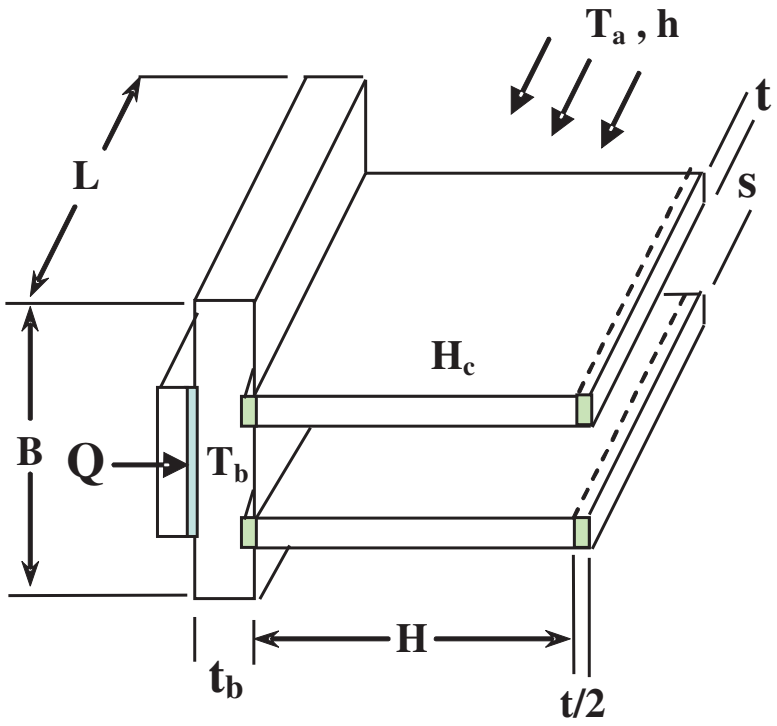

Figure 4.20: Heat Transfer with Rectangular Fin Arrays.

Heat sinks are typically designed based on a measure of thermal resistance to heat flow between the heat source and the surrounding cooling medium [Figs. 4.20 and 4.21].

$$R_{th} = \frac{T_b - T_a}{Q} = \frac{\theta_b}{Q} \tag{4.60}$$

R_{th} can be obtained from a resistor network formed between the heat source and the cooling medium.

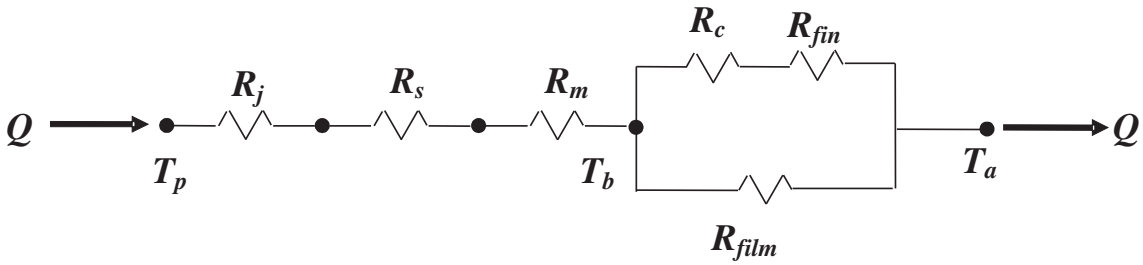

Figure 4.21: Thermal Circuit of Resistor Network

Based on the resistor network [Fig. 4.21], R_{th} can be expressed as:

$$R_{th} = R_j + R_s + R_m + \frac{1}{\frac{N}{R_c + R_{fin}} + \frac{1}{R_{film}}} \tag{4.61}$$

where N is the number of fins in the heat sink.

Heat transfer from package to heat sink base encounters a thermal resistance at the interface called thermal joint resistance, R_j because only a fraction of the total apparent area is in contact due to the surface irregularities at the interface face. Thermal joint resistance at the interface is a function of several geometric, physical and thermal parameters such as surface roughness and waviness, surface micro-hardness, thermal conductivity of the contacting solids, properties of the interstitial materials, and the contact pressure. Table B.1 of Appendix B shows that thermal joint resistance can be reduced to more than an order of magnitude smaller than the contact resistance of a bare joint by the application of a thin layer of a thermal interface material (TIM) at the interface. From Table B.2, it is also found that thermal joint resistance has a contribution of less than 1% to the total thermal resistance associated with a heat sink, therefore, it will be ignored in the heat transfer model

Spreading resistance (R_s) is ignored in most of the literature assuming package and heat sink base have same coverage area. But in most applications, package and heat sink coverage ratio is less than 50% which can generate significant spreading resistance and can influence the total thermal resistance. Therefore, R_s will be considered for this model.

Material resistance (R_m) depends on thermal property of the base material and geometry of the base and will be included in this model.

If fins are machined as an integral part of the wall from which they extend, there is no contact resistance (R_c) at the base. However, more commonly, fins are manufactured separately and are attached to the wall by a metallurgical or adhesive joint. Alternatively, the attachment may involve a press fit, for which the fins are pressed into slots machined on the wall material [Fig. 4.20]. In such cases, there exists a resistance called R_c and it is always in series with R_{fin} [Fig. 4.21]. From Table B.2, it is found that R_c is almost two order of magnitude smaller than R_{fin}, and it can be ignored in the heat transfer model.

R_{fin} and R_{film} can be represented by R_{hs} that accounts for parallel heat flow paths by conduction/convection in the fins and by convection from the exposed surface of the base.

$$R_{hs} = \frac{1}{\frac{N}{R_{fin}} + \frac{1}{R_{film}}} \tag{4.62}$$

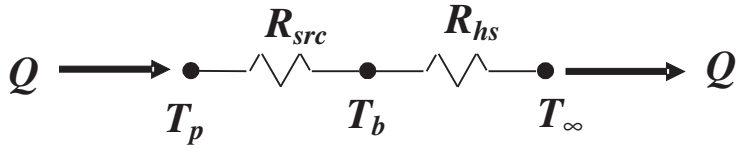

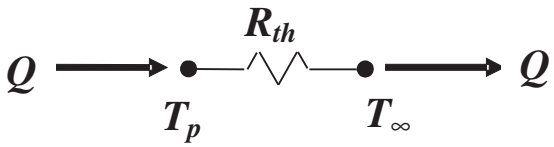

Figure 4.22: Reduced Thermal Circuit of Resistor Network

Based on the above assumptions, Eq. 4.61 can be reduced to the following equation as shown graphically in Fig. 4.22:

$$R_{th} = R_s + R_m + R_{hs} \tag{4.63}$$

4.3.1 Assumptions for Resistance Modelling

The modelling of R_s, R_s and R_{hs} will be based on the following limiting assumptions:

- The heat flow in the fin and its temperatures remain constant with time.
- The fin material is homogeneous and isotropic.
- The convective heat transfer coefficient on the faces of the fin is constant and uniform over the entire surface of the fin.
- The temperature of the medium surrounding the fin is uniform.
- The fin thickness is small, compared with its height and length, so that temperature gradients across the fin thickness and heat transfer from the edges of the fin may be neglected.
- The temperature at the base of the fin is uniform.
- There is no heat source within the fin itself.
- Heat transfer to or from the fin is proportional to the temperature excess between the fin and the surrounding medium.
- The radiation heat transfer is negligible
- The fluid is considered incompressible with constant properties.

4.3.2 Model of Spreading Resistance, $\mathbf{R}_s$

The spreading resistance is obtained from the model of Yovanovich et al. (1999) that shows the explicit and implicit relationships with the geometric and thermal parameters of the system.

$$\begin{aligned} R_s &= \frac{1}{2a^2cdk}\sum_{m=1}^{\infty}\frac{\sin^2(a\delta_m)}{\delta_m^3}\phi(\delta_m) \\ &+ \frac{1}{2b^2cdk}\sum_{n=1}^{\infty}\frac{\sin^2(b\lambda_n)}{\lambda_n^3}\phi(\lambda_n) \\ &+ \frac{1}{a^2b^2cdk}\sum_{m=1}^{\infty}\sum_{n=1}^{\infty}\frac{\sin^2(a\delta_m)\sin^2(b\lambda_n)}{\delta_m^2\lambda_n^2\beta_{m,n}}\phi(\beta_{m,n}) \end{aligned} \tag{4.64}$$

For a heat sink of foot print dimension L$(=2c)$ × B$(=2d)$ and a heat source dimension ℓ $(=2a)$ × ω $(=2b)$ the above equation becomes:

$$R_s = \frac{8}{LBk}\left[\frac{1}{\ell^2}\sum_{m=1}^{\infty}\frac{\sin^2\left(\frac{\ell}{2}\delta_m\right)}{\delta_m^3}\phi(\delta_m) + \frac{1}{w^2}\sum_{n=1}^{\infty}\frac{\sin^2\left(\frac{\omega}{2}\lambda_n\right)}{\lambda_n^3}\phi(\lambda_n)\right. \tag{4.65}$$

$$\left. + \frac{8}{\ell^2\omega^2}\sum_{m=1}^{\infty}\sum_{n=1}^{\infty}\frac{\sin^2\left(\frac{\ell}{2}\delta_m\right)\sin^2\left(\frac{\omega}{2}\lambda_n\right)}{\delta_m^2\lambda_n^2\beta_{m,n}}\phi(\beta_{m,n})\right]$$

where

$$\delta_m = \frac{2m\pi}{L}, \qquad \lambda_n = \frac{2n\pi}{B}, \qquad \beta_{m,n} = \sqrt{\delta_m^2 + \tau_n^2}$$

$$\zeta = \delta_m = \lambda_n = \beta_{m,n}$$

For an isotropic finite rectangular flux channel

$$\phi(\zeta) = \frac{\varphi e^{2\zeta t_b} + 1}{\varphi e^{2\zeta t_b} - 1}$$

$$\varphi = \frac{\zeta + \frac{Bi}{\mathcal{L}}}{\zeta - \frac{Bi}{\mathcal{L}}}$$

Lee et al. (1995) proposed the following correlation of the Yovanovich et al. (1999) model for spreading resistance. This correlation will be used in the optimization routine as the Yovanovich et al. (1999) model will be difficult to fit into the optimization routine.

$$R_s = \frac{\psi}{\sqrt{\pi}ka} \tag{4.66}$$

where

$$\psi = \frac{1}{2}(1-\varepsilon)^{\frac{3}{2}}\phi_c\,; \quad \phi_c = \frac{\tanh(\lambda_c\tau) + \frac{\lambda_c}{Bi}}{1 + \frac{\lambda_c}{Bi}\tanh(\lambda_c\tau)}\,; \quad \lambda_c = \pi + \frac{1}{\sqrt{\pi}\varepsilon}$$

$$\varepsilon = \frac{a}{b}\,; \qquad \tau = \frac{t_b}{b}\,; \qquad Bi = \frac{h\mathcal{L}}{k}$$

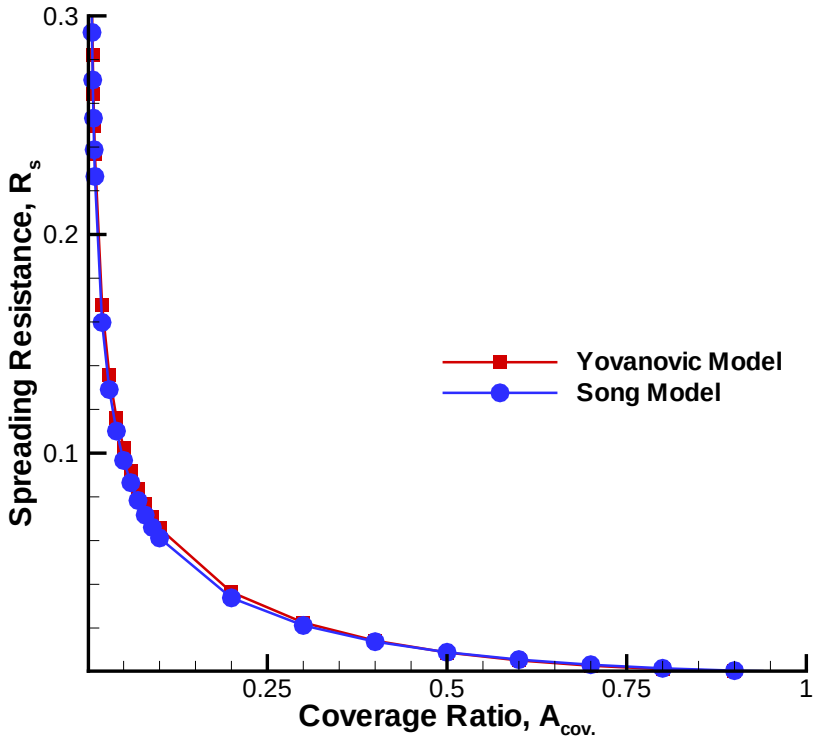

Figure 4.23: Comparison of Yovanovich et al. Model (1999) with the Correlation of Lee et al. (1995)

$$a = \sqrt{\frac{A_{sh}}{\pi}}\,; \qquad b = \sqrt{\frac{A_{bp}}{\pi}}\,; \qquad \mathcal{L} = \sqrt{\frac{A_t}{\pi}}$$

$$A_{sh} = \ell \times \omega\,; \qquad A_{bp} = L \times B\,; \qquad A_t = 2NLH + (N-1)\,sL$$

Figure 4.23 compares the correlated data of Lee et al. (1995) for spreading resistance with the model data of Yovanovich et al. (1999) and it is found that correlated data are within $\pm$ 5% of model data

4.3.3 Model of Material Resistance, $\mathbf{R}_m$

R_m is the conduction resistance encountered by the heat sink base, which depends on the thermal properties of the base material and the geometry of the base. It can be explained by the Fourier Law of Conduction.

$$R_m = \frac{t_b}{kA_{bp}} \tag{4.67}$$

where

$$A_{bp} = L \times B$$

4.3.4 Model of Heat Sink Resistance, $\mathbf{R}_{hs}$

Using the overall efficiency of a heat sink, R_{hs} can be written as:

$$R_{hs} = \frac{1}{\frac{N}{R_{fin}} + \frac{1}{R_{film}}} = \frac{1}{\eta_o h A_t} \tag{4.68}$$

where the overall heat sink efficiency,

$$\eta_o = 1 - \frac{NA_{sf}}{A_t}\left(1 - \eta_f\right) \tag{4.69}$$

In lieu of the somewhat cumbersome expression for heat transfer from a straight rectangular fin with an active tip, an approximate, yet accurate, prediction may be obtained by using the adiabatic tip result with a corrected fin length of the form $H_c = H + \frac{t}{2}$ for a rectangular fin. The correction is based on assuming equivalence between heat transfer from the actual fin with tip convection and heat transfer from a longer, hypothetical fin [Fig. 4.20] with an adiabatic tip [22]. Hence, with tip

convection, the fin efficiency may be approximated as:

$$\eta_f = \frac{\tanh(mH_c)}{mH_c} \tag{4.70}$$

$$m = \sqrt{\frac{h\mathcal{P}_f}{kA_{cf}}} \tag{4.71}$$

$$A_t = N \times A_f + A_{be}$$

$$A_f = 2H_cL$$

$$A_{be} = (N-1)\,sL$$

$$H_c = H + \frac{t}{2}$$

$$\mathcal{P}_f = 2\,(t+L)$$

$$A_{cf} = tL$$

The average heat transfer coefficient, h for the parallel plate heat sink will be computed using the model developed by Teerstra et al. (1999), which is found to be within 10% of the experimental data:

$$Nu_s = \frac{\tanh\sqrt{2Nu_i\frac{k_f}{k}\frac{H}{b}\frac{H}{t}\left(\frac{t}{L}+1\right)}}{\sqrt{2Nu_i\frac{k_f}{k}\frac{H}{b}\frac{H}{t}\left(\frac{t}{L}+1\right)}}Nu_i \tag{4.72}$$

where

$$Nu_s = \frac{hs}{k_f}$$

$$Nu_i = \left[\left(\frac{Re_s^*Pr}{2}\right)^{-3} + \left(0.664\sqrt{Re_s^*}Pr^{\frac{1}{3}} \times \sqrt{1+\frac{3.65}{\sqrt{Re_s^*}}}\right)^{-3}\right]^{-\frac{1}{3}}$$

$$Re_s^* = Re_s\left(\frac{s}{L}\right)$$

$$Re_s = \frac{\rho V_{ch} s}{\mu}$$

$$Pr = \frac{\mu C_p}{k_f}$$

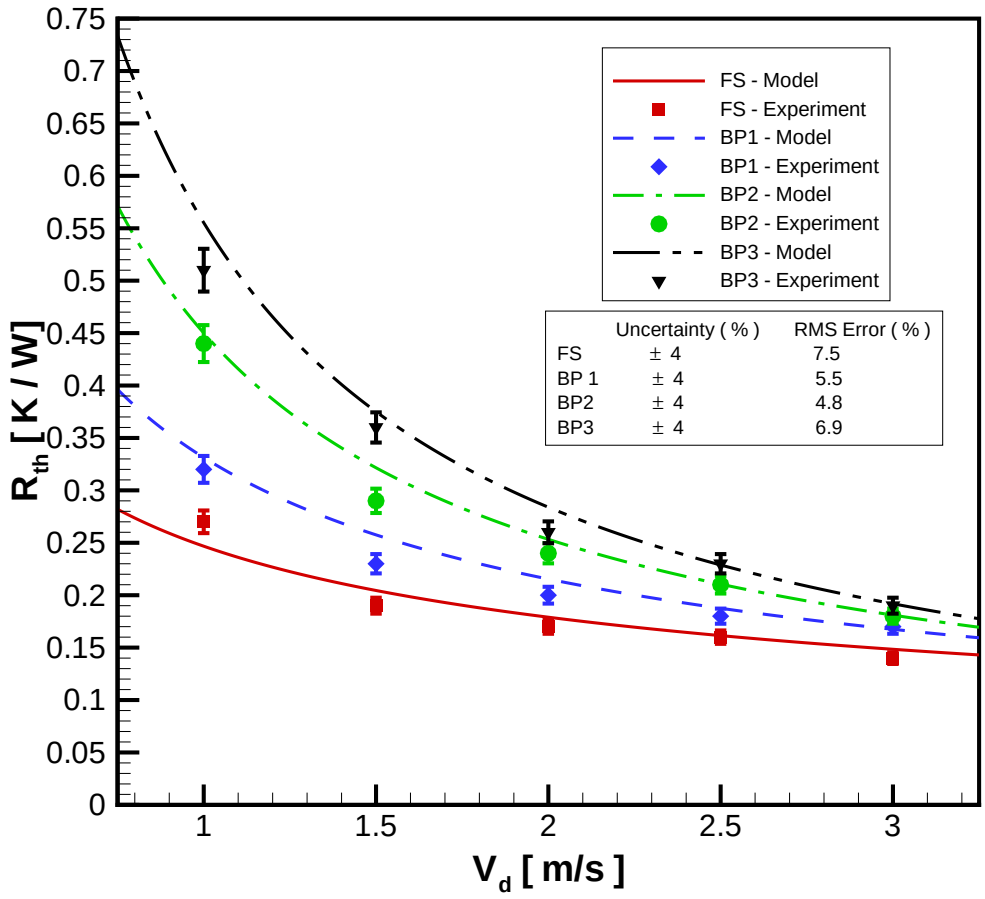

Figure 4.24: Model Validation for Thermal Resistance with Experimental Data.

Figure 4.24 compares the bypass model for thermal resistance with experimental data for various duct configurations and velocities, and it is found that the model data are in good agreement (RMS error ranging from 4.8% to 7.5%) with the experimental data. The experimental data exhibits an average uncertainty of $\pm 4\%$ because of the accuracy of the measurement apparatus.

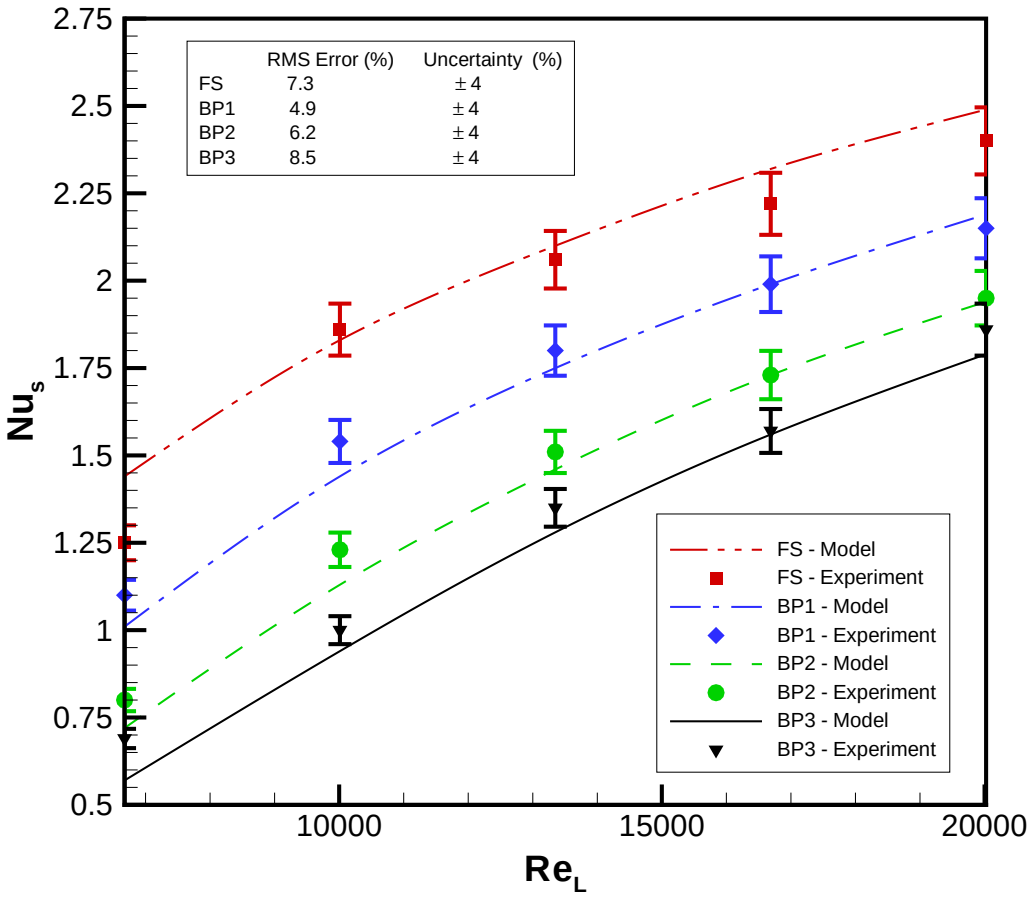

Figure 4.25: Model Validation for Nusselt Numbers with Experimental Data.

Figure 4.25 compares the bypass model for Nusselt number with experimental data for various duct configurations and Reynolds number (Re_L), and it is found that model data are in good agreement (RMS error ranging from 4.9% to 8.5%) with the experimental data. The experimental data exhibits an average uncertainty of $\pm 4\%$ because of the accuracy of the measurement apparatus.

4.3.5 Model Comparison - Earlier Literature

A thorough review of the literature revealed only a few experimental and numerical thermal studies of different heat sink geometries, duct configurations and flow conditions for a good comparison with the present model.

Jonsson and Moshfegh

Table 4.3 shows the experimental data used by Jonsson and Moshfegh (2001). These data are used to compare the proposed model for thermal resistance (R_{th}) for different duct Reynolds Numbers (Re_d) and configurations. In the literature, data for thermal resistance with bypass was not provided. The following correlation was proposed by Jonsson and Moshfegh (2001) to calculate the thermal resistance (R_{th}), which is reported within $\pm 10\%$ of the experimental data.

$$Nu_L = C_1 . \left(\frac{Re_d}{1000}\right)^{m1} . \left(\frac{CB}{B}\right)^{m2} . \left(\frac{CH}{H}\right)^{m3} . \left(\frac{s}{H}\right)^{m4} . \left(\frac{t}{H}\right)^{m5} \tag{4.73}$$

where

$$Re_D = \frac{\rho \omega D_{h_d}}{\mu}$$

the velocity, w, is given as:

$$w = \frac{A_d V_d}{A_d - N t H}$$

The correlation parameters (constants and exponents) are provided below in tabular form:

C_1	m_1	m_2	m_3	m_4	m_5
88.28	0.6029	-0.1098	-0.5632	0.08713	0.4139

The correlation is valid within the following limits:

Minimum	Variable	Maximum
1950	Re_D	16500
1.2	$\frac{CB}{B}$	3.1
1.5	$\frac{CH}{H}$	3
0.15	$\frac{s}{H}$	0.5
0.075	$\frac{t}{H}$	0.15

Figure 4.26 shows the comparison between the model and experimental data of Jonsson and Moshfegh (2001). The results of the model are in agreement with the experimental data with overall RMS errors ranging from 12.5% to 15.0%. The correlation proposed by Jonsson and Moshfegh (2001) for thermal resistance (R_{th}) was found in general within $\pm 10\%$ of the experimental data, that may be the cause of deviation of the model from their experimental correlation.

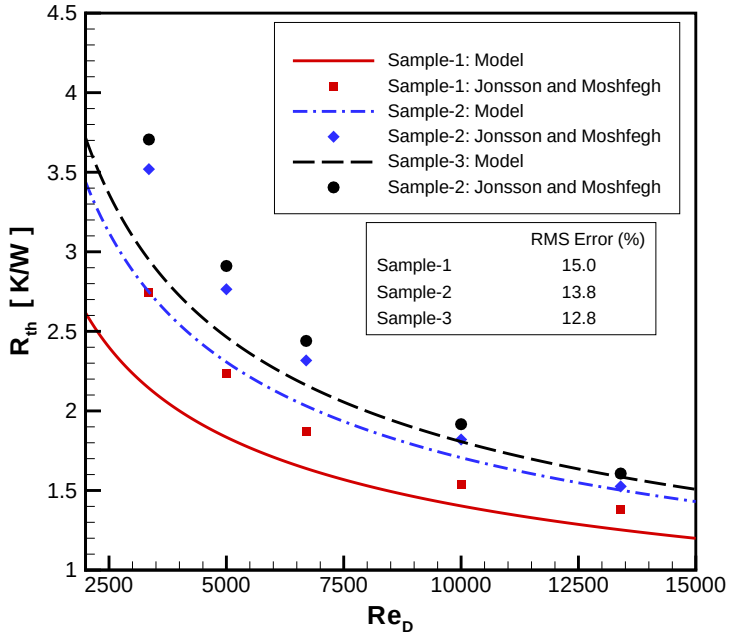

Figure 4.26: Thermal Model Validation with Experimental Correlation of Jonsson and Moshfegh (2001).

Butterbugh and Kang

Table 4.5 shows the experimental data used by Butterbugh and Kang (1995). These data are used to compare the proposed model of heat transfer for different duct velocities and configurations.

Table 4.5: Experimental Data (Thermal) of Butterbugh and Kang (1995)

CB-B	CH-(H+tb)	V_d	Fluid	Material		t_b	L	H	B	t	N	s	R_{th}
mm	mm	m/s		Base	Fin	mm	mm	mm	mm	mm		mm	K/W
0	25	1 2 3 4	Air	Al	Al	6	46	53	45	1.27	13	2.40	0.79 0.62 0.55 0.51
38	0	1 2 3 4	Air	Al	Al	6	46	53	45	1.27	13	2.40	0.91 0.66 0.58 0.52
51	25	1 2 3 4	Air	Al	Al	6	46	53	45	1.27	13	2.40	1.03 0.69 0.61 0.55

Figure 4.27 shows the comparison between model and experimental data of Butterbugh and Kang (1995). The results of the model show good agreement with the experimental data within an overall RMS errors of 2.5% to 5.0%.

From the review of the literature, it is found that the proposed model is very good in agreement with the pure experimental data of Butterbugh and Kang (1995) but deviates slightly from the correlated data of Jonsson and Moshfegh (2001).

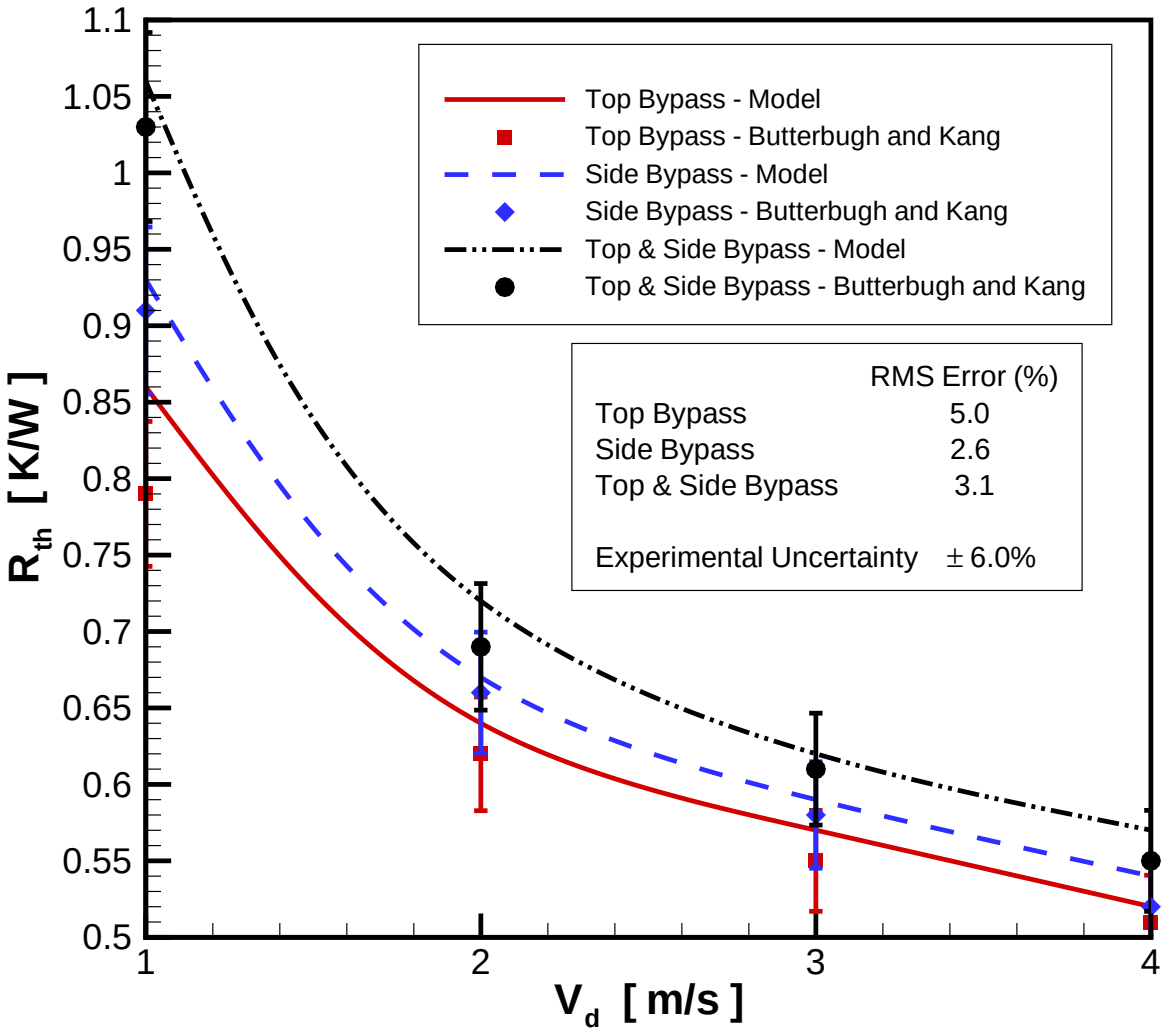

Figure 4.27: Bypass Thermal Model Validation with Experimental Data of Butterbugh and Kang (1995).

4.4 Entropy Generation Model

The Entropy Generation Model combines the basic principles of thermodynamics, heat and mass transfer, and fluid mechanics. It is the confluence of thermodynamics, heat transfer, and fluid mechanics [Fig. 4.28] because of its interdisciplinary character.

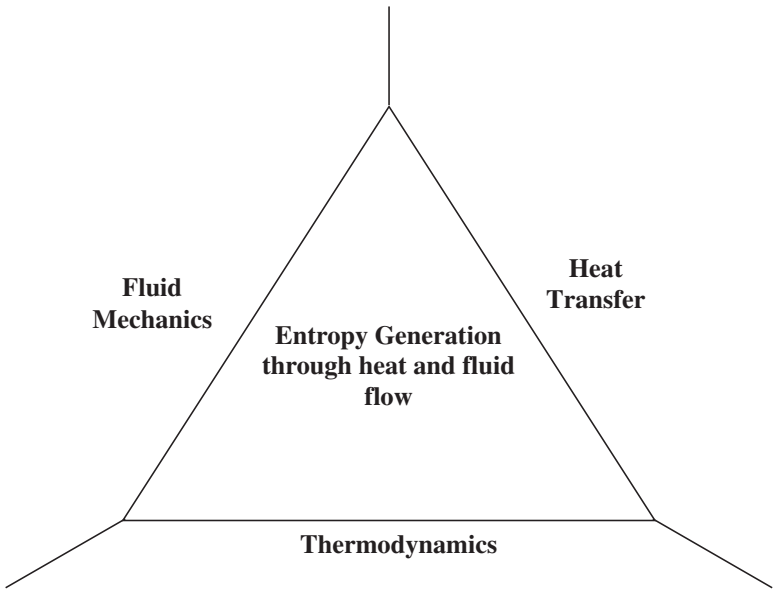

Figure 4.28: The interdisciplinary triangle covered by the Entropy Generation Model [8]

The entropy generation for extended surfaces is defined as the combination of the entropy generated due to fluid effects plus the entropy generated due to thermal effects in the following relationship:

$$\mathcal{S}_{gen} = \mathcal{S}_f + \mathcal{S}_t \tag{4.74}$$

where

$\mathcal{S}_f$ = Hydrodynamic Entropy Generation, expressed as:

$$\mathcal{S}_f = \frac{F_D V_d}{T_a} = \frac{A_d \Delta P_{hs} V_d}{T_a} = \frac{\forall_d \Delta P_{hs}}{T_a} \tag{4.75}$$

ΔP_{hs} can be obtained by using the model described in Section 4.2.

$\mathcal{S}_t$ = Thermal Entropy Generation, expressed as

$$\mathcal{S}_t = \frac{Q^2 R_{th}}{T_a^2} \tag{4.76}$$

R_{th} can be obtained by using the model described in Section 4.3.

Pressure drop and thermal resistance data measured from the experiment are used in Eq. 3.1 to calculate the experimental entropy generation and figure 4.29 compares the bypass model for entropy generation with experimental data for various duct configurations and velocities, and it is found that model data are in good agreement (RMS error ranging from 4.9% to 7.6%) with the experimental data. The experimental data exhibits an average uncertainty of $\pm 6\%$ because of the accuracy of the measurement apparatus.

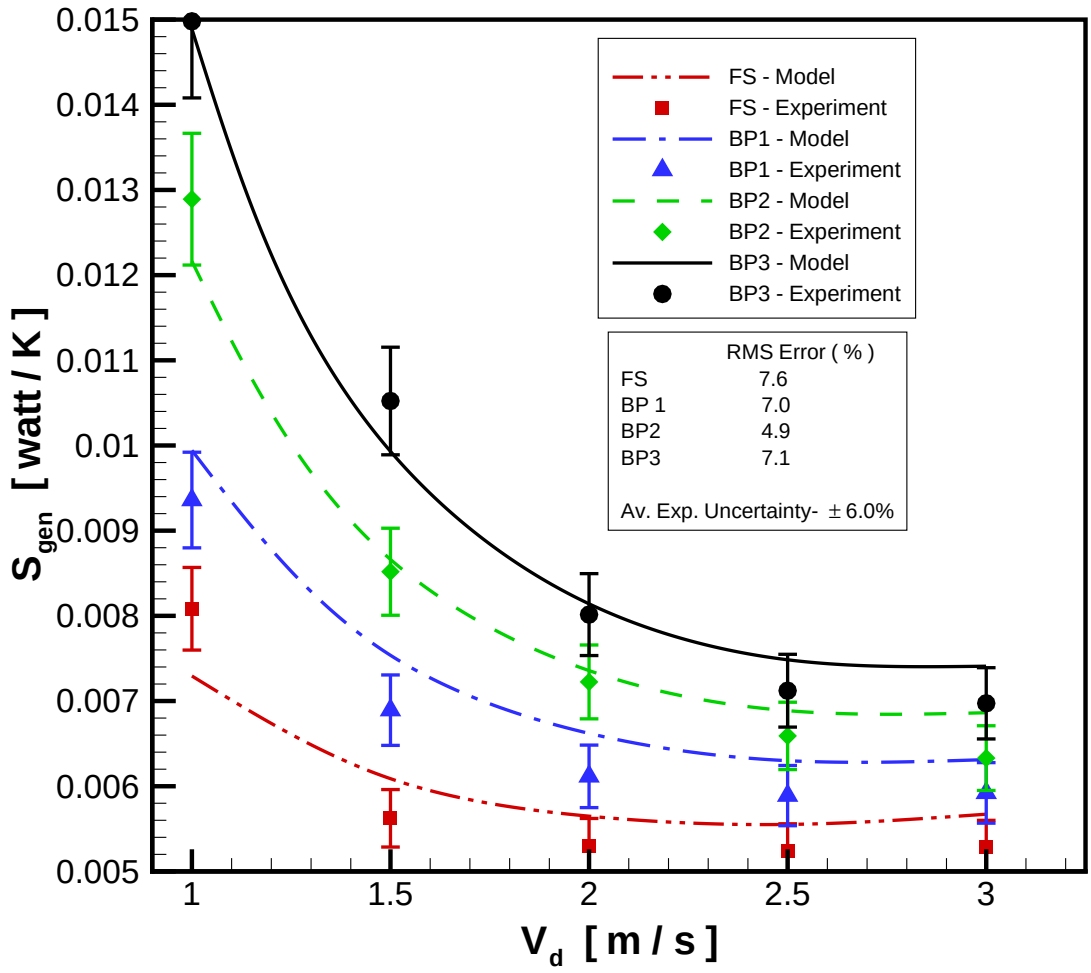

Figure 4.29: Validation of Data of Entropy Generation Model with that of Experiment

4.5 Summary

The Entropy Generation Model involves both fluid mechanics and heat transfer in the form of pressure drop and thermal resistance. As a result, a fluid model for pressure drop and a heat transfer model for thermal resistance have been developed and validated for designing a parallel plate heat sink under variable bypass conditions. The Entropy Generation Model will be discussed in the next chapter for designing an optimized heat sink by Entropy Generation Minimization (EGM).

Chapter 5

Entropy Generation Minimization (EGM)

Numerous analysis tools are available for determining the thermal performance of heat sinks given a well defined set of design conditions. Optimization routines that lead to changes in fin spacing, fin thickness, fin height, fin length, fin width or duct velocity also result in changes in the mean heat transfer coefficient and head loss in such a way that iterative procedures are required. While in some instances parametric studies can be undertaken to obtain a relationship between thermal performance and design parameters, a comprehensive design tool should also take into consideration the effect of viscous dissipation and its relationship on thermal performance. The entropy generation associated with heat transfer and frictional effects serve as a direct measure of lost potential for work or in the case of a heat sink, the ability to transfer heat to the surrounding cooling medium.

An optimization program is developed that establishes a relationship between the entropy generation associated with fluid friction and thermal resistance and heat sink design parameters in such a manner that all relevant design conditions combine to produce the best possible heat sink for optimum dimensions and performance within the given set of constraints.

5.1 Structure of Optimization Problems

Optimization problems require the minimization of a real-valued function $f(x)$ of an N-component vector argument $x = (x_1, x_2, \cdots, x_N)$ whose values are restricted to satisfy a number of real-valued equations $h_k(x) = 0$, a set of inequalities $g_j(x) \geq 0$, and the variable bounds $x_i^{(U)} \geq x_i \geq x_i^{(L)}$

The general optimization problem:

$$
\begin{array}{lllllll}
\text{Minimize} & f(x) & & & & & \\
\text{Subject to} & h_k(x) & = & 0 & & k & = & 1, \cdots, K \\
& g_j(x) & \geq & 0 & & j & = & 1, \cdots, J \\
& x_i^{(U)} & \geq & x_i & \geq & x_i^{(L)} & \text{i} & = & 1, \cdots, N
\end{array}
$$

where

$$
\begin{aligned}
f(x) &: \text{Objective Function} \\
h_k(x) = 0 &: \text{Equality Constraint} \\
g_j(x) \geq 0 &: \text{Inequality Constraint} \\
x_i^{(U)} \geq x_i \geq x_i^{(L)} &: \text{Bounds (Range) for Variables}
\end{aligned}
$$

5.2 Strategies for Optimization Program

In order to apply mathematical results and numerical techniques of optimization theory it is necessary to clearly define the performance criteria for which optimized values will be determined, to select the system variables, to define a model that will express the manner in which variables are related and to select the system requirements or constraints for which optimized values will be satisfied.

The strategies for an optimization program can be outlined as:

1. Performance Criterion
2. System Model
3. Selection of Variables and Parameters
4. System Requirement or Constraints

5.2.1 Performance Criterion

A performance criterion is needed to judge whether or not a given design is better than another. This criterion is called the objective function. A valid objective function must be influenced by the variables of the design problem. Selection of a proper objective function is an important decision in the design process; it can be minimum cost, maximum profit, minimum weight, minimum energy expenditure, minimum entropy generation associated with the system etc.

Based on the analyses of the preceding chapters, Entropy Generation (EG) associated with the thermal resistance and viscous dissipation in a heat sink is considered as the objective function of this optimization program.

5.2.2 System Model

Once the performance criterion have been established, the next step is to assemble the model that describes the manner in which the problem variables relate and the way in which the performance criterion is influenced by the variables. A model is the simplified mathematical representation of the system in consideration. A simplified form of an EGM model developed in earlier chapters will be used as a model for this optimization program.

Entropy Generation Model

Using Sction 4.4, entropy generation can be explained by the following expression:

$$\mathcal{S}_{gen} = \mathcal{S}_f + \mathcal{S}_t \tag{5.1}$$

where

$$\begin{aligned} \mathcal{S}_f &= \text{entropy generation associated with fluid viscous dissipation} \\ \mathcal{S}_t &= \text{entropy generation associated with thermal resistance} \end{aligned}$$

$\mathcal{S}_f$ can be expressed as:

$$\mathcal{S}_f = \frac{\forall_d \times \Delta P_{hs}}{T_a} \tag{5.2}$$

$\forall_d \times \Delta P_{hs}$ can also be referred to as fan power, P_{FP}.

and $\mathcal{S}_t$ can be expressed as:

$$\mathcal{S}_t = \frac{Q^2 R_{th}}{T_a^2} \tag{5.3}$$

ΔP_{hs} can be obtained from subsubsection 4.2.2 of Chapter 4, and the basic equations are shown in Table 5.1.

Table 5.1: Basic Equations for Pressure Drop Model

Equation			Function
ΔP_{hs}	=	$\left(K_c\,\sigma^2 + K_e + \dfrac{4\,f_{app_{ch}}\,L}{Dh_{ch}}\right)\dfrac{1}{2}\,\rho\,V_{ch}^2$	f(H.S. Geometry)
K_c	=	$1.18 + 0.0015\,\sigma - 0.395\,\sigma^2$	$= f\,(L,H,B,t,s,N,t_b)$
K_e	=	$1 - 2.76\,\sigma + \sigma^2$	f(Duct Geometry)
$f_{app_{ch}}$	=	$\dfrac{1}{Re_{ch}}\left[\left(\dfrac{3.44}{\sqrt{L_{ch}^*}}\right)^2 + \left(\dfrac{24}{1+\alpha_{ch}}\right)^2\right]^{\frac{1}{2}}$	$= f\,(CB,CH)$
V_{ch}	=	$\dfrac{V_d}{\sigma}\left[1 - \left(\left(\dfrac{1}{Re_d}\right)^{0.34}\left(\dfrac{Dh_b}{Dh_{ch}}\right)^{0.85}\right)^{\sigma}\right]$	f(Fluid Property)
			$= f\,(\rho,\mu)$
			f(Flow Condition)
			$= f\,(\forall_d)$

From Table 5.1, ΔP_{hs} is found as:

$$\Delta P_{hs} = f(L,H,B,t,s,t_b,CB,CH,\rho,\mu,\forall_d) \tag{5.4}$$

From Section 4.3, R_{th} can be expressed by the following expression:

$$R_{th} = R_{hs} + R_s + R_m \tag{5.5}$$

R_s, R_m and R_{hs} can be obtained from subsubsection 4.3.2, 4.3.3 and 4.3.4 of Chapter 4, and the basic equations are shown in Table 5.2.

Table 5.2: Basic Equations for Thermal Resistance Model

Equation			Function
R_s	=	$\dfrac{\psi}{\sqrt{\pi}ka}$	$f(\text{Source Geometry}) = f(\ell, \omega)$
ψ	=	$\dfrac{1}{2}(1-\varepsilon)^{\frac{3}{2}}\phi_c$	$f(\text{H.S. Material} = f(k)$
ϕ_c	=	$\dfrac{\tanh(\lambda_c\tau)+\dfrac{\lambda_c}{Bi}}{1+\dfrac{\lambda_c}{Bi}\tanh(\lambda_c\tau)}$	$f(\text{H.S. Geometry}) = f(B,L,H,s,t,t_b)$
λ_c	=	$\pi+\dfrac{1}{\sqrt{\pi}\varepsilon}$	$f(h) = f(L,H,s,t,D_{h_{ch}},\rho,\mu,k_f,Pr,V_{ch})$
Bi	=	$\dfrac{h\mathcal{L}}{k}$	$f(V_{ch}) = f(CB,CH,B,L,H,s,t,t_b,\forall_d,\rho,\mu)$
R_m	=	$\dfrac{t_b}{kA_{b\_hs}}$	
R_{hs}	=	$\dfrac{1}{\eta_o h A_t}$	
η_o	=	$1 - \dfrac{NA_{sf}}{A_t}(1-\eta_f)$	
η_f	=	$\dfrac{\tanh(mH_c)}{mH_c}$	

⋯continued

Table 5.3: Continuation of Table 5.2

Equation
$m = \sqrt{\frac{hP_f}{kA_{cf}}}$
$h = \frac{Nu_s k_f}{s}$
$Nu_s = \frac{\tanh\sqrt{2Nu_i \frac{k_f}{k}\frac{H}{b}\frac{H}{t}\left(\frac{t}{L}+1\right)}}{\sqrt{2Nu_i \frac{k_f}{k}\frac{H}{b}\frac{H}{t}\left(\frac{t}{L}+1\right)}} Nu_i$
$Nu_i = \left[\left(\frac{Re_s^* Pr}{2}\right)^{-3} + \left(0.664\sqrt{Re_s^*}Pr^{\frac{1}{3}} \times \sqrt{1+\frac{3.65}{\sqrt{Re_s^*}}}\right)^{-3}\right]^{-\frac{1}{3}}$
$Re_s^* = Re_s\left(\frac{s}{L}\right)$
$Re_s = \frac{\rho V_{ch} s}{\mu}$

From Tables 5.2 and 5.3, R_{th} is found as:

$$R_{th} = f(L,H,B,t,s,t_b,CB,CH,\rho,\mu,\forall_d,\ell,\omega,k,Pr) \tag{5.6}$$

From Tables 5.1, 5.2 and 5.3, Eq. 5.1 can be written as:

$$\mathcal{S}_{gen} = f(\text{H.S.G., D.G., P.G., H.S.M., Fl.P., F.C., S.P.}) \tag{5.7}$$

$$\begin{aligned}
\text{H.S.G. (Heat Sink Geometry)}, &= f(t,s,t_b,B,L,H) \\
B &= f(N,t,s) \\
\text{D.G. (Duct Geometry)}, &= f(CB,\, CH) \\
\text{P.G. (Package Geometry)}, &= f(\ell,\omega) \\
\text{H.S.M (Heat Sink Material)}, &= f(k) \\
\text{Fl.P. (Fluid Property)}, &= f(\rho,\, \mu,\, C_p,\, k_f) \\
\text{F.C. (Flow Condition)}, &= f(\forall_d,\, T_a) \\
\text{S.P. (System Property)}, &= f(Q)
\end{aligned}$$

From Eq. 5.7, it is found that $\mathcal{S}_{gen}$ is a function of heat sink geometry (N, t, s, t_b, B, L, H), duct geometry (CB, CH), package geometry (ℓ, ω), heat sink material (k), cooling fluid property (ρ, μ, C_p, k_f), flow condition ($\forall_d$, T_a) and system property (Q).

5.2.3 Selection of Variables and Parameters

It is necessary to distinguish between variables whose values influence the operation of the system or affect the design definition, known as decision variables and variables whose values are fixed by external factors, known as parameters.

A heat sink is normally designed based on the system requirement, therefore, heat load (Q) and source area ($\ell \times \omega$) must be fixed prior to designing a heat sink and can be treated as parameters.

Selection of the cooling fluid depends on the requirement of application, therefore, properties (ρ, μ, C_p, k_f) of the cooling fluid are fixed for a particular application and can be considered as parameters.

Selection of the heat sink material is normally based on thermal property (k), cost, weight and machinability, and the material is fixed prior to the design of a heat sink. Therefore, thermal conductivity (k) is also considered as parameter.

T_a is ambient temperature and assumed as a parameter.

Duct dimensions (CB and CH) are fixed for a particular application and assumed as parameters.

The remaining variables (t, s, t_b, B, L, H, V_d) of Eq. 5.7 will be treated as decision variables.

5.2.4 Selection of System Requirement or Constraints

All restrictions placed on a design are collectively called constraints which include limitation on space, performance, geometry, response of the system etc. The constraints are influenced by the decision variables, because only then can they be imposed. If a design satisfies all constraints, then a system can be identified as feasible (workable). Some constraints are quite simple, such as minimum and maximum values of decision variables, while more complex ones may be indirectly influenced by decision variables. Design problems may have equality as well as inequality constrains. A feasible design with respect to an equality constraint, however, must lie on its surface, therefore, the number of equality constraints can not be more than the decision variables. The feasible region for the inequality constraints is much larger than for the same constraint expressed as an equality. It is easier to find feasible designs for a system having only inequality constraints, there is no restriction on number of inequality constraints in optimization model.

The EGM Model has both equality and inequality constraints, which are described below.

Equality Constraint

The EGM Model has one equality constraint which is developed from the conservation of energy and must be satisfied during development of an optimum design.

Conservation of energy can be defined as:

$$Q_{in} = Q_{out}$$

where Q_{in} is the heat input Q from the package to the heat sink and Q_{out} must be equal to Q in order to ensure conservation of energy.

Q_{out} can be obtained by the following relationships:

$$\begin{aligned} Q_{out} &= \rho A_{ch} V_{ch} C_p (T_m - T_a) = \dot{m}_{ch} C_p (T_m - T_a) \\ T_m &= \frac{T_b + T_a}{2} \\ T_b &= R_{th} Q + T_a \end{aligned}$$

where T_a is a parameter and R_{th} can be obtained from the values of decision variables.

The equality constraint is expressed as:

$$h_1(Q) = Q - Q_{out} = 0 \tag{5.8}$$

Inequality Constraint

The EGM model has many simple inequality constraints that are related with the bound (maximum and minimum values) of the variables and some complex inequality constraints. Complex inequality constraints are described first:

Air flow rate inside the system is restricted by the capacity of the fan because of the nature of the application, and it is expressed as:

$$\forall_d \leq \forall_{Fan}$$

The inequality constraint associated with the duct flow rate is expressed as:

$$g_1(\forall_d) = \forall_d - \forall_{Fan} \leq 0 \tag{5.9}$$

The fin efficiency (η_f) is associated with the fin geometry and determines the performance of a fin or a heat sink. The efficiency of a fin is normally expected to be more than 75 %. The inequality constraint associated with η_f can be expressed as:

$$g_2(\eta_f) = 0.75 - \eta_f \leq 0 \tag{5.10}$$

The heat sink needs at least two fins to form a plate fin heat sink, and the fin number (N) in a plate fin heat sink is calculated as:

$$N = \frac{B + s}{s + t}$$

Inequality constraint associated with N can be expressed as:

$$g_3(N) = 2 - N \leq 0 \tag{5.11}$$

Other inequality constraints are simple and associated with the bounds of variables. t, s, t_b, H and V_d must be greater than zero, L must be greater than or equal to ℓ and B must be greater than or equal to w. L, B, H and t_b can also be limited to a certain maximum value because of the space and weight restriction associated with the system in consideration. Inequality constraints associated with bounds are given as:

$$g_4(B) = \omega - B \leq 0 \tag{5.12}$$

$$g_5(B) = B - B_d \leq 0 \tag{5.13}$$

$$g_6(L) = \ell - L \leq 0 \tag{5.14}$$

$$g_7(L) = L - L_d \leq 0 \tag{5.15}$$

$$g_8(H) = H - H_d \leq 0 \tag{5.16}$$

$$g_9(t_b) = t_b - t_{b_d} \leq 0 \tag{5.17}$$

where L_d, B_d, H_d and t_b are the upper bound for L, B, H and t_b because of the space and weight restriction.

Table 5.4 shows the optimization structure of the EGM Model.

5.3 Optimization Concept

From Table 5.4, it is clear that the EGM model deals with a nonlinear objective function with both equality and inequality constraints. The optimization routine will be run in Maple Mathematical Software that uses the Box's Complex Method nonlinear programming (NLP) procedure based on Kuhn-Tucker's theory of nonlinear optimization with both equality and inequality constraints.

Table 5.4: Optimization Structure of EGM Model

Objective Function	$f(\mathcal{S}_{gen})$ – Non Linear	
Decision Variables	Heat Sink Geometry	t, s, t_b, B, L, H
	Duct Velocity	V_d
Parameters	Heat Input	Q
	Heat Sink Material	k
	Cooling Fluid Property	ρ, μ, C_p , k_f
	Package Geometry	ℓ, ω
	Duct Geometry	CB, CH
	Ambient Temperature	T_a
Equality Constraint	Equation 5.8	
Inequality Constraints	Equations 5.9 to 5.17	

The theory of Kuhn-Tucker addresses the following general problem of NLP:

$$\begin{aligned}
&\text{Minimize} && f(x) && && \\
&\text{Subject to} && h_k(x) &= 0 && k &= 1,2,\cdots,K \\
& && g_j(x) &\geq 0 && j &= 1,2,\cdots,J \\
& && x &= (x_1, x_2, \cdots, x_N) && &
\end{aligned}$$

The Kuhn-Tucker theory finds vectors $x_{(n\times 1)}$, $u_{(1\times J)}$, and $v_{(1\times K)}$ for the given problem that satisfies the following conditions:

$$\nabla f(x) - \sum_{j=1}^{J} u_j \nabla g_j(x) - \sum_{k=1}^{K} v_k \nabla h_k(x) = 0 \tag{5.18}$$

$$\begin{aligned} h_k(x) &= 0 \qquad \text{for } k = 1,2,\cdots,K \\ g_j(x) &\geq 0 \qquad \text{for } j = 1,2,\cdots,J \\ u_j g_j(x) &= 0 \qquad \text{for } j = 1,2,\cdots,J \\ u_j &\geq 0 \qquad \text{for } j = 1,2,\cdots,J \end{aligned}$$

where u_j and v_k are Kuhn-Tucker multipliers for inequality and equality constraints.

For notational convenience the decision variables of this optimization problem can be redefined as follows in terms of x:

$$x = (x_1, x_2, x_3, x_4, x_5, x_6, x_7) = (t, s, t_b, B, L, H, V_d)$$

Constraints can be redefined as:

Equality constraint:

$$h_1(x) = Q - Q_{out} = 0 \tag{5.19}$$

Inequality constraints:

$$g_1(x) = \forall_d - \forall_{Fan} \leq 0 \tag{5.20}$$

$$g_2(x) = 0.75 - \eta_f \leq 0 \tag{5.21}$$

$$g_3(x) = 2 - N \leq 0 \tag{5.22}$$

$$g_4(x) = \omega - x_4 \leq 0 \tag{5.23}$$

$$g_5(x) = x_4 - B_d \leq 0 \tag{5.24}$$

$$g_6(x) = \ell - x_5 \leq 0 \tag{5.25}$$

$$g_7(x) = x_5 - L_d \leq 0 \tag{5.26}$$

$$g_8(x) = x_6 - H_d \leq 0 \tag{5.27}$$

5.4 Available Design Information

A heat sink will be designed with bypass for minimum entropy generation when a heat source of specified dimensions and heat load, properties of heat sink material, properties of cooling fluid, ambient temperature, bypass dimensions (parameters) and design constraints L_d, B_d, H_d, t_{b_d} and $\forall_{Fan}$ are known.

5.4.1 Bypass Configuration

Figure 5.1 is a representation of bypass in an electronic enclosure.

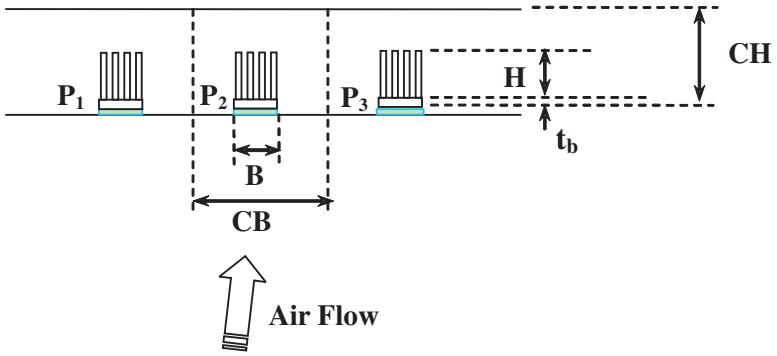

Figure 5.1: Bypass in an Electronic Enclosure

Bypass is defined by the following expressions:

$$\begin{aligned} \text{Top Bypass: } CH_T &= CH - (H + t_b) \\ \text{Side Bypass: } CH_S &= CB - B \end{aligned}$$

The information regarding the duct (CH and CB) must be provided earlier before designing a heat sink as they are considered as parameters.

System information is provided in Table 5.5.

Table 5.5: Available System Information

Item	Specifications			
Duct Configuration	CB	=	150	mm
	CH	=	150	mm
Heat Source	ℓ	=	25	mm
	ω	=	25	mm
	Q	=	25	W
Cooling Fluid - Air	ρ	=	1.2	kg/m^3
	μ	=	1.8×10^{-5}	$N \cdot s/m^2$
	C_p	=	1007	J/kg.K
	k_f	=	25.74×10^{-3}	$W/m \cdot K$
	Pr	=	0.7	-
Heat Sink Material - Al	k	=	209	$W/m \cdot K$
Ambient Temperature	T_a	=	293	K
Fan Capacity	$\forall_{Fan}$	=	30	CFM
Design Constraints	L_d	=	100	mm
	B_d	=	100	mm
	H_d	=	50	mm
	t_{b_d}	=	10	mm

5.5 Optimization Techniques

Optimization can be done using the following two techniques:

1. Parametric Optimization

2. Multi-variable Optimization

5.5.1 Parametric Optimization

The rate of entropy generation given in Eq. 5.1 can be used to optimize for any or all variables. The simplest approach is obtained by fixing all variables in the heat sink design but one and then monitoring the change in entropy generation as that particular design variable is freed to float over a typical range. A distinct minimum will be established that represents the magnitude of the free variable that leads to the lowest rate of entropy generation. This technique of optimization is known as parametric optimization.

Parametric optimization needs initial guess of all variables except one to start the parametric optimization for that particular variable. The values of variables are assumed as follows:

$$L = 50.0\ (mm);\ H = 25.0\ (mm);\ B = 50.0\ (mm); t = 1.0\ (mm);$$
$$s = 2.5\ (mm);\ N = 15;\ t_b = 7.3\ (mm);\ V_d = 2\ (m/s)$$

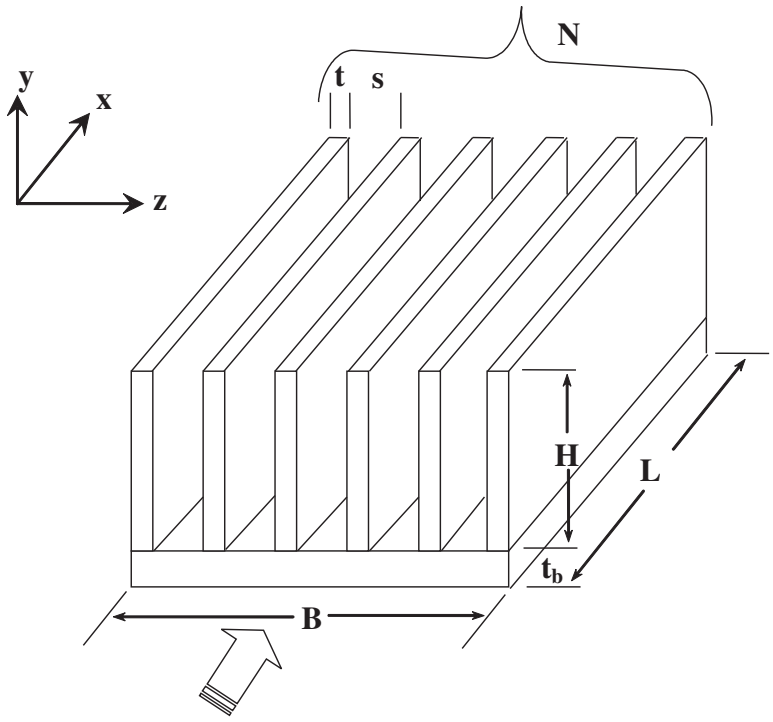

Figure 5.2: Dimensions of a Heat Sink

5.5.2 Optimized Data after Parametric Optimization

Tables 5.6 and 5.7 show the optimized data for minimum entropy generation after parametric optimization. A heat sink designed with all parametric optimized data shows lower entropy generation than the entropy generation associated with each single variable [Table 5.6 and Fig. 5.3].

Table 5.6: Single Variable Optimized Dimensions of a Heat Sink

Variable	Optimized Data	
	Variables	$\mathcal{S}_{gen} \times 10^3\ W/K$
L	100.0 mm	8.21
H	50 mm	6.17
B	100.0 mm	5.05
t	0.505 mm	9.16
s	2.64 mm	9.58
$N = 33$		
t_b	10 mm	9.55
V_d	3.28 m/s	8.1
All	$\mathcal{S}_{gen} = 4.64 \times 10^{-3}\ W/K$	

Table 5.7: Performance of an Optimized Heat Sink

θ_b	7.34	K
R_{th}	0.294	K/W
η_f	78.44	%
η_0	78.98	%
P_{hs}	9.94	Pa
Q_d	156	CFM
Power	0.73	W

After Parametric Optimization, the temperature excess (θ_b) of the optimized heat sink is found to be 7.34 K [Table 5.7].

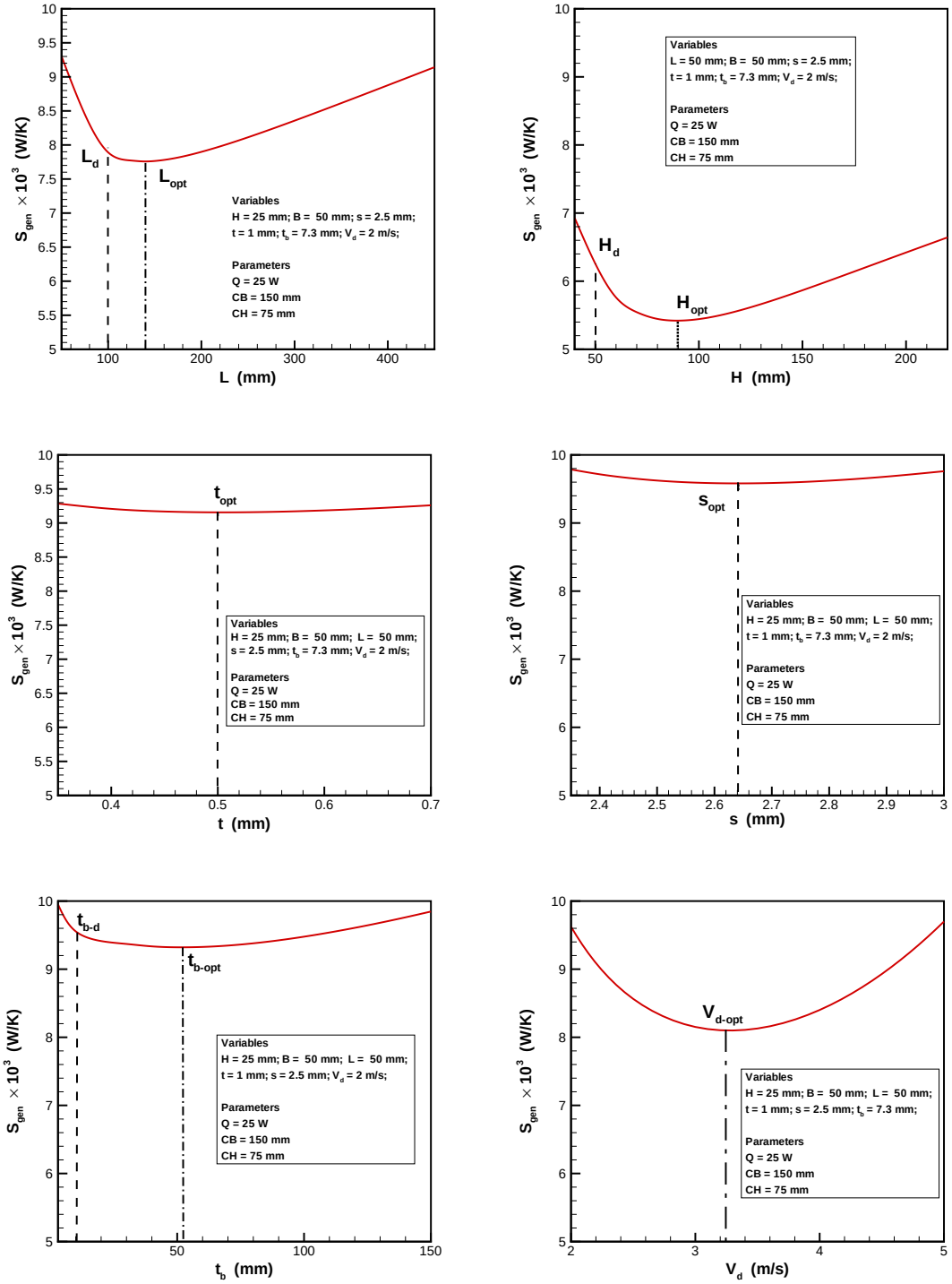

Figure 5.3: Influence of individual variable on $\mathcal{S}_{gen}$

5.6 Multi-variable Optimization

While single variable parametric optimization can provide an optimum design condition when all other design variables are predetermined, there is no guarantee that this "Optimized" data will hold when other design variables are unconstrained. Optimization must be achieved based on a simultaneous solution considering all decision variables with equality and inequality constraints. This can be accomplished by incorporating a multi-variable Kuhn-Tucker Method where the minimizing Eq. 5.72 is invoked for each variable, leading to a series of nonlinear equations that must be solved in a simultaneous manner.

When the variables are freed to float, some variables such as L, B, H and t_b show the tendency to become as large as possible to attain higher heat sink performance for minimum entropy generation rate, which is not practical because of the restriction of space (L_d, B_d, H_d, CH, CB) and cost or weight (t_{b_d}) of the heat sink. Heat Sink designers should be aware of these restrictions prior to initiating the design process. During the optimization process, optimum values for L, B, H and t_b are found similar to L_d, B_d, H_d and t_{b_d}.

Tables 5.8 and 5.9 show the dimensions and performance of a multi-variable optimized heat sink and compare these data with that of a parametric and thermally optimized heat sink. Optimized values are different for each case. The dimensions of a thermally optimized heat sink are changed with the change of flow rate, and if there is no air cooling limit, the higher the flow rate the better the thermal performance is. But there is a trade off, this higher performance is achieved with the expense of higher fan power. But in the case of entropy generation minimization, which deals with the minimization of both thermal and hydraulic resistance, it is found that optimized heat sinks exhibit a slightly poorer thermal performance but a very good hydraulic performance. It needs very small amount of fan power compared to the heat sinks obtained from parametric and thermal optimization.

After multi-variable optimization, the temperature excess (θ_b) of the optimized heat sink is found to be 9.12 K, which is higher than that of single variable (θ_b=7.34) and thermally (only) (θ_b=5.53) optimized heat sink [Table 5.9].

Table 5.8: Dimensions of an Optimized Heat Sink

Variables	Multi-variable	Single Variable	Thermally (only)	Unit
L	100.0	100.0	100.0	mm
H	50.0	50.0	50.0	mm
B	100.0	100.0	100.0	mm
t	0.95	0.505	0.90	mm
s	3.05	2.64	1.67	mm
N	26	33	40	-
t_b	10	10	10	mm
V_d	1.77	3.28	5	m/s

Table 5.9: Performance of an Optimized Heat Sink

Parameters	Multi-variable	Single Variable	Thermally (only)	Unit
$\mathcal{S}_{gen}$	0.0031	0.00464	0.0135	W/K
T_b	302.12	300.34	298.53	K
θ_b	9.12	7.34	5.53	K
R_{th}	0.365	0.294	0.221	K/W
η_f	88.46	78.44	83.8	$\%$
η_0	88.8	78.98	84.1	$\%$
P_{hs}	3.57	9.94	31.1	Pa
Q_d	84	156	238	CFM
Power	.142	0.73	3.5	W

5.7 Sensitivity Analysis

In all optimization models the coefficient of the objective function and the constraints are supplied as input data or as parameters to the model. The optimal solution obtained is based on the values of these parameters. In practice the values of these parameters are seldom known with absolute certainty, because many of them are application oriented. Hence the solution of a practical problem is not complete with the mere determination of the optimal solution.

Each variation in the values of the parameters changes the optimization result, which may in turn effect the optimal solution found earlier. In order to develop an overall strategy to meet the various contingencies, one has to study how the optimal solution will change with changes in the input parameters. This is know as sensitivity analysis.

There are a number of reasons for performing a detailed sensitivity analysis:

1. To find one or more parameters with respect to which the optimal solution is very sensitive. If such parameters exist, then it may be worthwhile to change the corresponding system features.

2. To extract information about additions or modifications to the system so as to improve the overall operation.

3. To clarify the effect on the system of variations in imprecisely known parameters. Some model parameters may be subject to considerable uncertainty. A sensitivity analysis can indicate whether it is worthwhile to expend resources to obtain a better estimate of these parameter values.

4. To suggest the likely effects of variations in uncontrollable external parameters.

Because this type of information is so important in implementing a solution on the real system, a detailed sensitivity analysis is, in many cases, more valuable than the actual optimal solution itself.

Sensitivity information is normally extracted in two ways: through the Kuhn-Tucker multipliers values and through parameter case study runs. The Kuhn-Tucker multipliers of Eq. 5.72 are

measures of the rate of change of the objective function with respect to a change in the right-hand side of the constraint.

Thus, given a equality constraint $h_k(x) = b_k$, the multiplier v_k is equal to

$$v_k = \frac{\partial f}{\partial b_k} \tag{5.28}$$

Similarly, for an inequality constraint $g_j(x) \geq d_j$, the multiplier u_j is equal to

$$u_j = \frac{\partial f}{\partial d_j} \tag{5.29}$$

As a first-order approximation, the change of the objective function value resulting from changes in the right-hand side of constraints is given by:

$$\begin{aligned} f(x) - f(x^*) &= \sum_k \left(\frac{\partial f}{\partial b_k} \right) \Delta b_k + \sum_j \left(\frac{\partial f}{\partial d_j} \right) \Delta d_j \\ &= \sum_k v_k \Delta b_k + \sum_j u_j \Delta d_j \end{aligned} \tag{5.30}$$

This estimate of the change in the optimal objective function value is likely to be quite good provided that the changes Δd_j, Δb_k are small, that the same constraints remain tight at the optimum, and that only a few constraints are perturbed at a time.

5.7.1 Sensitivity Analysis by Parameter Case Study

In our problem, bypass (duct geometry), heat sink material, cooling fluid, heat load and package dimensions are considered as parameters. Sensitivity of these parameters on the optimized value will be discussed in the following.

Sensitivity of Bypass

Tables 5.10 and 5.11 and Figs. 5.4 and 5.5 show the influence of bypass on the dimensions of a heat sink for optimum performance. It is clear that dimensions rearrange themselves depending on bypass for better heat sink performance. The higher the bypass the lower the heat sink performance is. With the increasing bypass, the spacing is readjusted to a larger value to ensure better fluid flow by reducing the hydraulic resistance associated with the frictional drag. Larger spacing results in a decrease in number of fins for a heat sink of same width which result in higher thermal resistance and lower pressure drop. The entropy associated with the thermal resistance dominates over the entropy associated with the pressure drop and results in an increase in overall entropy generation.

Table 5.10: Influence of Bypass on Optimized Heat Sink Dimensions

Bypass		L	H	B	t	s	N	t_b	V_d
$CB\ (mm)$	$CH\ (mm)$	mm	mm	mm	mm	mm	-	mm	m/s
150	150	100	50	100	0.945	3.05	25	10	1.77
200	200	100	50	100	0.96	3.44	24	10	1.75
250	250	100	50	100	0.97	3.77	22	10	1.72
300	300	100	50	100	0.98	4.10	20	10	1.70

Table 5.11: Influence of Bypass on Optimized Heat Sink Performances

Bypass in mm		$\mathcal{S}_{gen} \times 10^3$	T_b	θ_b	R_{th}	η_f	η_0	Q_d	P_{hs}	$Power$
CB	CH	W/K	K	K	K/W	%	%	CFM	Pa	W
150	150	3.14	302.1	9.1	0.37	88.5	88.8	84	3.6	0.14
200	200	3.55	303.2	10.2	0.41	89.4	89.7	148	2.4	0.17
250	250	3.91	304.2	11.2	0.45	90.0	90.3	228	1.8	0.19
300	300	4.23	305.1	12.1	0.48	90.4	90.7	324	1.4	0.21

From Table 5.11, it is found that the heat sink with less bypass results in a lower temperature excess (θ_b) and flow rate (CFM) than a heat sink with higher bypass [Table 5.11].

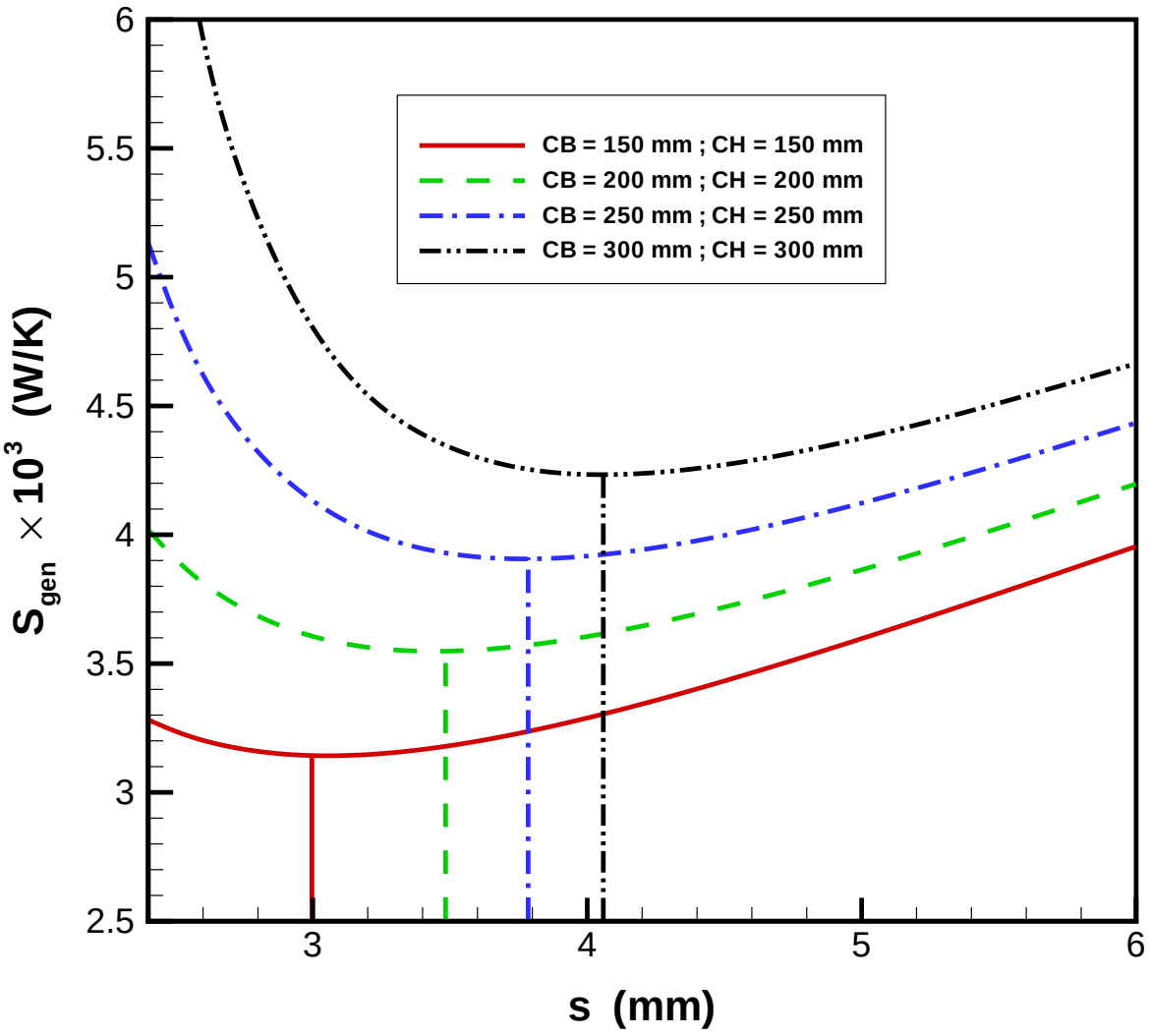

Figure 5.4: Sensitivity of Bypass on Optimized Value of $\mathcal{S}_{gen}$ and s

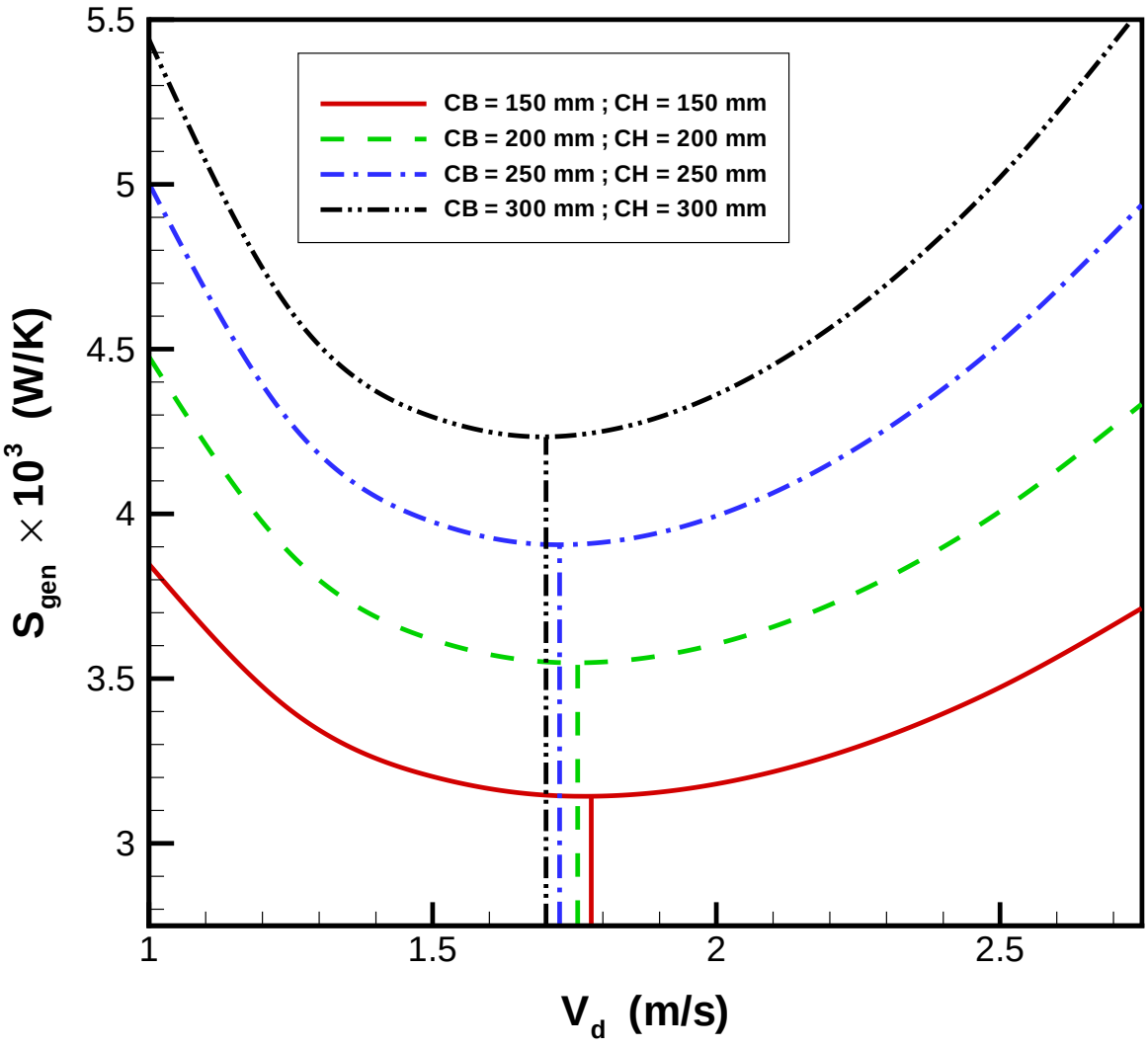

Figure 5.5: Sensitivity of Bypass on Optimized Value of $\mathcal{S}_{gen}$ and V_d

Sensitivity of Heat Sink Material

Aluminium (k_{Al} = 209 W/m·K), Copper (k_{Cu} = 388 W/m·K), Magnesium (k_{Mg} = 156 W/m·K), and Stainless Steel (k_{SS} = 13.4 W/m·K) are used to check the sensitivity of heat sink material on the optimized data. Table 5.12 and 5.13 show that the higher the conductivity of the material the better the performance is with a decrease in fin thickness, t. Figure 5.6 shows the influence of fin thickness on entropy generation for heat sinks of different material. Because of the cost and machining difficulty, heat sinks with aluminium fins and a copper base can be the best choice for optimum thermal performance of a heat sink. From Table 5.13, it is found that use of copper in the base plate can lower the spreading and material resistance almost by 50% while all other resistances remain constant.

Table 5.12: Influence of Material on Optimized Heat Sink Dimensions

Material		L	H	B	t	s	N	t_b	V_d
Fin	Base	mm	mm	mm	mm	mm	-	mm	m/s
Al	Al	100.0	50.0	100.0	0.945	3.05	26	10	1.77
Al	Cu	100.0	50.0	100.0	0.945	3.05	26	10	1.77
Cu	Cu	100.0	50.0	100.0	0.70	3.07	27	10	1.76
Mg	Mg	100.0	50.0	100.0	1.09	3.04	25	10	1.77
SS	SS	85.0	37.0	100.0	2.54	2.68	20	10	2.19

Table 5.13: Influence of Material on Heat Sink Resistances

Material		R_s	R_m	R_{hs}	R_{th}
Fin	Base	K/W	K/W	K/W	K/W
Al	Al	8.35×10^{-2}	4.78×10^{-2}	2.75×10^{-1}	3.64×10^{-1}
Al	Cu	4.50×10^{-2}	2.58×10^{-2}	2.75×10^{-1}	3.23×10^{-1}
Cu	Cu	4.50×10^{-2}	2.58×10^{-2}	2.48×10^{-1}	2.95×10^{-1}
Mg	Mg	1.12×10^{-1}	6.41×10^{-2}	2.93×10^{-1}	4.11×10^{-1}
SS	SS	1.19×10^{0}	2.01×10^{0}	7.39×10^{-1}	2.02×10^{0}

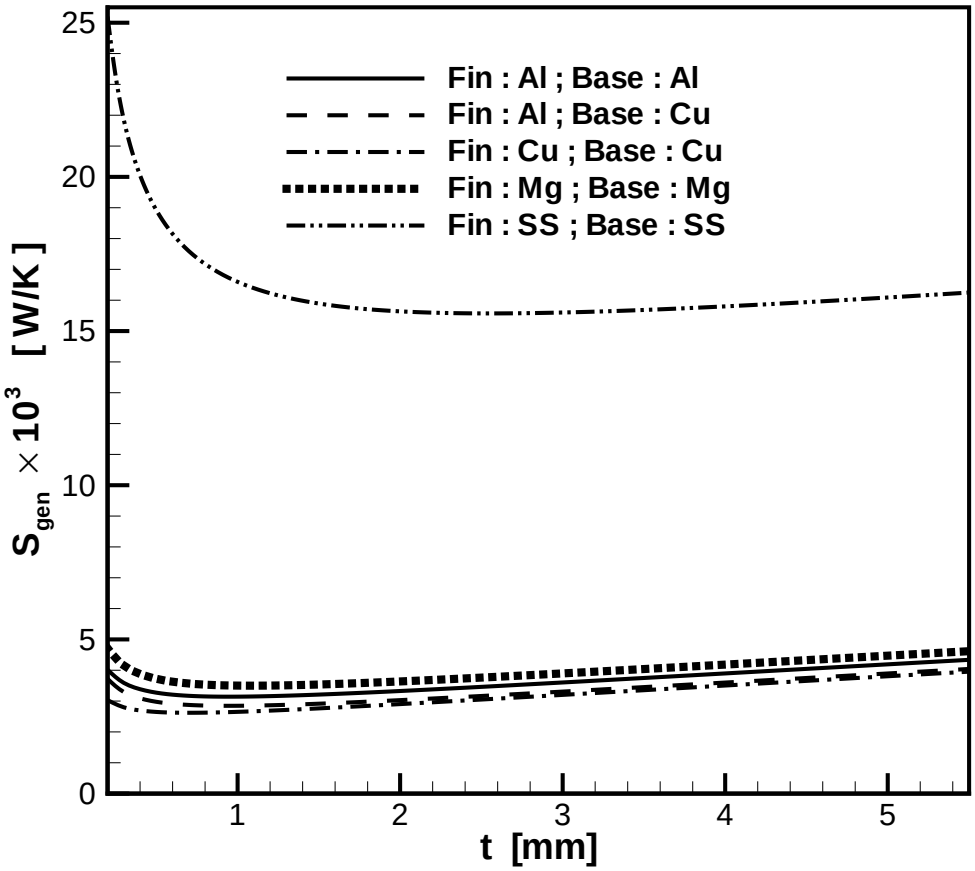

Figure 5.6: Sensitivity of Material on Optimized Value of $\mathcal{S}_{gen}$ and t

Table 5.14: Influence of Material on Optimized Heat Sink Performances

Material		$\mathcal{S}_{gen} \times 10^3$	T_b	θ_b	R_{th}	η_f	η_0	Q_d	P_{hs}	*Power*
Fin	Base	W/K	K	K	K/W	%	%	CFM	Pa	W
Al	Al	3.14	302.09	9.09	0.364	88.58	88.90	84.4	3.63	0.145
Al	Cu	2.85	301.08	8.08	0.323	88.58	89.90	84.4	3.63	0.144
Cu	Cu	2.62	300.38	7.38	0.295	91.52	91.52	83.9	3.48	0.138
Mg	Mg	3.50	303.29	10.29	0.411	87.22	87.57	84.38	3.71	0.148
SS	SS	15.57	343.44	50.44	2.02	72.33	73.22	104.41	5.23	0.258

Sensitivity of Heat Input

Tables 5.15 and 5.16, and Fig. 5.7 show that the optimized data change significantly with a change in heat load. Higher heat loads require more surface area and air flow to remove the excess heat that results in a decrease in fin spacing and heat sink resistance at the expense of heat sink efficiency. A decrease in fin spacing and an increase in flow rate results in an increase in hydraulic resistance associated with fluid drag which in turn results in an increase in entropy generation. Though heat sink resistance is less in high heat load cases because of higher fluid flow, still it shows higher temperature access because of comparatively higher material and spreading resistance.

Table 5.15: Influence of Heat Load on Optimized Heat Sink Dimensions

Q	L	H	B	t	s	N	t_b	V_d
W	mm	mm	mm	mm	mm	-	mm	m/s
25	100.0	50.0	100.0	0.945	3.05	26	10	1.77
50	100.0	50.0	100.0	0.933	2.55	29	10	2.54
100	100.0	50.0	100.0	0.921	2.13	33	10	3.67
200	100.0	50.0	100.0	0.91	1.78	38	10	5.29

Table 5.16: Influence of Heat Load on Optimized Heat Sink Performances

Q	$\mathcal{S}_{gen} \times 10^3$	T_b	θ_b	R_{th}	η_f	η_0	Q_d	P_{hs}	$Power$
W	W/K	K	K	K/W	%	%	CFM	Pa	W
25	3.14	302.09	9.09	0.363	88.58	88.90	84.4	3.63	0.145
50	10.21	308.03	15.03	0.3	86.86	87.17	121	7.46	0.616
100	33.83	318.29	25.29	0.253	84.93	85.23	175	15.5	1.84
200	114.41	336.53	33.53	0.218	82.89	83.18	252	32.02	3.81

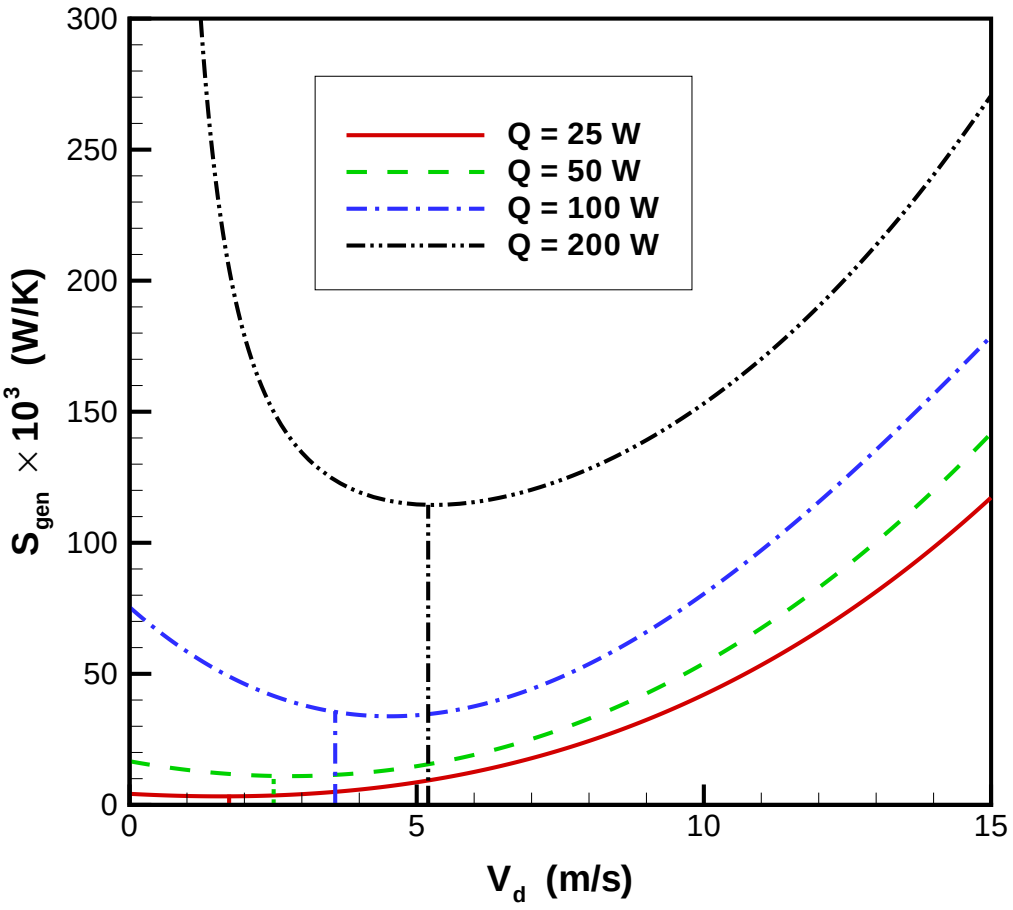

Figure 5.7: Sensitivity of Heat Load on Optimized Value of $\mathcal{S}_{gen}$ and V_d

Sensitivity of Coverage Ratio

Tables 5.17 and 5.18, and Fig. 5.8 show that the optimized data change significantly with a change in heat source dimensions. Smaller heat source dimension results in lower coverage ratio that results in an increase in spreading resistance which in turn results in higher entropy generation. Coverage ratio has very little affect on the optimized variable such as fluid flow and heat sink dimensions. Only the base plate thickness is adversely affected. From Fig. 5.8, it is observed that the higher the coverage ratio the lower the entropy generation is and it is better to keep the coverage ratio greater than 5% to have minimum entropy generation.

Table 5.17: Influence of Coverage Ratio on Optimized Heat Sink Dimensions

χ	L	H	B	t	s	N	t_b	V_d
%	mm	mm	mm	mm	mm	-	mm	m/s
0.01	100.0	50.0	100.0	0.945	3.07	26	5.11	1.79
0.25	100.0	50.0	100.0	0.945	3.05	26	10	1.77
1.00	100.0	50.0	100.0	0.945	3.05	26	10	1.77
6.25	100.0	50.0	100.0	0.945	3.05	26	10	1.77
25.00	100.0	50.0	100.0	0.945	3.05	26	10	1.77
81.00	100.0	50.0	100.0	0.945	3.05	26	10	1.77

Table 5.18: Influence of Coverage Ratio on Optimized Heat Sink Performances

χ	$\mathcal{S}_{gen} \times 10^3$	T_b	θ_b	R_{th}	η_f	η_0	Q_d	P_{hs}	$Power$
%	W/K	K	K	K/W	%	%	CFM	Pa	W
0.01	19.7	358.9	65.9	2.64	88.59	88.91	85.56	3.58	0.145
0.25	5.8	311.2	18.2	0.73	88.59	88.91	84.29	3.63	0.145
1.00	4.2	305.6	12.6	0.50	88.59	88.91	84.29	3.63	0.145
6.25	3.1	302.1	9.1	0.36	88.59	88.91	84.29	3.63	0.145
25.00	2.7	300.7	7.7	0.31	88.59	88.91	84.29	3.63	0.145
81.00	2.5	300.0	7.0	0.28	88.59	88.91	84.86	3.60	0.145

The sensitivity of cooling fluid will not be discussed as the air is universally used as a cooling fluid in microelectronics cooling, and the goal of this research is to find the air cooling limit for minimum entropy generation.

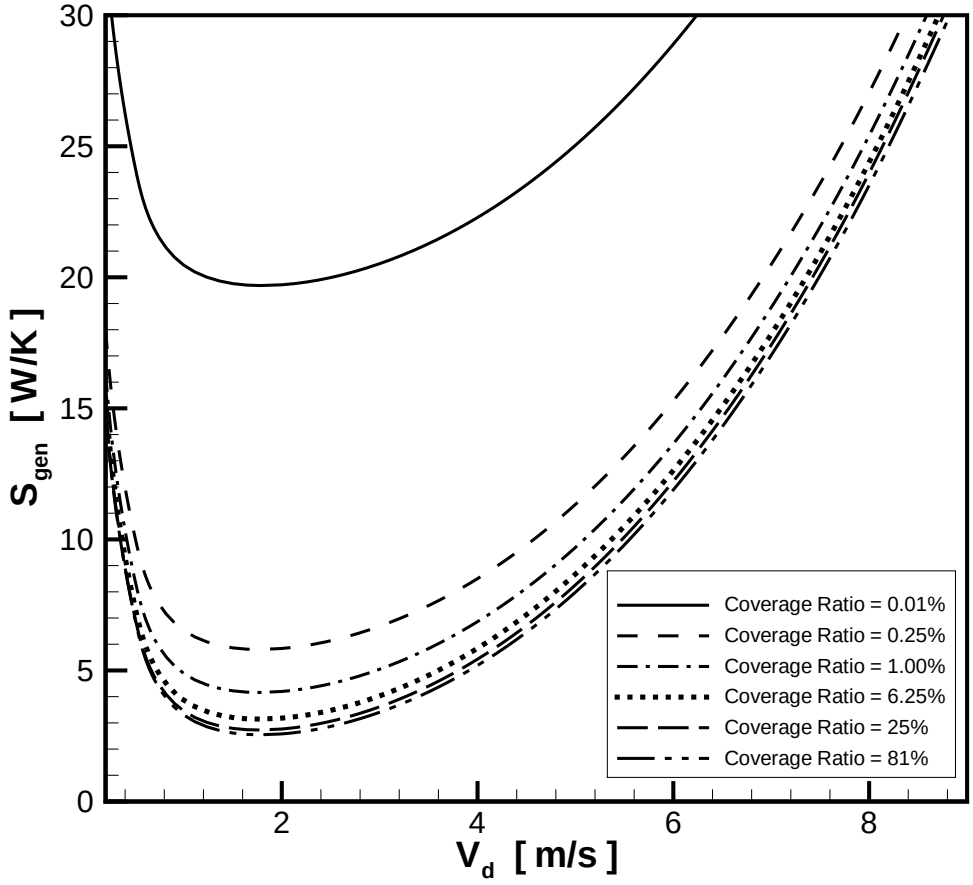

Figure 5.8: Sensitivity of Coverage Ratio on Optimized Value of $\mathcal{S}_{gen}$ and V_d

5.8 Summary

A procedure is presented that allows design variables in plate fin heat sinks to be optimized for minimum entropy generation. The procedure is based on the minimization of entropy generation resulting from viscous fluid effects and heat transfer, both in the cooling medium and within the internal conductive path of the heat sink. The model clearly demonstrates a rapid, stable procedure for obtaining optimum design conditions without resorting to parametric analysis using repeated iterations with a thermal analysis tool.

The optimization model allows design variables to be constrained at a predetermined minimum or maximum according to the design requirement but otherwise free to float to an optimized value.

Sensitivity analysis is also carried out with a heat sink of variable bypass, and it is found that with the change of bypass, the optimized dimensions and performance of a heat sink are also changed for minimum entropy generation.

Chapter 6

Conclusion

The primary focus of this research initiative was to develop a compact heat sink model that incorporates the effects of flow bypass into the design process. Most existing design tools for optimizing plate fin heat sinks assume fully shrouded flow thereby forcing air through the heat sink producing a follow pattern that is not typically encountered in real applications. A more practical design tool that includes both top and side bypass allows for more realistic design conditions and in turn produces an optimized solution that will better protect sensitive electronic components.

The influence of bypass was studied first through an experimental program in order to get the insight of thermal and hydraulic characteristics of a heat sink for different flow conditions. It was observed that bypass influenced pressure drop and thermal resistance differently depending on heat sink geometries and flow conditions. This experimental observation was later used to develop a compact model to determine the performance of a plate fin heat sink. Experimental data were also used to validate the newly developed compact model. The absence of a compact model constrained researchers from designing an optimized heat sink for best thermal and hydraulic performance. This newly developed model makes it possible to develop a simulation model for predicting optimum heat sink dimensions and performance. The optimization program is developed based on a procedure that allows the simultaneous optimization of heat sink design parameters based on a minimization of the entropy generation associated with heat transfer and fluid friction. This model considers the effect of flow bypass on optimum flow and heat transfer condition.

This thesis presents the development of an analytical model for fluid flow by applying a control volume analysis for momentum balance between heat sink and bypass area in order to accurately

predict the air flow through the heat sink. The control volume analysis incorporates the flow and frictional drag associated with the heat sink and bypass area for laminar developing flow. The model was validated with experimental data for pressure drop and found to have an RMS error of $\pm 10\%$. The model was later validated with the experimental data of Butterbugh and Kang [1995] and Jonsson and Moshfegh [2001] using their heat sink and duct geometry, and the RMS difference was found within $\pm 9\%$ and $\pm 11\%$ respectively. Their experimental procedures were similar to this research study. The model was also validated with the numerical work of Coetzer and Visser [2003] and found to have an RMS difference of $\pm 5.6\%$. A correlation for channel velocity was built with respect to duct velocity (V_d), channel spacing (s), channel thickness (t), duct Reynolds number (Re_d) and duct geometry (CH and CB), and the RMS difference was found $\pm 8\%$ with respect to the model data. The simplified correlation is later used in the optimization model for minimum entropy generation.

The second part of this research details a thermal model for predicting the base plate temperature (T_b) of a heat sink, which is one of the main focuses of this research. The thermal model includes an existing convective/conductive fin resistance model, spreading resistance model and a material resistance model. Thermally developing laminar flow is assumed to determine the convective heat transfer coefficient (h) of fin resistance model and the spreading resistance model using the channel velocity found in the earlier fluid model. The model was validated with experimental data for thermal resistance with an RMS difference of $\pm 10\%$. The model was later validated with experimental data of Butterbugh and Kang [1995] and Jonsson and Moshfegh [2001] using their heat sink and duct geometry and found to have an RMS difference of $\pm 5\%$ and $\pm 11\%$, respectively. Their experimental procedures were similar to this research study.

The final part of this research deals the performance of a heat sink in terms of total thermal and hydraulic resistance. From the development of the fluid and thermal model, it was observed that there exists an inverse relationship between the thermal resistance and pressure drop that allows an optimized condition for which entropy generation associated with thermal and hydraulic resistance can be minimized. At first, the effect of each variable such as heat sink length (L), height (H), width (B), fin spacing (s), fin thickness (t), number of fins (N), base plate thickness (t_b), coverage ratio (χ) and duct velocity (V_d) on entropy generation was examined one by one in a single variable optimization and later those optimized values were combined together to get the

final optimized data. In single variable optimization, there is no guarantee that this "optimized" data will hold when other design variables are unconstrained. Optimization must be achieved based on a simultaneous solution considering all decision variables with equality and inequality constraints. A multi-variable optimization with all variables (L, H, B, s, t, N, t_b and V_d) free to float was performed and data for optimized heat sink dimensions and performance were obtained. The thermally optimized heat sink showed better thermal performance than the optimized heat sink obtained from entropy generation minimization but with higher entropy generation rate and pressure drop penalty. A sensitivity analysis for various bypass was carried out in the optimization program, and it was found that with the change of bypass, the optimized dimensions and performances of a heat sink were also changed. Minimum entropy generation is increased with an increase of bypass with new optimized dimensions and performance of a heat sink.

References

[1] Airflow Measurement Systems, "Airflow Systems," *http://www.fantester.com*

[2] Antonetti, V.W., "On the Use of Metallic Coatings to Enhance Thermal Contact Conductance," Ph.D. Dissertation, Department of Mechanical Engineering, University of Waterloo, Waterloo, ON, Canada, 1983.

[3] Ashiwake, N., Nakayama, W., Daikoku, T., and Kobayashi, F., "Forced Convection Heat Transfer from LSI Packages in an Air Cooled Wiring Card Array," *Heat Transfer in Electronic Equipment-193,* ASME HTD 28, 1983, pp. 35-42.

[4] Azar, K., McLeod, R.S., and Caron, R.E., "Narrow Channel Heat Sink for Cooling of High Powered Electronics Components," *Proceedings of the Eighth Annual IEEE Semiconductor Thermal Measurement and Management Symposium (SEMI-THERM VIII),* Austin, TX, 1992, pp. 12-19.

[5] Azar, K., "The History of Power Dissipation," *http://www.electronicssooling.com /html /2000_jan_a2.html,* Southborough, MA: Electronics Cooling, 2000.

[6] Azar, K., "Managing Power Requirements in the Electronics Industry," *http: //www.electronics-cooling.com/html/2000_dec_a1.html,* Southborough,MA: Electronics Cooling, 2000.

[7] Bar-Cohen, A., and Iyengar, M., "Least-Energy Optimization of Air-cooled Heat Sinks for Sustainable Development," *Proceedings of the Sixth Intersociety Conference on Thermal and Thermomechanical Phenomena in Electronic Systems (ITHERM'98),* Seattle, WA, 1998, pp. 295-302.

[8] Bejan, A., *Entropy Generation Through Heat and Fluid Flow,* New York: Wiley, 1982.

[9] Bejan, A., and Morega, A.M., "Optimal Arrays of Pin Fins and Plate Fins in Laminar Forced Convection," *Journal of Heat Transfer,* Vol. 115, 1993, pp. 75-81.

[10] Bejan, A., Tsataronis, G., and Moran, K., *Thermal Design and Optimization,* New York: Wiley, 1996.

[11] Bejan, A., *Entropy Generation Minimization,* Boca Raton, FL: CRC Press, 1996.

[12] Bejan, A., *Advanced Engineering Thermodynamics,* New York: Wiley, 1997.

[13] Butterbaugh, M.A., and Kang, S.S., "Effect of Airflow Bypass on the Performance of Heat Sinks in Electronic Cooling," *ASME Advances in Electronic Packaging,* Vol. EEP-10-2, 1995, pp. 843-848.

[14] Churchil, S.W. and Usagi, R., "A General Expression for the Correlation of Rates of Transfer and Other Phenomena," *AIChE Journal,* Vol. 18, No. 6, 1972, pp. 1121 - 1128.

[15] Coetzer, C.B., and Visser, J.A., "Compact Modeling of Forced Flow in Longitudinal Fin Heat Sinks with Tip Bypass," *ASME Journal of Electronic Packaging,* Vol. 125, 2003, pp. 319-324.

[16] Copeland, D., "Optimization of Parallel Plate Heat Sinks for Forced Convection", *Proceedings of the Sixteenth Annual IEEE Symposium on Semiconductor Thermal Measurement and Management (SEMI-THERM XVI),* San Jose, CA, 2000, pp. 266-272.

[17] Culham, J.R., and Muzychka, Y.M., "Optimization of Plate Fin Heat Sinks Using Entropy Generation Minimization," *IEEE Transactions on Components and Packaging Technologies,* Vol. 24, No. 2, 2001, pp. 16-25.

[18] Flow Kinetics LLC., "Using a Pitot Static Tube for Velocity and Flow Rate Measurement," *http://www.flowmeterdirectory.com/flowmeter_artc/flowmeter_artc_02111201 .html*

[19] Goldberg, N., "Narrow Channel Forced Air Heat Sink," *IEEE Transactions on Components, Hybrids, and Manufacturing Technology,* Vol. CHMT-7, No. 1, 1984, pp. 154-159.

[20] Hirata, M., Kakita, Y., Yada, Y., Hirose, Y., Morikawa, T., and Enomot, H., "Temperature Distribution of Finned Integrated Circuits," *FUJITSU Scientific & Technical Journal*, December 1970.

[21] Holahan, M.F., Kang, S.S., and Bar-Cohen, A., "A Flow Stream Based Analytical Model for Design of Parallel Plate Heat Sinks," *ASME Proceedings of the* 31^{st} *National Heat Transfer Conference (HTD-Vol. 329),* Houston, TX, Vol. 7, 1996, pp. 63-71.

[22] Incropera, P.F., and Dewitt, D.P., *Fundamentals of Heat and Mass Transfer*, New York: Wiley, 2002.

[23] Intel Corporation, "Moore's Law," *http://www.intel.com/research/silicon/ mooreslaw.htm*, Santa Clara, CA.

[24] Iwasaki, H., Sasaki, T., and Ishizuka, M., "Cooling Performance of Plate Fins for Multichip Modules," *IEEE Transactions on Components, Packaging and Manufacturing Technology - Part A,* Vol. 18, No. 3, 1995, pp. 592-595.

[25] Iyengar, M., and Bar-Cohen, A., "Design for Manufacturability of SISE Parallel Plate Forced Convection Heat Sinks," *IEEE Transactions on Components and Packaging Technologies,* Vol. 24, No. 2, 2001, pp. 150-158.

[26] Jonsson, H., and Moshfegh, B., "Modeling of the Thermal and Hydraulic Performance of Plate Fin, Strip Fin, and Pin Fin Heat Sinks- Influence of Flow Bypass," *IEEE Transactions on Components and Packaging Technologies,* Vol. 24, No. 2, 2001, pp. 142-149.

[27] Kays, W.M., and London, A.L., *Compact Heat Exchangers,* New York: McGraw-Hill, 1984.

[28] Khan, W.A., Culham, J.R., and Yovanovich, M.M., "Performance of Shrouded Pin-Fin Heat Sinks in Forced Convection Cooling," *Proceedings of the 38th AIAA Themophysics Conference,* Toronto, Canada, 2005.

[29] Kim, D., and Kim, J.S., "Compact Modeling of Fluid Flow and Heat Transfer in Straight Fin Heat Sinks," *ASME Journal of Electronic Packaging,* Vol. 126, 2004, pp. 247-255.

[30] Knight, R.W., Goodling, J.S., and Gross, B.E., "Optimum Thermal Design of Air Cooled Forced Convection Finned Heat Sinks- Experimental Verification," *IEEE Transactions on Components, Hybrids, and Manufacturing Technology,* Vol. 15, No. 5, 1992, pp. 754-760.

[31] Lau, K.S., and Mahajan, R.L., "Effects of Tip Clearance and Fin Density on the Performance of Heat Sinks for VLSI Packages," *IEEE Transactions on Components, Hybrids, and Manufacturing Technology,* Vol. 12, No. 4, 1989, pp. 757-765.

[32] Lee, R.S., Huang, H.C., and Chen, W.Y., "A Thermal Characteristic Study of Extruded-Type Heat Sinks in Considering Air Flow Bypass Phenomena," *Proceedings of the Sixth Annual IEEE Symposium on Semiconductor Thermal and Temperature Measurement (SEMI-THERM VI),* Phoenix, AZ, 1990, pp. 95-102.

[33] Lee, S., "Optimum Design and Selection of Heat Sinks," *IEEE Transactions on Components, Packaging and Manufacturing Technologies,* Vol. 18, 1995, pp. 812-817.

[34] Lee, S., Song, S., Au, V., and Moran, K. P., "Constriction/Spreading Resistance Model for Electronics Packaging," *ASME/JSME Thermal Engineering Conference,* Vol.4, 1995, pp. 199-206.

[35] Leonard, W., Teertstra, P., and Culham, J.R., "Characterization of Heat Sink Flow Bypass in Plate Fin Heat Sinks," *Proceedings of ASME International Mechanical Engineering Congress & Exposition (IMECE2002-39556),* New Orleans, Louisiana, 2002.

[36] Matsushima, H., Yanagida, T., and Kondo, Y., "Algorithm for Prediction of the Thermal Resistance of Finned LSI Packages Mounted on a Circuit Board," *Heat Transfer - Japanese Research,* Vol. 21, No. 5, 1992, pp. 504-517.

[37] Min, J.Y., Jang, S.P., and Kim, S.J., "Effect of Tip Clearance on the Cooling Performance of a Microchannel Heat Sink," *International Journal of Heat and Mass Transfer,* Vol. 47, 2004, pp. 1099-1103.

[38] Muzychka, Y.S., and Yovanovich, M.M., "Modeling Friction Factors in Non-circular Ducts for Developing Laminar Flow," *Proceedings of the Second AIAA Theoretical Fluid Mech. Meeting,* Albuquerque, NM, 1998.

[39] Narasimhan, S., and Bar-Cohen, A., "Flow and Pressure Field Characteristics in the Porous Block Compact Modelling of Parallel Plate Heat Sinks," *IEEE Transactions on Components, Packaging and Manufacturing Technologies,* Vol. 26, No. 1, 2003, pp. 147-157.

[40] Obinelo, I. F., "Characterization of Thermal Performance of Longitudinal Fin Heat Sinks for System Level Modeling Using CFD Methods," *Proceedings of the ASME International, Intersociety and Photonic Packaging Conference and Exhibition,* Hawaii, 1997.

[41] Omega Engineering, "Highly Accurate, Low-pressure Laboratory Transducer," *http://www.omega.com/Pressure/pdf/PX653.pdf*

[42] Prasher, R.S., "Surface Chemistry and Characteristics Based Model for the Thermal Contact Resistance of Fluidic Interstitial Thermal Interface Materials," *ASME Journal of Heat Transfer,* Vol. 123, 2001, pp. 969-975.

[43] Prstic, S., Iyengar, M., and Bar-Cohen, A., "Bypass Effect in High Performance Heat Sinks, *Proceedings of the International Thermal Science Conference,* Bled, Slovenia, 2000.

[44] Saini, M., and Webb, L.R., "Validation of Models for Air Cooled Plane Fin Heat Sinks Used in Computer Cooling," *Proceedings of the Eighth Intersociety Conference on Thermal and Thermomechanical Phenomena in Electronic Systems (I-THERM),* 2002, pp. 244-250.

[45] Sata, Y., Iwasaki, H., and Ishizuka M., "Development of Prediction Technique for Cooling Performance of Finned Heat Sink in Uniform Flow," *IEEE Transactions on Components, Packaging and Manufacturing Technologies- Part A,* Vol. 20, No. 2, 1997, pp. 160-167.

[46] Sathyamurthy, P., Runstadler, P.W., and Lee, S., "Numerical and Experimental Evaluation of Planar and Staggered Hear Sinks," *Proceedings of the Fifth InterSociety Conference on Thermal Phenomena in Electronic Systems (I-THERM),* 1996, pp. 132-139.

[47] Savija, I., Culham, J.R., Yovanovich, M.M., and Marotta, E.E., "Review of Thermal Conductance Models for Joints Incorporating Enhancement Materials," *40th AIAA Aerospace Sciences Meeting and Exhibit (AIAA-2002-0494),* Reno, NV, 2002.

[48] Savija, I., Culham, J.R., Yovanovich, M.M., and Marotta, E.E., "Thermal Joint Resistance Models for Conforming Rough Surfaces with Grease Filled Gaps," *40th AIAA Aerospace Sciences Meeting and Exhibit (AIAA-2002-0495),* Reno, NV, 2002.

[49] Shah, R.K., and London A.L., *Laminar Flow Forced Convection in Ducts,* New York: Academic Press, 1978.

[50] Shah, R.K., "Chapter 4, Part 3: Compact Heat Exchangers," *Handbook of Heat Transfer Applications,* New York: McGraw-Hill, 1985.

[51] Simons, R.E., and Schmidt, R.R., "A Simple Method to Estimate Heat Sink Air Flow Bypass," *Electronics Cooling,* Vol.3, No. 2, 1997, pp. 36-37.

[52] Sparrow, E.M., Baliga, B.R., and Patankar, S.V., "Forced Convection Heat Transfer from a Shrouded Fin Array with and without Tip Clearances," *ASME Journal of Heat Transfer,* Vol. 100, 1978, pp. 572-579.

[53] Sparrow, E.M., and Beckley, T.J., "Pressure Drop Characteristic for a Shrouded Longitudinal Fin Array with and without Tip Clearances," *ASME Journal of Heat Transfer,* Vol. 103, 1981, pp. 393-395.

[54] Sparrow, E.M., and Hsu, C.F., "Analytically Determined Fin-Tip Heat Transfer Coefficient," *Journal of Heat Transfer,* Vol. 103, No. 1, 1981, pp. 18-25.

[55] Sparrow, E.M., and Kadle, D.S., "Effect of Tip to Shroud Clearance on Turbulent Heat Transfer from a Shrouded Longitudinal Fin Array," *ASME Journal of Heat Transfer,* Vol. 108, 1986, pp. 961-973.

[56] Teertstra, P., Yovanovich, M.M., Culham, J.R., and Lemczyk, T., "Analytical Forced Convection Modelling of Plate Fin Heat Sinks," *Proceedings of the Fifteenth Annual IEEE Symposium on Semiconductor Thermal Measurement and Management,* San Diego, CA, 1999, pp. 34-41.

[57] Yokono, Y., Saski, T., and Ishizuka, M., "Small Cooling Fin Performance for LSI Packages," *Cooling Technology for Electronic Equipment,* New York: Ed. Win Aung, Hemisphere Publishing Corp., 1988, pp. 211-220.

[58] Yovanovich, M.M., "New Contact and Conductance Correlations for Conforming Rough Surfaces," *Spacecraft Radiative Transfer and Temperature Control,* Vol. 83, Progress in Astronautics and Aeronautics, AIAA, New York, 1982, pp. 83-95.

[59] Yovanovich, M.M., Muzychka, Y.S., Culham, J.R., "Spreading Resistance of Isoflux Rectangles and Strips on Compound Flux Channels," *Journal of Thermophysics and Heat Transfer*, Vol. 13, No. 4, 1999, pp. 495-500.

[60] Yuan, T.D., "Computational Modelling of Flow Bypass Effects on Straight Fin Heat Sink in Rectangular Duct," *Proceedings of the Twelfth Annual IEEE Symposium on Semiconductor Thermal Measurement and Management (SEMI-THERM XII),* Austin, TX, 1996, pp. 164-168.

[61] White, M.F., *Fluid Mechanics,* New York: McGraw-Hill, 2003.

[62] Wirtz, R.A., Chen, W., and Zhou, R., "Effect of Flow Bypass on the Performance of Longitudinal Fin Heat Sinks," *ASME Journal of Electronic Packaging,* Vol. 116, 1994, pp. 206-211.

Appendix A

Viscous Dissipation - Rectangular Duct

A.1 Introduction

Viscous dissipation of a rectangular duct will be modelled using the basic equations of motion that will later be equated with the viscous dissipation from a control volume analysis of chapter-4 for a rectangular channel to find the frictional drag in channels for laminar fully developed flow.

A.2 Model Development

For constant thermophysical properties (ρ, μ and k) of a fluid, the basic equations of motions can be reduced to the following:

$$\text{Continuity Equation:} \quad \vec{\nabla}.\vec{V} = 0 \tag{A.1}$$

$$\text{Navier-Stokes Momentum Equation:} \quad \rho\frac{\mathcal{D}\vec{V}}{\mathcal{D}t} = \rho\vec{g} - \vec{\nabla}_p + \mu\nabla^2\vec{V} \tag{A.2}$$

Figure A.1 shows an incompressible viscous flow in a rectangular channel of spacing s, height H and length L. The flow is found only in the direction of x, therefore, $u \neq 0$ but $v = w = 0$. u is $f(z)$ only.

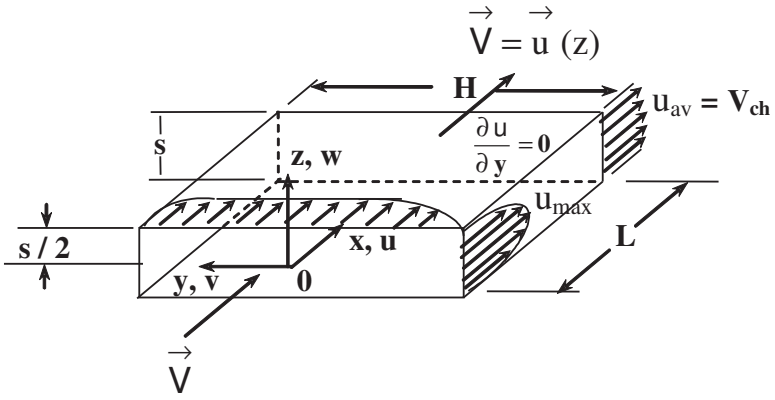

Figure A.1: Velocity Distribution in a Rectangular Duct

Based on these assumptions, Eq. A.1 becomes:

$$\begin{aligned} \frac{\partial u}{\partial x}+\frac{\partial u}{\partial y}+\frac{\partial u}{\partial z} &= 0 \\ \frac{\partial u}{\partial x}+0+0 &= 0 \\ \frac{\partial u}{\partial x} &= 0 \end{aligned}$$

Thus there is a single nonzero axial velocity component that varies across the channel. As $H \gg s$, the flow is assumed two dimensional $\left(\frac{\partial u}{\partial y} \approx 0\right)$. The flow is considered fully developed and the pressure varies in the x direction because of viscous dissipation of flow in the x direction. Gravity effects are assumed negligible.

The x-momentum equation of Eq. A.2 becomes:

$$\begin{aligned} \rho\left(u\frac{\partial u}{\partial x}+v\frac{\partial u}{\partial y}+w\frac{\partial u}{\partial z}\right) &= -\frac{\partial P}{\partial x}+\rho g_x+\mu\left(\frac{\partial^2 u}{\partial x^2}+\frac{\partial^2 u}{\partial y^2}+\frac{\partial^2 u}{\partial z^2}\right) \\ \rho\left(u\times 0+0\times\frac{\partial u}{\partial y}+0\times\frac{\partial u}{\partial z}\right) &= -\frac{\partial P}{\partial x}+\rho\times 0+\mu\left(0+0+\frac{\partial^2 u}{\partial z^2}\right) \\ \mu\frac{\partial^2 u}{\partial z^2} &= \frac{\partial P}{\partial x} \end{aligned} \tag{A.3}$$

The y-momentum equation of Eq. A.2 becomes:

$$\begin{aligned}
\rho\left(u\frac{\partial v}{\partial x}+v\frac{\partial v}{\partial y}+w\frac{\partial v}{\partial z}\right) &= -\frac{\partial P}{\partial x}+\rho g_y+\mu\left(\frac{\partial^2 v}{\partial x^2}+\frac{\partial^2 v}{\partial y^2}+\frac{\partial^2 v}{\partial z^2}\right)\\
\rho\left(u\times 0+0\times 0+0\times 0\right) &= -\frac{\partial P}{\partial y}+\rho\times 0+\mu\left(0+0+0\right)\\
\frac{\partial P}{\partial y} &= 0
\end{aligned}$$

The z-momentum equation of Eq. A.2 becomes:

$$\begin{aligned}
\rho\left(u\frac{\partial w}{\partial x}+v\frac{\partial w}{\partial y}+w\frac{\partial w}{\partial z}\right) &= -\frac{\partial P}{\partial z}+\rho g_z+\mu\left(\frac{\partial^2 w}{\partial x^2}+\frac{\partial^2 w}{\partial y^2}+\frac{\partial^2 w}{\partial z^2}\right)\\
\rho\left(u\times 0+0\times 0+0\times 0\right) &= -\frac{\partial P}{\partial z}+\rho\times 0+\mu\left(0+0+0\right)\\
\frac{\partial P}{\partial z} &= 0
\end{aligned}$$

Thus the pressure gradient in Eq. A.3 is the total and only gradient:

$$\mu\frac{\partial^2 u}{\partial z^2}=\frac{\partial P}{\partial x}=\text{constant} \;<\; 0$$

$\frac{\partial P}{\partial x}$ is made constant because from the theory of separation of variables, it is known that if two quantities are equal and one varies only with z and the other varies only with x, then they must both equal the same constant. Otherwise they would not be independent of each other.

The constant is made negative because physically, the pressure must decrease in the flow direction in order to drive the flow against resisting wall shear stress.

The solution of Eq. A.3 is found by double integration:

$$u=\frac{1}{\mu}\frac{\partial P}{\partial x}\frac{z^2}{2}+C_1 z+C_2 \tag{A.4}$$

C_1 and C_1 can be found by applying boundary conditions.

For no-slip condition, at $z=\pm\frac{s}{2}$, $u=0$.

After substitution of z and u, Eq. A.4 becomes:

$$0 = \frac{1}{\mu}\frac{\partial P}{\partial x}\frac{s^2}{8}+C_1\frac{s}{2}+C_2 \tag{A.5}$$

$$0 = \frac{1}{\mu}\frac{\partial P}{\partial x}\frac{s^2}{8}-C_1\frac{s}{2}+C_2 \tag{A.6}$$

From the solution of A.5 and A.6, constants are found:

$$C_1 = 0 \text{ and } C_2 = -\frac{\partial P}{\partial x}\frac{s^2}{8\mu}$$

The flow in a channel is found by substituting C_1 and C_2 into Eq. A.4:

$$u = -\frac{\partial P}{\partial x}\frac{s^2}{8\mu}\left(1-\frac{4z^2}{s^2}\right) \tag{A.7}$$

at $z = 0$, $u = u_{max}$, Eq. A.7 becomes:

$$u_{max} = -\frac{\partial P}{\partial x}\frac{s^2}{8\mu} \tag{A.8}$$

Substituting u_{max}, Eq. A.7 becomes:

$$u = u_{max}\left(1-\frac{4z^2}{s^2}\right) \tag{A.9}$$

The average channel velocity is defined as:

$$V_{av} = V_{ch} = \frac{\forall_{ch}}{A_{ch}} \tag{A.10}$$

where

$$\begin{aligned} \forall_{ch} &= \frac{\forall_d}{N-1} \qquad \text{where } N \text{ is number of fins} \\ A_{ch} &= s \times H \end{aligned}$$

$\forall_{ch}$ can also be expressed as:

$$\forall_{ch} = \int u \, \mathrm{d}A \tag{A.11}$$

dA can be substituted as H dz

Substituting $\forall_{ch}$ from Eq. A.10 into A.9, V_{ch} can be written as:

$$V_{ch} = \frac{1}{A_{ch}} \int u \, \mathrm{d}A \tag{A.12}$$

Substituting dA, A_{ch}, u and applying limits for z from $-\frac{s}{2}$ to $+\frac{s}{2}$, Eq. A.12 becomes:

$$\begin{aligned}
V_{ch} &= \frac{1}{s \times H} \int_{-\frac{s}{2}}^{+\frac{s}{2}} u_{max} \left(1 - \frac{4z^2}{s^2}\right) H \, \mathrm{d}z \\
V_{ch} &= \frac{u_{max}}{s} \int_{-\frac{s}{2}}^{+\frac{s}{2}} \left(1 - \frac{4z^2}{s^2}\right) H \, \mathrm{d}z \\
V_{ch} &= \frac{u_{max}}{s} \left[z - \frac{4\,z^3}{3\,s^2}\right]_{-\frac{s}{2}}^{+\frac{s}{2}} \\
V_{ch} &= \frac{u_{max}}{s} \left[\left\{+\frac{s}{2} - \left(-\frac{s}{2}\right)\right\} - \frac{4}{3\,s^2}\left\{\frac{s^3}{8} - \left(-\frac{s^3}{8}\right)\right\}\right] \\
V_{ch} &= \frac{u_{max}}{s} \left(s - \frac{s}{3}\right) \\
V_{ch} &= \frac{2}{3}\, u_{max} \\
\text{or} \quad u_{max} &= \frac{3}{2}\, V_{ch}
\end{aligned} \tag{A.13}$$

Substituting u_{max} from A.13 to A.9, the equation of flow becomes:

$$u = \frac{3}{2} V_{ch} \left(1 - \frac{4z^2}{s^2}\right) \tag{A.14}$$

Wall shear stress is defined as:

$$\tau_w = -\mu \frac{\mathrm{d}u}{\mathrm{d}z} \tag{A.15}$$

At $z = \frac{s}{2}$, τ_w is found as:

$$\tau_w = \frac{6\,\mu\, V_{ch}}{s} \tag{A.16}$$

From the definition of hydraulic diameter, $D_{h_{ch}}$ is found:

$$D_{h_{ch}} = \frac{4\,A_{ch}}{\mathcal{P}_{ch}} = \frac{4\,s\,H}{2\,(s+H)} = \frac{2\,s}{1+\alpha} \tag{A.17}$$

where α is the aspect ratio of the channel.

Rearranging A.17, s is found:

$$s = \frac{D_{h_{ch}}(1+\alpha)}{2} \tag{A.18}$$

Substituting s from A.18 to A.16, τ_w is found:

$$\tau_w = \frac{12\,\mu\, V_{ch}}{D_{h_{ch}}(1+\alpha)} \tag{A.19}$$

Appendix B

Thermal Joint Resistance Model

Heat transfer from a package to a heat sink base encounters a thermal resistance at the interface called thermal joint resistance, R_j because only a fraction of the total apparent area is in contact because of the surface irregularities at the interface face. Thermal joint resistance at the interface is a function of several geometric, physical and thermal parameters such as surface roughness and waviness, surface micro-hardness, thermal conductivity of the contacting solids, properties of the interstitial materials, and the contact pressure. Thermal joint resistance can be minimized by the use of a Thermal Interface Material (TIM).

The thermal joint resistance of a joint formed by two nominally flat rough surfaces filled with thermal interface materials (TIMs) (Fig. B.1) can be obtained from a model [46] that is based on following simplifying assumptions:

- Surfaces are nominally flat and rough with Gaussian height distributions.
- The load is supported by the contacting asperities only.
- The load is light; nominal contact pressure is small; $P/H_c \approx 10^{-3}$ to 10^{-5}
- TIM is homogeneous, fills the interstitial gaps completely, and wets the bounding surfaces perfectly.

In general, the joint conductance h_j and joint resistance R_j depends on the contact and gap components. The joint conductance is modeled as [56]:

$$h_j = h_c + h_g \tag{B.1}$$

The joint resistance is modeled as:

$$\frac{1}{R_j} = \frac{1}{R_c} + \frac{1}{R_g} \tag{B.2}$$

where R_c is the contact resistance and R_g is the gap resistance.

R_c can be obtained from the contact conductance relationship for conforming rough surfaces and plastic deformation of contacting asperities [56]:

$$h_c = \frac{1}{R_c A_a} = 1.25\, K_s \left(\frac{m}{\sigma}\right) \left(\frac{P}{H_c}\right)^{0.95} \tag{B.3}$$

where A_a is the apparent area of contact of two joining surfaces and k_s is the harmonic mean thermal conductivity of the two contacting surfaces of thermal conductivity k_1 and k_2 and expressed as:

$$k_s = \frac{2\,k_1\,k_2}{k_1 + k_2} \tag{B.4}$$

The effective rms surface roughness σ of the two contacting surfaces with roughness σ_1 and σ_2 can be expressed as:

$$\sigma = \sqrt{\sigma_1^2 + \sigma_2^2} \tag{B.5}$$

The effective absolute mean asperity slope m can be obtained from the individual absolute mean asperity slopes of two contacting materials m_1 and m_1.

$$m = \sqrt{m_1^2 + m_2^2} \tag{B.6}$$

If the absolute mean asperity slopes m_1 and m_1 are unknown, they can be obtained from the approximate correlation equation of Antonetti et al. [1]:

$$m_i = 0.1259 \left(\sigma_i \cdot 10^6\right)^{0.402}, \qquad i = 1,2 \tag{B.7}$$

The contact pressure is P and H_c is the surface micro-hardness of the softer of the two contacting solids.

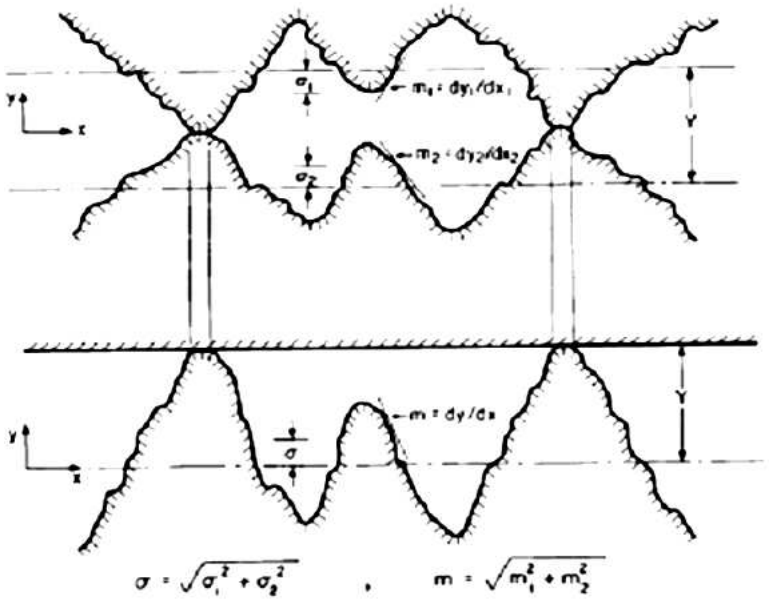

Figure B.1: Contact of an Equivalent Rough Surface and Smooth Plane Contact [47]

Based on the assumptions given above, the gap conductance is modeled as an equivalent layer of thickness $t = Y$ filled with TIM having thermal conductivity k_g. The joint resistance obtained from gap conductance can be expressed as:

$$h_g = \frac{1}{R_g A_a} = \frac{k_g}{Y + M} \tag{B.8}$$

$$R_g = \frac{Y + M}{A_a k_g} \tag{B.9}$$

$M = 0$ if the gap is filled with TIM, if the gap is filled with air, $M = \alpha\,\beta\,\Lambda$.

For air, gas parameters α = 2.4, β = 1.7 and molecular free path Λ = 0.06 μm.

The mean plane separation Y, shown in Fig. B.1, is given approximately by the simple power law relation [1]:

$$\frac{Y}{\sigma} = 1.53 \left(\frac{P}{H_c}\right)^{-0.097} \tag{B.10}$$

Using above relationships, R_j can be expressed as:

$$R_j = \frac{1}{\frac{1}{R_c} + \frac{1}{R_g}} \tag{B.11}$$

$$R_j = \left[\left\{1.25\,K_s \left(\frac{m}{\sigma}\right) \left(\frac{P}{H_c}\right)^{0.95} + \frac{k_g}{Y + M}\right\} A_a\right]^{-1} \tag{B.12}$$

For light contact pressures it is assumed that $R_c \gg R_g$. The joint resistance depends on the gap only; therefore,

$$\frac{1}{R_j} = \frac{1}{R_g} \tag{B.13}$$

The power law relation of Eq. B.10 shows that Y/σ is a relatively weak function of the relative contact pressure. Using this relation, the joint resistance may be expressed as:

$$R_j = \frac{1.53\,\sigma \left(\frac{P}{H_c}\right)^{-0.097}}{A_a\, k_g} \tag{B.14}$$

which show clearly how the geometric, physical, and thermal parameters influence the joint resistance.

The above model will be used to calculate the joint resistance formed between an aluminium 6063-T5 (k_1=201 $W/m\cdot K$) heat sink and an Al_2O_3 (k_2=20.9 $W/m\cdot K$) package filled with TIM ($k_g = 0.735\,W/m\cdot K$ of Wakefield Type 120) and air ($k_a = 0.026\,W/m\cdot K$). The micro-hardness of the aluminium alloy $H_c = 1094\,MPa$, and based on commonly used surface roughness of aluminium heat sink of $\sigma = 0.1\mu m$ (4 micro-inch) and a surface roughness for alumina of $\sigma = 1.3\mu m$ are used to compute contact parameters. Package dimension is assumed as $50\,mm \times 50\,mm$ and the dimensions of a heat sink used in experiment is found as L = 100 mm, B = 100 mm, t_b = 10 mm, t = 1 mm and number of fins, N = 28. For aluminium of density ρ = 2702 kg/m^3, the weight of the heat sink is found as $5.83\,N$. A_a is found between package and heat sink as $50\,mm \times 50\,mm$ for which P can be calculated from A_a as 0.06 MPa. P/H_c is found as 5.5×10^{-5}.

The specific thermal joint resistances are plotted for TIM and air in Fig. B.2 against the contact pressure over the range $0.012 \leq P(MPa) \leq 1$. It is observed that the calculated values of the joint resistance with TIM are more than an order of magnitude smaller than the joint resistance of a bare joint. The comparison of resistances for thermal joint resistance model are shown in the Table B.1:

Thermal joint resistances is compared with the other resistances associated with a heat sink in fully shrouded configures with relatively high duct velocity (3 m/s) as those resistances are found minimum in fully shrouded configuration and at high duct velocity [Table B.2].

Table B.1: Thermal Joint Resistances with TIM and Air

P MPa	P/H_c	Interface Material	R_c K/W	R_g K/W	R_j K/W
0.06	5.5×10^{-5}	TIM	0.83	0.003	0.003
		Air	0.83	0.083	0.076

Table B.2: Comparison of Resistances Associated with a Heat Sink

Resistance	Value	Unit	Contribution
R_j	3.0×10^{-3}	K/W	1.1% of R_{th}
R_m	4.0×10^{-3}	K/W	1.45% of R_{th}
R_s	2.2×10^{-2}	K/W	7.99% of R_{th}
R_c	4.0×10^{-3}	K/W	1.6% of R'_{fin}
R_{fin}	2.491×10^{-1}	K/W	-
R'_{fin}	2.531×10^{-1}	K/W	-
R_{film}	9.43	K/W	-
R_{hs}	2.465×10^{-1}	K/W	89.5% of R_{th}
R_{th}	2.755×10^{-1}	K/W	-

where

$$
\begin{aligned}
R'_{fin} &= R_c + R_{fin} \\
R_{hs} &= \frac{1}{\frac{1}{R'_{fin}} + \frac{1}{R_{film}}} \\
R_{th} &= R_j + R_m + R_s + R_{hs}
\end{aligned}
$$

Based on the resistor network (Fig. B.2), R_{th} is expressed as:

$$
R_{th} = R_j + R_s + R_m + \frac{1}{\frac{1}{R_c + R_{fin}} + \frac{1}{R_{film}}} \tag{B.15}
$$

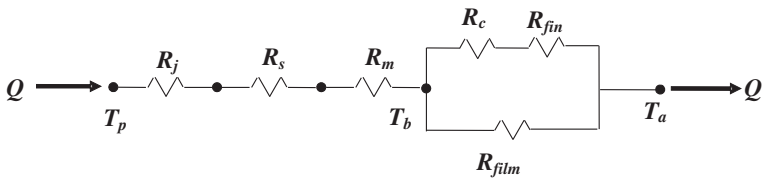

Figure B.2: Thermal Circuit of Resistor Network

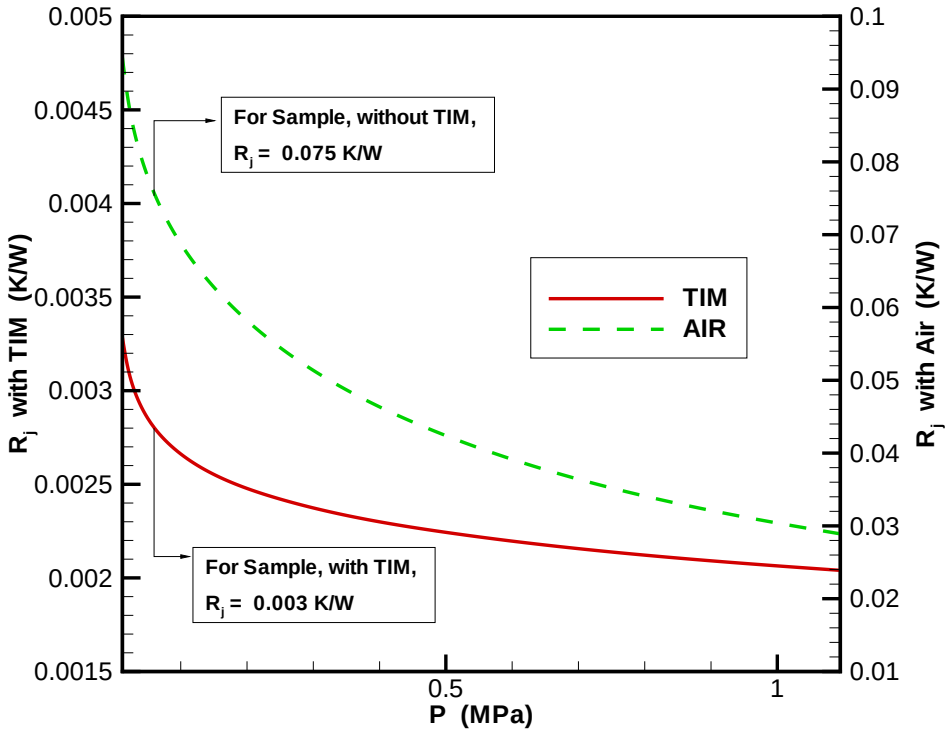

Figure B.3: Contact of an Equivalent Rough Surface and Smooth Plane Contact

Appendix C

Error Analysis

C.1 Introduction

Model data were compared with the data of experiments and earlier literature in Chapter 4. The procedure to calculate the deviation (error or difference) is discussed in this appendix.

C.2 Definition of Errors

$$\textbf{\% Error}_i = \frac{x_{c_i} - x_{m_i}}{x_{c_i}} \times 100 \tag{C.1}$$

where x_c = compared data; in our research, compared data is experimental data (x_e) and literature data (x_l), i is number of data.

$$\textbf{\% RMS Error} = \sqrt{\frac{1}{n} \times \sum_{i=1}^{n} \%\,\textbf{Error}_i{}^2} \tag{C.2}$$

$$\textbf{\% Average Error} = \frac{1}{n} \times \sum_{i=1}^{n} \%\,\textbf{Error}_i \tag{C.3}$$

C.3 Differences of Model and Experimental Data

Geometry of the heat sink used for experiments is shown in the following table:

B	L	H	s	t	N	t_b
mm	mm	mm	mm	mm		mm
102	101	51	2.75	1.00	28	8.0

The differences of model and experimental data are shown in Tables C.1 and C.2.

Table C.1: Error for Pressure Drop, ΔP_{hs}

B	CB	H	CH	V_d	ΔP_{hs} (pa)		Error	Av. Error	RMS Error
mm	mm	mm	mm	m/s	Expt.	Model	%	%	%
				1.00	4.56	5.22	14.42		
				1.50	7.92	8.56	8.05		
102	108	51	54	2.00	11.16	12.26	9.86	9.28	9.70
				2.50	15.13	16.33	7.88		
				3.00	19.53	20.74	6.20		
				1.00	2.84	3.39	19.37		
				1.50	5.10	5.80	13.73		
102	108	51	54	2.00	7.94	8.50	7.05	10.66	11.83
				2.50	10.87	11.54	6.16		
				3.00	13.92	14.89	6.97		
				1.00	1.87	2.17	16.35		
				1.50	3.62	3.91	8.01		
102	108	51	54	2.00	5.23	5.93	13.38	10.03	10.86
				2.50	7.85	8.26	5.22		
				3.00	10.06	10.78	7.16		
				1.00	1.31	1.61	22.90		
				1.50	2.76	3.07	11.23		
102	108	51	54	2.00	4.45	4.75	6.74	11.44	12.88
				2.50	6.23	6.72	7.87		
				3.00	8.17	8.86	8.45		

Table C.2: Error for Thermal Resistance, R_{th}

B	CB	H	CH	V_d	R_{th} (K/W)		Error	Av. Error	RMS Error
mm	mm	mm	mm	m/s	Expt.	Model	%	%	%
102	108	51	54	1.00	0.27	0.24	14.26	7.09	7.99
				1.50	0.19	0.20	5.37		
				2.00	0.17	0.18	4.49		
				2.50	0.16	0.16	4.48		
				3.00	0.14	0.15	6.83		
102	127	51	64	1.00	0.32	0.29	8.83	2.49	4.07
				1.50	0.23	0.23	1.98		
				2.00	0.20	0.20	0.64		
				2.50	0.18	0.18	0.19		
				3.00	0.17	0.17	0.80		
102	152	51	76	1.00	0.44	0.38	13.45	5.77	7.21
				1.50	0.29	0.27	5.98		
				2.00	0.24	0.22	5.50		
				2.50	0.21	0.20	3.52		
				3.00	0.18	0.18	0.37		
102	178	51	89	1.00	0.51	0.47	7.92	7.08	8.14
				1.50	0.36	0.31	13.63		
				2.00	0.26	0.25	6.87		
				2.50	0.23	0.21	5.83		
				3.00	0.19	0.19	1.14		

C.4 Differences of Model and Literature Data

C.4.1 Butterbugh and Kang (1995)

Geometry of the heat sink used for experiments is shown in the following table:

B	L	H	s	t	N	t_b
mm	mm	mm	mm	mm		mm
46	46	53	2.4	1.27	13	6.0

Table C.3: Error for Pressure Drop, ΔP_{hs}

B	CB	H	CH	V_d	ΔP_{hs} (pa)		Error	Av. Error	RMS Error
mm	mm	mm	mm	m/s	Expt.	Model	%	%	%
46	46	53	53	1.00	4.76	3.90	18.07	21.66	21.93
				2.00	12.20	9.86	19.18		
				3.00	22.40	17.34	22.59		
				4.00	35.70	26.13	26.81		
46	46	53	66	1.00	3.17	2.69	15.14	18.87	19.33
				2.00	8.40	7.12	15.24		
				3.00	16.00	12.83	19.81		
				4.00	26.20	19.57	25.31		
46	46	53	78	1.00	2.57	2.05	20.23	19.53	19.57
				2.00	6.93	5.71	17.60		
				3.00	13.00	10.47	19.46		
				4.00	20.40	16.15	20.83		
46	46	53	91	1.00	2.06	1.69	17.96	17.05	17.29
				2.00	5.53	4.83	12.66		
				3.00	10.80	8.97	16.94		
				4.00	17.60	13.97	20.63		

Table C.4: Error for Pressure Drop, ΔP_{hs}: Table C.3 ....continued

B	CB	H	CH	V_d	ΔP_{hs} (pa)		Error	Av. Error	RMS Error
mm	mm	mm	mm	m/s	Expt.	Model	%	%	%
46	46	53	155	1.00	0.97	1.06	9.28	9.56	9.99
				2.00	2.97	3.31	11.45		
				3.00	5.66	6.37	12.54		
				4.00	9.64	10.12	4.98		
46	59	53	53	1.00	3.43	2.98	13.12	13.29	13.98
				2.00	8.19	7.67	6.35		
				3.00	16.20	13.64	15.80		
				4.00	25.10	20.61	17.89		
46	71	53	53	1.00	2.41	2.24	7.05	7.57	8.97
				2.00	6.24	6.03	3.37		
				3.00	11.40	10.91	4.30		
				4.00	19.80	16.72	15.56		
46	84	53	53	1.00	1.76	1.79	1.70	10.49	11.97
				2.00	5.62	5.04	10.32		
				3.00	10.50	9.22	12.19		
				4.00	17.40	14.31	17.76		
46	148	53	53	1.00	1.38	1.09	21.01	17.31	17.76
				2.00	3.74	3.34	10.70		
				3.00	7.79	6.40	17.84		
				4.00	12.60	10.12	19.68		
46	198	53	53	1.00	1.16	0.93	19.83	16.26	16.56
				2.00	3.36	2.95	12.20		
				3.00	6.66	5.71	14.26		
				4.00	11.20	9.10	18.75		
46	97	53	78	1.00	1.28	1.35	5.47	7.15	8.09
				2.00	3.47	3.94	13.54		
				3.00	7.10	7.36	3.66		
				4.00	10.80	11.44	5.93		

Table C.5: Error for Thermal Resistance, R_{th}

B	CB	H	CH	V_d	R_{th} (K/W)		Error	Av. Error	RMS Error
mm	mm	mm	mm	m/s	Expt.	Model	%	%	%
46	46	53	53	1.00	0.70	0.73	4.29	3.49	3.63
				2.00	0.58	0.59	2.26		
				3.00	0.52	0.53	2.72		
				4.00	0.47	0.49	4.68		
46	46	53	66	1.00	0.75	0.82	9.04	5.32	5.74
				2.00	0.61	0.63	4.13		
				3.00	0.54	0.56	3.90		
				4.00	0.50	0.52	4.21		
46	46	53	78	1.00	0.79	0.91	14.90	8.04	8.99
				2.00	0.62	0.67	6.91		
				3.00	0.55	0.58	5.24		
				4.00	0.51	0.54	5.10		
46	46	53	91	1.00	0.84	0.99	17.96	9.26	10.56
				2.00	0.65	0.69	7.44		
				3.00	0.57	0.60	5.45		
				4.00	0.52	0.55	6.18		
46	46	53	155	1.00	1.16	1.24	6.90	3.23	3.92
				2.00	0.75	0.77	3.08		
				3.00	0.64	0.65	1.57		
				4.00	0.58	0.59	1.38		
46	59	53	53	1.00	0.75	0.80	5.44	4.80	5.15
				2.00	0.61	0.62	2.47		
				3.00	0.54	0.58	7.45		
				4.00	0.49	0.51	3.85		

Table C.6: Error for Thermal Resistance, R_{th}: Table C.5 ....continued

B	CB	H	CH	V_d	R_{th} (K/W)		Error	Av. Error	RMS Error
mm	mm	mm	mm	m/s	Expt.	Model	%	%	%
46	71	53	53	1.00	0.83	0.88	6.17	5.37	5.41
				2.00	0.63	0.66	4.46		
				3.00	0.55	0.58	5.09		
				4.00	0.50	0.53	5.77		
46	84	53	53	1.00	0.91	0.96	5.16	4.61	4.69
				2.00	0.66	0.69	4.39		
				3.00	0.58	0.60	3.29		
				4.00	0.52	0.55	5.59		
46	148	53	53	1.00	1.12	1.22	8.93	6.39	6.58
				2.00	0.72	0.77	6.08		
				3.00	0.61	0.65	5.89		
				4.00	0.56	0.59	4.64		
46	198	53	53	1.00	1.25	1.34	7.20	7.55	7.573
				2.00	0.74	0.80	7.82		
				3.00	0.62	0.67	8.41		
				4.00	0.56	0.60	6.76		
46	97	53	78	1.00	1.03	1.09	5.83	4.55	4.69
				2.00	0.69	0.73	5.48		
				3.00	0.61	0.63	3.29		
				4.00	0.55	0.57	3.62		

Appendix D

Uncertainty Analysis

D.1 Introduction

The results obtained from any experimental procedures have some uncertainties associated with them. The uncertainty may be due to the imperfection of the test apparatus, imperfection of the theory for data reduction, incorrect assumptions or careless measurements. It is very important that the output of the measurement system truly reflects the actual value of the measurand. The uncertainty of a measurement is defined as the difference between the measured value and the true value of the measurand. Errors in experiment generally fall into two categories: bias errors (fixed or systematic errors) and precision errors (random errors). Precision errors are detected by a lack of repeatability in the measurement output and can be reduced by generating multiple data and averaging them. Bias errors are often not obvious to the experimenter and very difficult to reduce. Major sources of the bias errors are calibration error, accuracy of the instrument etc. The uncertainty of a measurement system is an estimate of the limits of errors in the measurements. In a typical measurement system, there are a large number of error sources known as elemental error sources and each can generate either a bias or precision error.

An uncertainty analysis of the experimental method, apparatus and data is performed in the following sections. Following assessment of the accuracy of each of the instruments and sensors used in the experiment, the impact of these uncertainties on the reported value of pressure drop, dimensionless pressure drop, Reynolds number, thermal resistance, convective heat transfer coefficient and Nusselt number is presented.

D.2 Measurement of Uncertainties

When estimating the uncertainty in measured and calculated quantities, both bias and precision errors need to be considered. These elemental errors are combined to give an overall uncertainty in a measured quantity using the root-sum-squares method. This method is expressed mathematically in Eq. D.1:

$$u_x = \pm \left[e_{bias}^2 + e_{precision}^2 \right]^{\frac{1}{2}} \tag{D.1}$$

where u_x represents the uncertainty in the measured quantity x. The estimation of bias errors (e_{bias}) is based on the accuracy of the instruments, while the estimation of precision errors $(e_{precision})$ is based on statistical analysis of the data.

D.2.1 Uncertainties of Precision Errors

Uncertainties associated with precision error are calculated based on statistical analysis of the data assuming a 95% confidence interval. To estimate the precision uncertainty of a measurement, multiple readings are taken, typically on the order of 50, the sample standard deviation is calculated using Eq. D.2, and multiplied by the appropriate Student t factor.

$$S_x = \sqrt{\frac{1}{N-1} \sum_{i=1}^{N} (x_i - \bar{x})^2} \tag{D.2}$$

In all instances, the value of t is taken to be 2, which corresponds to 60 independent measurements (degrees of freedom) and a 95% confidence interval ($\alpha/2$= 0.025). Thus, the estimation of precision uncertainty can be expressed by Eq. D.3.

$$e_{precision} = \pm t_{\frac{\alpha}{2}} S_x \tag{D.3}$$

D.2.2 Uncertainties of Bias Errors

The uncertainty in the experimental measurement or bias error has been determined using the root sum square method described by Holman (1984) and Moffat (1988). In any experimental program, a set of measurements is made, and these measurements are then used to calculate some desired result of the experiments. The uncertainty in the calculated result is estimated on the basis of the uncertainties in the primary measurements. The result R is a given function of the independent variables $x_1, x_2, x_3, ..., x_n$. Thus

$$R = R(x_1, x_2, x_3, ..., x_n) \tag{D.4}$$

Let w_R be the uncertainty in the result and $w_1, w_2, w_3, ..., w_n$ be the uncertainties in the independent variables. If the uncertainties in the independent variables are all given, then the uncertainty in the result is given as

$$w_R = \left[\left(\frac{\partial R}{\partial x_1} w_1 \right)^2 + \left(\frac{\partial R}{\partial x_2} w_2 \right)^2 + \cdots\cdots\cdots + \left(\frac{\partial R}{\partial x_n} w_n \right)^2 \right]^{\frac{1}{2}} \tag{D.5}$$

Uncertainties for Product Functions

In many cases the result function R takes the form of a product of the respective primary variables raised to exponents and expressed as:

$$R = {x_1}^{a_1} {x_2}^{a_2} ..... {x_n}^{a_n} \tag{D.6}$$

When primary variables are raised to exponents, the uncertainty in the result R is given as:

$$e_{bias} = \frac{w_R}{R} = \left[\sum \left(\frac{a_i w_{x_i}}{x_i} \right)^2 \right]^{\frac{1}{2}} = \left[\left(\frac{a_1 w_{x_1}}{x_1} \right)^2 + \left(\frac{a_2 w_{x_2}}{x_2} \right)^2 + \cdots + \left(\frac{a_n w_{x_n}}{x_n} \right)^2 \right] \tag{D.7}$$

The result of this equation is the uncertainty in R expressed as a percentage.

Uncertainties for Additive Functions

When the result function has an additive form, R will be expressed as:

$$R = a_1 x_1 + a_2 x_2 + \cdots\cdots\cdots + a_n x_n = \sum a_i x_i \tag{D.8}$$

The uncertainty in the result may then be expressed as:

$$\begin{aligned} w_R &= \left[\sum (a_i w_{x_i})^2\right]^{\frac{1}{2}} \\ e_{bias} &= \frac{w_R}{R} \end{aligned} \tag{D.9}$$

The experiment was conducted with a sample size of 50 for each reported data point, and uncertainties associated with precision and bias errors were considered to calculate the overall uncertainty. It has been observed that the contribution of precision error is neglible on overall uncertainty and has been ignored in the sample calculation of the following section.

$$u_x = \pm\, e_{bias}$$

The following section describes the uncertainty associated with the instrumentation and methods used in the measurement (bias errors) of each of the individual quantities in the experimental test program.

D.3 Uncertainty in Measured Values

Sample calculation of uncertainty in measured value is presented for the follow configuration of experiment.

One Case of Experiment

Q	V_d	Bypass	
W	m/s	CB/B	CH/H
50	2	1.5	1.5

Heat Sink Geometry								
L	B	H	s	t	t_b	N	Material	
mm	mm	mm	mm	mm	mm		Fin	Base
100	95.5	50	2.5	1	8	28	Al	Al

Experimental Data

T_a	T_b	Voltage	Current		Pressure				
					P_a	P_1		P_2	
^0C	^0C	V	V_{shunt}	I	h (m of Hg)	V	Pa	V	Pa
21.8	28.6	27.66	.0181	1.81	.7285	1.293	3.9	1.464	6.57

D.3.1 Temperature Measurements

All temperature measurement were performed using T-type thermocouples and a Keithley 2700 data acquisition system. From the calibration specification (Keithley, 2001) the accuracy of T-type thermocouple measurement is found:

$$w_T = \pm 0.2 \quad [^0C]$$

The uncertainty in the temperature measurement is found:

$$\frac{w_T}{T} = \pm \frac{0.2 \ [^0C]}{T \ [^0C]}$$

The uncertainty in the base plate temperature, $T_b = 28.6^0C$ is measured:

$$\frac{w_{T_b}}{T_b} = \pm\frac{0.2\ [^0C]}{T_b\ [^0C]} = \pm\frac{0.2}{28.6} = \pm 0.007 = \pm 0.7\ \%$$

The uncertainty in the ambient temperature, $T_a = 21.8^0C$ is measured:

$$\frac{w_{T_a}}{T_a} = \pm\frac{0.2\ [^0C]}{T_a\ [^0C]} = \pm\frac{0.2}{21.8} = \pm 0.009 = \pm 0.9\ \%$$

The uncertainty of base plate temperature and ambient temperature are found to be 0.7% **and** 0.9% **respectively.**

D.3.2 Heater Voltage

The voltage applied to the cartridge resistance heaters embedded underneath the base plate is measured using the Keithley data logger. The range of voltage used in these test is $15V < V_{heater} < 50V$, and the corresponding accuracy of the measurements from the calibration specifications of the instrument (Keithley, 2001) is:

$$w_{V_{heater}} = \pm\left(4.5\times10^{-5}\times V_{heater} + 9\times10^{-6}\times Range\right) \tag{D.10}$$

Rearranging the Eq. D.10:

$$\frac{w_{V_{heater}}}{V_{heater}} = \pm\left(4.5\times10^{-5} + 9\times10^{-6}\times\frac{Range}{V_{heater}}\right) \tag{D.11}$$

For the 100 V range and $V_{heater} = 27.66$, the resulting uncertainty of the heater supplied voltage is found:

$$\frac{w_{V_{heater}}}{V_{heater}} = \pm\left(4.5\times10^{-5} + 9\times10^{-6}\times\frac{100}{27.66}\right) = \pm 7.8\times10^{-5}$$

The uncertainty for the heater supplied voltage is $\pm$ **0.0078%**

D.3.3 Heater Current

The current in the heater is calculated based on the voltage drop across a calibrated shunt resistor:

$$I = \frac{V_{shunt}}{\Re} = {V_{shunt}}^{1} \times \Re^{-1} \tag{D.12}$$

$$a_{V_{shunt}} = 1; \;\; a_{\Re} = -1$$

Comparing with Eq. D.7, the uncertainty for the heater current is found:

$$\frac{w_I}{I} = \left[\left(\frac{a_{V_{shunt}} w_{V_{shunt}}}{V_{shunt}} \right)^2 + \left(\frac{a_{\Re} w_{\Re}}{\Re} \right)^2 \right]^{\frac{1}{2}} \tag{D.13}$$

From the specifications for the data logger (Keithley, 2001) the uncertainty in the voltage readings across the shunt resistor is found:

$$w_{V_{shunt}} = \pm \left(3.0 \times 10^{-5} \times V_{shunt} + 3.5 \times 10^{-5} \times Range \right) \quad [V] \tag{D.14}$$

Rearranging the Eq. D.14:

$$\frac{w_{V_{shunt}}}{V_{shunt}} = \pm \left(3.0 \times 10^{-5} + 3.5 \times 10^{-5} \times \frac{Range}{V_{shunt}} \right) \tag{D.15}$$

For the 100 mV range and $V_{shunt} = 18.1\ mv$, the resulting uncertainty for the shunt voltage is found:

$$\frac{w_{V_{shunt}}}{V_{shunt}} = \pm \left(3.0 \times 10^{-5} + 3.5 \times 10^{-5} \times \frac{100}{18.1} \right) = \pm\, 0.000223 \times 10^{-5}$$

The uncertainty for the shunt voltage is 0.0223%

The resistance of the shunt is measured during a calibration procedure at the start of the experimental test program. Using the Keithley data logger to measure current as the full range of voltages were supplied to the shunt, $0 < V_{shunt} < 50\ mv$, the resistance is calculated based on a linear fit of the voltage versus current data. The uncertainty in the calculated resistance is determined by:

$$\frac{w_{\Re}}{\Re} = \left[\left(\frac{w_{V_{shunt}}}{V_{shunt}} \right)^2 + \left(\frac{w_{I_s}}{I_s} \right)^2 + \left(\frac{w_{\angle}}{\angle} \right)^2 \right]^{\frac{1}{2}} \tag{D.16}$$

where the uncertainty associated with the linear fit of the data, $w_{\angle}/\angle$, is the RMS % difference between the linear fit and the data.

$$\frac{w_{\angle}}{\angle} = 0.09\,\% = \pm 0.0009$$

The uncertainty in the shunt current measurement is calculated from (Keithley, 2001):

$$\frac{w_{I_s}}{I_s} = \pm\left(8.0\times10^{-4} + \frac{4.0\times10^{-5}\ [A]}{I\qquad\quad [A]}\right) \tag{D.17}$$

The uncertainty in the resistance is tested at the nominal current value, I $\approx$ 0.1 A, and the uncertainty in the shunt current is determined:

$$\frac{w_{I_s}}{I_s} = \pm\left(8.0\times10^{-4} + \frac{4.0\times10^{-5}\ [A]}{0.1\qquad\quad [A]}\right) = \pm\,0.0012$$

Substituting the value of $\frac{w_{V_{shunt}}}{V_{shunt}} = \pm 0.0223$, $\frac{w_{I_s}}{I_s} = \pm 0.0012$ and $\frac{w_{\angle}}{\angle} = \pm 0.0009$ in Eq. D.16:

$$\frac{w_{\Re}}{\Re} = \pm\left[(.0223)^2 + (0.0012)^2 + (0.0009)^2\right]^{\frac{1}{2}} = \pm 0.02235 = \pm 2.24\%$$

The uncertainty of the shunt resistance is found to be 2.24 %.

Substituting the value of $\frac{w_{V_{shunt}}}{V_{shunt}} = \pm 0.0223$, $\frac{w_{\Re}}{\Re} = \pm 0.02235$, $a_{V_{shunt}} = 1$, and $a_{\Re}$ = -1 in Eq. D.13:

$$\frac{w_I}{I} = \left[\{(1)\times(.0223)\}^2 + \{(-1)\times(.02235)\}^2\right]^{\frac{1}{2}} = \pm 0.0316 = \pm 3.16\%$$

The uncertainty of the heater current is found to be 3.16 %.

D.3.4 Pressure

The uncertainty of pressure is associated with the measurement of atmospheric pressure and system pressure.

In both cases, pressure is measured from the following equation:

$$P = h^1\,\rho^1\,g^1 \tag{D.18}$$

where g is constant (9.81 m/s^2)

Comparing with Eq. D.7, the uncertainty of pressure is written as:

$$\frac{w_P}{P} = \left[\left(\frac{w_h}{h}\right)^2 + \left(\frac{w_\rho}{\rho}\right)^2\right]^{\frac{1}{2}} \tag{D.19}$$

Atmospheric Pressure

The atmospheric pressure is read from a barometer in h (m of mercury) and the accuracy of barometer is found, $w_h = \pm 0.0005\,m$, and ρ of mercury can be assumed constant at atmospheric conditions.

The uncertainty of atmospheric pressure is written as;

$$\frac{w_{P_a}}{P_a} = \frac{w_{h_a}}{h_a} \tag{D.20}$$

For the given sample, $h_a = 0.7285$ m of Hg.

Therefore, the uncertainty in the atmospheric pressure is calculated as:

$$\frac{w_{P_a}}{P_a} = \frac{0.0005}{0.7285} = \pm\, 0.0007$$

The uncertainty in the atmospheric pressure is found to be 0.07 %.

Heat Sink Inlet Pressure, P_1

P_1 is read by a pressure transducer in voltage (V), and this voltage is then transmitted through the Keithley data logger for further recording as h_1 (m of water) from the vendor supplied relationship.

The relationship of h_1 with V_1 is given as:

$$h_1 = \frac{V_1 - V_0}{5 - V_0}\, h_{range} \tag{D.21}$$

The uncertainty of h_1 associated with the uncertainty of the pressure transducer and the data logger is written as:

$$\frac{w_{h_1}}{h_1} = \left[\left(\frac{w_{h_{PT}}}{h_{PT}} \right)^2 + \left(\frac{w_{V_{DL}}}{V_{DL}} \right)^2 \right]^{\frac{1}{2}} \tag{D.22}$$

PT = Pressure Transducer; DL = Data Logger

The uncertainty of data logger is calculated using Eq. D.15. For the 100 V range and $V_{DL} = 1.293$ V for heat sink inlet pressure, the resulting uncertainty in the data logger is found:

$$\frac{w_{V_{DL}}}{V_{DL}} = \pm \left(4.5 \times 10^{-5} + 9 \times 10^{-6} \times \frac{100}{1.293} \right) = \pm 0.000741$$

From the vendor specification sheet, the uncertainty of the pressure transducer is found:

$$\frac{w_{h_{PT}}}{h_{PT}} = \pm 0.0025$$

The uncertainty of h_1 is calculated as:

$$\frac{w_{h_1}}{h_1} = \left[(0.0025)^2 + (0.000741)^2\right]^{\frac{1}{2}} = \pm\, 0.0026$$

Density (ρ) of water is assumed constant at this particular temperature and pressure. Therefore, uncertainty of P_1 is found:

$$\frac{w_{P_1}}{P_1} = \frac{w_{h_1}}{h_1} = \pm\, 0.0026 = \pm\, 0.26\,\%$$

The uncertainty associated with P_1 is found to be $\pm$ 0.26 %

By applying same procedure, **The uncertainty associated with P_2 is found to be $\pm$ 0.26 %**

D.3.5 Air density, ρ_{air}

ρ_{air} is calculated using the following relationship:

$$\rho_{air} = \frac{P_a}{R_{air}\, T_a} = {P_a}^1\, {R_{air}}^{-1}\, {T_a}^{-1} \tag{D.23}$$

R_{air} is constant (287 J/kg.K).

The uncertainty associated with ρ_{air} can be written as:

$$\frac{w_{\rho_{air}}}{\rho_{air}} = \left[\left(\frac{w_{P_a}}{P_a}\right)^2 + \left(-1\,.\frac{w_{T_a}}{T_a}\right)^2\right]^{\frac{1}{2}} \tag{D.24}$$

The uncertainty associated with atmospheric pressure and temperature were ± 0.0007 and ± 0.009 respectively.

The uncertainty associated with ρ_{air} is found:

$$\frac{w_{\rho_{air}}}{\rho_{air}} = \left[(.0007)^2 + (.009)^2\right]^{\frac{1}{2}} = \pm 0.009 = \pm 0.9\%$$

The uncertainty associated with ρ_{air} is $\pm$ 0.9 %

D.3.6 Air viscosity, μ_{air}

μ_{air} is calculated using the following power law relationship:

$$\mu = \mu_0 \left(\frac{T_a}{T_0}\right)^{0.7} \tag{D.25}$$

where $T_0 = 273$ K, $\mu_0 = 1.71$ E-5 kg/(m.s), and T in kelvins.

The uncertainty associated with μ_{air} is written as:

$$\frac{w_{\mu_{air}}}{\mu_{air}} = 0.7\,\frac{w_{T_a}}{T_a} \tag{D.26}$$

The uncertainty associated with T_a is $\pm$ 0.009 %.

The uncertainty of μ_{air} is:

$$\frac{w_{\mu_{air}}}{\mu_{air}} = 0.7 \times 0.009 = \pm\, 0.0063 = \pm\, 0.63\%$$

The uncertainty associated with μ_{air} is $\pm$ 0.63 %

D.3.7 Duct Velocity, V_d

V_d is measured using the following relationship:

$$V_d = \frac{\forall}{A_d} = \frac{\forall}{CB \times CH} = \forall^1\, CB^{-1}\, CH^{-1} \tag{D.27}$$

The uncertainty associated with V_d is written as:

$$\frac{w_{V_d}}{V_d} = \left[\left(\frac{w_\forall}{\forall}\right)^2 + \left(-1.\frac{w_{CB}}{CB}\right)^2 + \left(-1.\frac{w_{CH}}{CH}\right)^2\right]^{\frac{1}{2}} \tag{D.28}$$

$\forall$ is measured by following vendor supplied relationship for the nozzle:

$$\forall = A_n \times V_n = \alpha A_n \left[\frac{2\Delta P_n}{\rho_{air}}\right]^{\frac{1}{2}} = \sqrt{2}\,\alpha A_n\, \Delta P_n{}^{\frac{1}{2}}\, \rho_{air}{}^{-\frac{1}{2}} \tag{D.29}$$

where A_n is nozzle area and α is dimensionless flow coefficient obtained directly from supplied vendor specification sheet.

The uncertainty associated with $\forall$ is given as:

$$\frac{w_{\forall}}{\forall} = \left[\left(\frac{1}{2} \frac{w_{\Delta P_n}}{\Delta P_n} \right)^2 + \left(-\frac{1}{2} \frac{w_{\rho_{air}}}{\rho_{air}} \right)^2 \right]^{\frac{1}{2}} \tag{D.30}$$

The uncertainty associated with ΔP_n is given as:

$$\frac{w_{\Delta P_n}}{\Delta P_n} = \left[\left(\frac{w_{h_{PT}}}{h_{PT}} \right)^2 + \left(\frac{w_{V_{DL}}}{V_{DL}} \right)^2 \right]^{\frac{1}{2}}$$

From the vendor specification sheet, the uncertainty of the pressure transducer is found:

$$\frac{w_{h_{PT}}}{h_{PT}} = \pm 0.0025$$

The uncertainty of the data logger is calculated using Eq. D.11. For the 100 V range and voltage associated with pressure drop around the nozzle, $V_{DL} = 1.702352$ V, the resulting uncertainty in the data logger is found:

$$\frac{w_{V_{DL}}}{V_{DL}} = \pm \left(4.5 \times 10^{-5} + 9 \times 10^{-6} \times \frac{100}{1.702352} \right) = \pm 0.000574$$

Therefore, the uncertainty associated with ΔP_n is:

$$\frac{w_{\Delta P_n}}{\Delta P_n} = \left[(0.0025)^2 + (0.000574)^2 \right]^{\frac{1}{2}} = \pm 0.002565$$

From subsection D.3.5, the uncertainty of ρ_{air} is found:

$$\frac{w_{\rho_{air}}}{\rho_{air}} = \pm\, 0.009$$

The uncertainty associated with Q is found:

$$\frac{w_{\forall}}{\forall} = \left[\left(\frac{1}{2} \times .002565 \right)^2 + \left(-\frac{1}{2} \times .009 \right)^2 \right]^{\frac{1}{2}} = \pm 0.004679 = \pm 0.4679\,\%$$

The dimension of CB and CH were measured with a vernier and found, CB $= 0.1524 \pm 0.00001$ m and CH $= 0.0762 \pm 0.00001$ m.

The uncertainty associated with CB is found:

$$\frac{w_{CB}}{CB} = \frac{0.00001}{0.1524} = \pm\, 0.0000656 = \pm\, 0.00656\,\%$$

The uncertainty associated with CH is found:

$$\frac{w_{CH}}{CH} = \frac{0.00001}{0.0762} = \pm\, 0.00013 = \pm\, 0.013\ \%$$

The uncertainty associated with V_d is found:

$$\frac{w_{V_d}}{V_d} = \left[\left(\frac{w_{\forall}}{\forall}\right)^2 + \left(-1\,.\,\frac{w_{CB}}{CB}\right)^2 + \left(-1\,.\,\frac{w_{CH}}{CH}\right)^2\right]^{\frac{1}{2}}$$

$$= \left[(0.004679)^2 + (-1 \times 0.0000656)^2 + (-1 \times 0.00013)^2\right]^{\frac{1}{2}}$$

$$\frac{w_{V_d}}{V_d} = \pm\, 0.0046813 = \pm\, 0.468\ \%$$

The uncertainty associated with V_d is $\pm$ 0.468 %

D.4 Uncertainties of Parameters after Data Reduction

Experimental data were reduced to Pressure Drop around heat sink (ΔP_{hs}), Duct Reynolds Number, (Re_d), Dimensionless Pressure Drop (C_D), Thermal Resistance (R_{th}), Convective Heat Transfer Coefficient (h), Nusselt Number (Nu_{2s}), and Entropy Generation (S_{gen}) .

D.4.1 Pressure Drop (ΔP_{hs})

The pressure drop around heat sink is measured by the following relationship:

$$\Delta P_{hs} = P_2 - P_1 = P_2 + (-1)\, P_1 \tag{D.31}$$

The uncertainty associated with ΔP_{hs} can be calculated using Eq. D.9:

$$w_{\Delta P_{hs}} = \left[(-1 \times w_{P_1})^2 + (w_{P_2})^2\right]^{\frac{1}{2}} \tag{D.32}$$

From subsection D.3.4, the uncertainty of P_1 is found:

$$\frac{w_{P_1}}{P_1} = \pm\, 0.0026$$

For $P_1 = 3.9$ Pa,

$$w_{P_1} = \pm\, 0.0026 \times 3.9 = \pm\, 0.01014\ Pa$$

From subsection D.3.4, the uncertainty of P_2 is found:

$$\frac{w_{P_2}}{P_2} = \pm\, 0.002586$$

For $P_2 = 6.57$ Pa,

$$w_{P_2} = \pm\, 0.002586 \times 6.57 = \pm\, 0.01699\ Pa$$

Substituting the value of w_{P_1} and w_{P_2} into Eq. D.32, the value of $w_{\Delta P_{hs}}$ is found:

$$w_{\Delta P_{hs}} = \left[(-1 \times 0.01014)^2 + (0.01699)^2\right]^{\frac{1}{2}} = \pm\, 0.019786\ \ [Pa]$$

Substituting the value of P_1 and P_2 into equation D.31, ΔP_{hs} is found:

$$\Delta P_{hs} = 6.57 - 3.9 = 2.67\ \ [Pa]$$

Therefore, the uncertainty associated with ΔP_{hs} is found:

$$\frac{w_{\Delta P_{hs}}}{\Delta P_{hs}} = \frac{0.019786}{2.67} = \pm\, 0.00741 = \pm\, 0.741\ \%$$

The uncertainty associated with ΔP_{hs} is found to be $\pm\, 0.741$ %.

D.4.2 Dimensionless Pressure Drop, C_D:

C_D is defined as:

$$C_D = \frac{\Delta P_{hs}}{\frac{1}{2}\,\rho_{air}\,{V_d}^2} = 2\,{\Delta P_{hs}}^1\,{\rho_{air}}^{-1}\,{V_d}^{-2} \tag{D.33}$$

Comparing with Eq. D.7, the uncertainty of C_D can be written as:

$$\frac{w_{C_D}}{C_D} = \left[\left(1.\frac{w_{\Delta P_{hs}}}{\Delta P_{hs}}\right)^2 + \left(-1.\frac{w_{\rho_{air}}}{\rho_{air}}\right)^2 + \left(-2.\frac{w_{V_d}}{V_d}\right)^2\right]^{\frac{1}{2}} \tag{D.34}$$

From subsection D.4.1,

$$\frac{w_{\Delta P_{hs}}}{\Delta P_{hs}} = \pm\, 0.00741$$

From subsection D.3.7,

$$\frac{w_{V_d}}{V_d} = \pm\, 0.0046813$$

From subsection D.3.5,

$$\frac{w_{\rho_{air}}}{\rho_{air}} = \pm\, 0.009$$

Substituting the values into Eq. D.34, the uncertainty of C_D is found:

$$\begin{aligned} \frac{w_{C_D}}{C_D} &= \left[(1\times 0.00741)^2 + (-1\times 0.009)^2 + (-2\times 0.0046813)^2\right]^{\frac{1}{2}} \\ &= \pm 0.014952 = \pm 1.5\% \end{aligned}$$

The uncertainty associated with Dimensionless Pressure Drop is $\pm$ 1.5 %.

D.4.3 Duct Reynolds Number (Re_d)

Re_d is defined by:

$$Re_d = \frac{\rho_{air} V_d D_{h_d}}{\mu} = {\rho_{air}}^1 {V_d}^1 {D_{h_d}}^1 \mu^{-1} \tag{D.35}$$

Comparing with Eq. D.7, the uncertainty of Re_d can be written as:

$$\frac{w_{Re_d}}{Re_d} = \left[\left(1.\frac{w_{\rho_{air}}}{\rho_{air}}\right)^2 + \left(1.\frac{w_{V_d}}{V_d}\right)^2 + \left(1.\frac{w_{D_{h_d}}}{D_{h_d}}\right)^2 + \left(-1.\frac{w_{\mu_{air}}}{\mu_{air}}\right)^2\right]^{\frac{1}{2}} \tag{D.36}$$

From subsection D.3.5,

$$\frac{w_{\rho_{air}}}{\rho_{air}} = \pm\, 0.009$$

From subsection D.3.7,

$$\frac{w_{V_d}}{V_d} = \pm\, 0.0046813$$

From subsection D.3.6,

$$\frac{w_{\mu_{air}}}{\mu_{air}} = \pm\, 0.0063$$

The hydraulic Diameter of duct (Dh_d) may be defined as:

$$D_{h_d} = \frac{4.A_d}{P_d} = 4.{A_d}^1 {P_d}^{-1} \tag{D.37}$$

Comparing with Eq. D.7, the uncertainty of D_{h_d} can be written as:

$$\frac{w_{D_{h_d}}}{D_{h_d}} = \left[\left(1.\frac{w_{A_d}}{A_d}\right)^2 + \left(-1.\frac{w_{P_d}}{P_d}\right)^2\right]^{\frac{1}{2}} \tag{D.38}$$

The area of the duct (A_d) is defined by:

$$A_d = CB \times CH \tag{D.39}$$

Comparing with Eq. D.7, the uncertainty of A_d can be written as:

$$\frac{w_{A_d}}{A_d} = \left[\left(\frac{w_{CB}}{CB}\right)^2 + \left(\frac{w_{CH}}{CH}\right)^2\right]^{\frac{1}{2}} \tag{D.40}$$

From subsection D.3.7,

$$\frac{w_{CB}}{CB} = \pm 0.0000656 \ \ and \ \ \frac{w_{CH}}{CH} = \pm 0.00013$$

Therefore, the uncertainty of A_d is found:

$$\frac{w_{A_d}}{A_d} = \left[(0.0000656)^2 + (0.00013)^2\right]^{\frac{1}{2}} = \pm\, 0.000146 = \pm\, 0.0146\,\%$$

The perimeter of duct ($\mathcal{P}_d$) is defined by:

$$\mathcal{P}_d = 2\,(CB + CH) \tag{D.41}$$

Comparing with Eq. D.9, the uncertainty of $\mathcal{P}_d$ can be written as:

$$w_{\mathcal{P}_d} = \left[(2.w_{CB})^2 + (2.w_{CH})^2\right]^{\frac{1}{2}} \tag{D.42}$$

w_{CB} and w_{CH} are found from the accuracy of the vernier:

$$w_{CB} = w_{CH} = \pm\, 0.00001 \ \ m$$

Substituting these values in Eq. D.42:

$$w_{\mathcal{P}_d} = \left[(2 \times 0.00001)^2 + (2 \times 0.00001)^2\right]^{\frac{1}{2}} = \pm\, 0.000028$$

For this sample calculation, the duct configuration is:

$$CB = 0.1524\,m \text{ and } CH = 0.0762\,m$$

Using Eq. D.41, $\mathcal{P}_d$ is found:

$$\mathcal{P}_d = 2\,.\,(0.1524 + 0.0762) = .4572\,m$$

The uncertainty of $\mathcal{P}_d$ is calculated as:

$$\frac{w_{\mathcal{P}_d}}{\mathcal{P}_d} = \frac{0.000028}{0.4572} = \pm\, 0.000062 = \pm\, .0062\ \%$$

Substituting the uncertainty of A_d and P_d into Eq. D.38, the uncertainty of D_{h_d} is found:

$$\begin{aligned} \frac{w_{D_{h_d}}}{D_{h_d}} &= \left[(1\times 0.000146)^2 + (-1\times 0.000062)^2\right]^{\frac{1}{2}} \\ &= \pm\, 0.000159 = \pm\, 0.0159\ \% \end{aligned}$$

Substituting the uncertainty of ρ_{air}, V_d, D_{h_d} and μ_{air} in Eq. D.36, the uncertainty of Re_d is found:

$$\begin{aligned} \frac{w_{Re_d}}{Re_d} = \Big[&(1\times 0.009)^2 + (1\times 0.0046813)^2 \\ &+ (1\times 0.000159)^2 + (-1\times 0.0063)^2\Big]^{\frac{1}{2}} \end{aligned}$$

$$\frac{w_{Re_d}}{Re_d} = \pm\, 0.007901 = \pm\, 0.79\ \%$$

The uncertainty associated with duct Reynolds number is found to be $\pm$ 0.79 %

D.4.4 Thermal Resistance (R_{th})

R_{th} is defined by:

$$R_{th} = \frac{T_b - T_a}{Q} = \frac{\Delta T}{Q} = \Delta T^1\, Q^{-1} \tag{D.43}$$

Comparing with Eq. D.7, the uncertainty of R_{th} can be written as:

$$\frac{w_{R_{th}}}{R_{th}} = \left[\left(\frac{w_{\Delta T}}{\Delta T}\right)^2 + \left(-1\times\frac{w_Q}{Q}\right)^2\right]^{\frac{1}{2}} \tag{D.44}$$

ΔT is defined as:

$$\Delta T = T_b - T_a = T_b + (-1)\, T_a \tag{D.45}$$

Comparing with Eq. D.9, the uncertainty of ΔT can be written as:

$$w_{\Delta T} = \left[(-1 \times w_{T_a})^2 + (w_{T_b})^2\right]^{\frac{1}{2}} \tag{D.46}$$

The uncertainty associated with T_a and T_b were found from the accuracy of T-thermocouples:

$$w_{T_a} = w_{T_b} = \pm\, 0.2\ {}^0C$$

Substituting the value of w_{T_a} and w_{T_b} into Eq. D.46, $w_{\Delta T}$ is found:

$$w_{\Delta T} = \left[(0.2)^2 + (0.2)^2\right]^{\frac{1}{2}} = \pm\, 0.28\ {}^0C$$

From the experiment, ΔT is found:

$$\Delta T = T_b - T_a = 28.6 - 21.8 = 6.8\ {}^0C$$

The uncertainty of ΔT is found:

$$\frac{w_{\Delta T}}{\Delta T} = \frac{0.28}{6.8} = \pm 0.041595 = \pm 4.2\ \%$$

Heat is supplied to the resistance heater by supplying current through a power supply, and supplied heat Q (50 Watt) is defined by the following relationship:

$$Q = V \times I \tag{D.47}$$

Comparing with Eq. D.7, the uncertainty of Q can be written as:

$$\frac{w_Q}{Q} = \left[\left(\frac{w_V}{V}\right)^2 + \left(\frac{w_I}{I}\right)^2\right]^{\frac{1}{2}} \tag{D.48}$$

The uncertainty of V and I are found from subsubsection D.3.2 and D.3.3 respectively:

$$\frac{w_V}{V} = \pm\, 7.8 \times 10^{-5} \ \textit{and}\ \frac{w_I}{I} = \pm\, 0.0012$$

Substituting these values into Eq. D.48, the uncertainty of Q is found:

$$\frac{w_Q}{Q} = \left[\left(7.8 \times 10^{-5}\right)^2 + (0.0012)^2\right]^{\frac{1}{2}} = \pm\, 0.0012 = \pm\, 0.12\ \%$$

The uncertainty of R_{th} is found by substituting the uncertainty of ΔT and Q into Eq. D.49:

$$\frac{w_{R_{th}}}{R_{th}} = \left[0.041595^2 + (-1 \times 0.0012)^2\right]^{\frac{1}{2}} = \pm\, 0.041612 = \pm\, 4.16\ \%$$

The uncertainty in thermal resistance is found to be $\pm$ 4.16 %

D.4.5 Convective Heat Transfer Coefficient, h

The convective heat transfer coefficient is calculated from Newton's Law of Cooling:

$$Q = h\, A_s\ (T_b - T_a) \tag{D.49}$$

$$h = \frac{1}{A_s} \times \frac{Q}{T_b - T_a} = \frac{1}{A_s} \times \frac{1}{R_{th}} = {A_s}^{-1}\, {R_{th}}^{-1} \tag{D.50}$$

Comparing with Eq. D.7, the uncertainty associated with h can be written as:

$$\frac{w_h}{h} = \left[\left(-1\ \times\ \frac{w_{A_s}}{A_s}\right)^2 + \left(-1\ \times\ \frac{w_{R_{th}}}{R_{th}}\right)^2\right]^{\frac{1}{2}} \tag{D.51}$$

From subsection D.4.4,

$$\frac{w_{R_{th}}}{R_{th}} = \pm\, 0.041612$$

Convective heat transfer area A_s is defined as:

$$A_s = 2\, N\, A_f + (N-1)\ A_b \tag{D.52}$$

As $N = 28$ for this experiment, the equation D.57 becomes:

$$A_s = 56\, A_f + 27\, A_b \tag{D.53}$$

Using Eq. D.9, The uncertainty associated with A_s can be written as:

$$w_{A_s} = \left[\left(56\, w_{A_f}\right)^2 + \left(27\, w_{A_b}\right)^2\right]^{\frac{1}{2}} \tag{D.54}$$

A_f is defined as:

$$A_f = L \times H \tag{D.55}$$

Using Eq. D.7, the uncertainty associated with A_f can be written as:

$$\frac{w_{A_f}}{A_f} = \left[\left(\frac{w_L}{L}\right)^2 + \left(\frac{w_H}{H}\right)^2\right]^{\frac{1}{2}} \tag{D.56}$$

The uncertainty associated with L and H are found from the accuracy of the vernier:

$$w_L = w_H = \pm\, 0.00001\ m$$

The value of L and H are measured:

$$L = 0.1016\ m \quad \text{and} \quad H = 0.05\ m$$

The uncertainty of L and H were found:

$$\frac{w_L}{L} = \pm\, 0.000098 = \pm\, 0.0098\,\% \quad \text{and} \quad \frac{w_H}{H} = \pm\, 0.0002 = \pm\, 0.02\,\%$$

Using Eq. D.56, the uncertainty of A_f is calculated as:

$$\frac{w_{A_f}}{A_f} = \left[0.000098^2 + 0.0002^2\right]^{\frac{1}{2}} = \pm\, 0.000223 = \pm\, 0.0223\,\%$$

From heat sink geometry, A_f is found:

$$A_f = 0.1016 \times 0.05 = 0.00508 \quad [m^2]$$

Therefore, w_{A_f} is found:

$$w_{A_f} = 0.000223 \times 0.00508 = \pm\, 0.00000113 \quad [m^2]$$

A_b is defined as:

$$A_b = L \times s \tag{D.57}$$

Using Eq. D.7, the uncertainty associated with A_b can be written as:

$$\frac{w_{A_b}}{A_b} = \left[\left(\frac{w_L}{L}\right)^2 + \left(\frac{w_s}{s}\right)^2\right]^{\frac{1}{2}} \tag{D.58}$$

The uncertainty associated with L and s are found from the accuracy of the vernier:

$$w_L = w_s = \pm\, 0.00001\ m$$

The value of L and s are measured:

$$L = 0.1016\ m \quad \text{and} \quad s = 0.0025\ m$$

The uncertainty of L and s are found:

$$\frac{w_L}{L} = \pm\, 0.000098 = \pm\, 0.0098\,\% \quad \text{and} \quad \frac{w_s}{s} = \pm\, 0.004 = \pm\, 0.40\,\%$$

Using Eq. D.58, the uncertainty of A_b is calculated as:

$$\frac{w_{A_b}}{A_b} = \left[0.000098^2 + 0.004^2\right]^{\frac{1}{2}} = \pm\, 0.004001 = \pm\, 0.4001\,\%$$

From heat sink geometry, A_b is found:

$$A_b = 0.1016 \times 0.0025 = 0.000254 \quad [m^2]$$

Therefore, w_{A_b} is measured:

$$w_{A_b} = 0.004 \times 0.000254 = \pm\, 0.00000102 \quad [m^2]$$

Substituting the value of w_{A_f} and w_{A_b} into Eq. D.54, the value of w_{A_s} is found:

$$w_{A_s} = \left[(56 \times 0.00000113)^2 + (27 \times 0.00000102)^2\right]^{\frac{1}{2}} = \pm\, 0.000069 \quad [m^2]$$

Substituting the value of A_f and A_b into Eq. D.53, the value of A_s is found:

$$A_s = 56 \times 0.00508 + 27 \times 0.000254 = 0.291338 \quad [m^2]$$

The uncertainty of A_s is found:

$$\frac{w_{A_s}}{A_s} = \frac{0.000069}{0.291338} = \pm\, 0.00023716 = \pm\, 0.0237\,\%$$

Substituting the uncertainty of A_s and R_{th} into Eq. D.51, the uncertainty of h is found:

$$\frac{w_h}{h} = \left[(-1 \times 0.00023716)^2 + (-1 \times 0.041612)^2\right]^{\frac{1}{2}} = \pm\, 0.041613 = \pm\, 4.16\,\%$$

The uncertainty in Convective Heat Transfer Coefficient is found to be $\pm$ 4.16 %

D.4.6 Nusselt Number (Nu_{2s})

Nusselt number is defined by:

$$Nu_{2s} = \frac{hD_{h_{ch}}}{k_{air}} \tag{D.59}$$

where k_{air} is assumed constant.

Using Eq. D.7, the uncertainty associated with Nu_{2s} can be written as:

$$\frac{w_{Nu_{2s}}}{Nu_{2s}} = \left[\left(\frac{w_h}{h}\right)^2 + \left(\frac{w_{D_{h_{ch}}}}{D_{h_{ch}}}\right)^2\right]^{\frac{1}{2}} \tag{D.60}$$

From subsubsection D.4.5, the uncertainty of h is found:

$$\frac{w_h}{h} == \pm 0.041613$$

$D_{h_{ch}}$ is defined by:

$$D_{h_{ch}} = \frac{4A_{ch}}{P_{ch}} = \frac{4s \times H}{2 \times H + s} \tag{D.61}$$

As $H \gg s$, Eq. D.61 can be written as:

$$D_{h_{ch}} = 2 \times s \tag{D.62}$$

The uncertainty associated with $D_{h_{ch}}$ is:

$$\frac{w_{D_{h_{ch}}}}{D_{h_{ch}}} = \frac{w_s}{s} \tag{D.63}$$

The uncertainty associated with s is found from the accuracy of the vernier:

$$w_s = \pm 0.00001\ m$$

From heat sink geometry, s is found:

$$s = 0.0025 \quad [m]$$

The uncertainty associated with $D_{h_{ch}}$ is found:

$$\frac{w_{D_{h_{ch}}}}{D_{h_{ch}}} = \frac{0.00001}{0.0025} = \pm 0.004 = \pm 0.40\,\%$$

Substituting the uncertainty of h and $D_{h_{ch}}$ into Eq. D.60, the uncertainty of Nu_{2s} is calculated as:

$$\frac{w_{Nu_{2s}}}{Nu_{2s}} = \left[(0.041613)^2 + (0.004)^2\right]^{\frac{1}{2}} = \pm 0.041804 = \pm 4.18\,\%$$

The uncertainty in Nusselt Number is found to be $\pm$ 4.18 %

D.4.7 Entropy Generation ($\mathcal{S}_{gen}$)

$\mathcal{S}_{gen}$ is defined as:

$$\mathcal{S}_{gen} = \mathcal{S}_{fl} + \mathcal{S}_{th} \tag{D.64}$$

Using Eq. D.7, uncertainty associated with $\mathcal{S}_{gen}$ can be written as:

$$w_{\mathcal{S}_{gen}} = \left[{w_{\mathcal{S}_{fl}}}^2 + {w_{\mathcal{S}_{th}}}^2 \right]^{\frac{1}{2}} \tag{D.65}$$

Uncertainty of Hydrodynamic Entropy Generation, $\mathcal{S}_{fl}$:

$\mathcal{S}_{fl}$ is defined as:

$$\mathcal{S}_{fl} = \frac{\Delta P_{hs} \times \forall_d}{T_a} = \Delta P_{hs}^1 \ {\forall_d}^1 \ {T_a}^{-1} \tag{D.66}$$

Using Eq. D.7, uncertainty associated with $\mathcal{S}_{fl}$ can be written as:

$$\frac{w_{\mathcal{S}_{fl}}}{\mathcal{S}_{fl}} = \left[\left(\frac{1 \times w_{\Delta P_{hs}}}{\Delta P_{hs}} \right)^2 + \left(1 \times \frac{w_{\Delta \forall_d}}{\Delta \forall_d} \right)^2 + \left(-1 \times \frac{w_{\Delta T_a}}{\Delta T_a} \right)^2 \right]^{\frac{1}{2}} \tag{D.67}$$

From subsection D.4.1, $\Delta P_{hs} = 2.67 \ \ [Pa]$ and $\frac{w_{\Delta P_{hs}}}{\Delta P_{hs}} = \pm\, 0.00741 = \pm\, 0.741 \ \%$

From subsection D.3.7, $\forall_d = 0.023253912 \ \ [m/s]$ and $\frac{w_{\forall}}{\forall} = \pm 0.004679 = \pm 0.4679\,\%$

From subsection D.3.1, $T_a = 294.8 \ K$ and $\frac{w_{T_a}}{T_a} = \pm 0.009 = \pm 0.9 \ \%$

Substituting these values in Eq. D.67:

$$\frac{w_{\mathcal{S}_{fl}}}{\mathcal{S}_{fl}} = \left[0.00741^2 + 0.004679^2 + 0.009^2 \right]^{\frac{1}{2}} = \pm 0.012562 = \pm 1.26\,\%$$

Using Eq. D.66:

$$\mathcal{S}_{fl} = \frac{2.67 \times 0.023253912}{294.8} = 0.00021 \ \ \left[\frac{Watt}{K} \right]$$

$w_{\mathcal{S}_{fl}}$ is found:

$$w_{\mathcal{S}_{fl}} = 0.012562 \times 0.00021 = \pm\, 2.638 \times 10^{-6} \ \ \left[\frac{Watt}{K} \right]$$

Uncertainty of Thermal Entropy Generation, $\mathcal{S}_{th}$:

$\mathcal{S}_{th}$ is defined as:

$$\mathcal{S}_{th} = \frac{Q^2 \times R_{th}}{T_a{}^2} = Q^2 \; {R_{th}}^1 \; {T_a}^{-2} \tag{D.68}$$

Using Eq. D.7, the uncertainty associated with $\mathcal{S}_{th}$ can be written as:

$$\frac{w_{\mathcal{S}_{th}}}{\mathcal{S}_{th}} = \left[\left(2 \times \frac{w_Q}{Q} \right)^2 + \left(1 \times \frac{w_{R_{th}}}{R_{th}} \right)^2 + \left(-2 \times \frac{w_{T_a}}{T_a} \right)^2 \right]^{\frac{1}{2}} \tag{D.69}$$

From subsection D.4.4:

$$Q = 50 \;\; [\mathrm{W}]; \qquad \frac{w_Q}{Q} = \pm\, 0.0012 = \pm\, 0.12\ \%;$$

$$R_{th} = 0.136 \;\; \left[\frac{K}{W} \right]; \; \frac{w_{R_{th}}}{R_{th}} = \pm\, 0.041612 = \pm\, 4.16\ \%$$

From subsection D.3.1,

$$T_a = 294.8\ K; \; \frac{w_{T_a}}{T_a} = \pm 0.009 = \pm 0.9\ \%$$

Substituting these values in Eq. D.69:

$$\frac{w_{\mathcal{S}_{th}}}{\mathcal{S}_{th}} = \left[(2 \times 0.0012)^2 + (0.041612)^2 + (-2 \times 0.009)^2 \right]^{\frac{1}{2}} = \pm 0.0454 = \pm 4.54\,\%$$

Using Eq. D.68:

$$\mathcal{S}_{th} = \frac{50^2 \times 0.136}{294.8^2} = 0.003912 \;\; \left[\frac{W}{K} \right]$$

$w_{\mathcal{S}_{th}}$ is found:

$$w_{\mathcal{S}_{th}} = 0.0454 \times 0.003912 = \pm\ 1.78 \times 10^{-4} \;\; \left[\tfrac{W}{K} \right]$$

Using Eq. D.64, $\mathcal{S}_{gen}$ is found:

$$\mathcal{S}_{gen} = 0.00021 + 0.003912 = 0.004122 \;\; \left[\frac{W}{K} \right]$$

substituting $w_{\mathcal{S}_{fl}}$ and $w_{\mathcal{S}_{th}}$ into Eq. D.65, $w_{\mathcal{S}_{gen}}$ is found:

$$w_{\mathcal{S}_{gen}} = \left[\left(2.638 \times 10^{-6} \right)^2 + \left(1.78 \times 10^{-4} \right)^2 \right]^{\frac{1}{2}} = \pm 0.0001803 \;\; \left[\frac{W}{K} \right]$$

The uncertainty in $\mathcal{S}_{gen}$ is found:

$$\frac{w_{\mathcal{S}_{gen}}}{\mathcal{S}_{gen}} = \frac{0.0001803}{0.004122} = \pm 0.04374 = \pm 4.374\%$$

The Uncertainty associated with Entropy Generation is found to be $\pm$ 4.37%.

The uncertainty associated with experimental data of ΔP_{hs}, R_{th} and $\mathcal{S}_{gen}$ are shown in Table D.1.

Table D.1: Experimental Uncertainties

B mm	CB mm	H mm	CH mm	V_d $\frac{m}{s}$	Uncertainty (%)		
					ΔP_{hs}	R_{th}	$\mathcal{S}_{gen}$
100	100	50	50	1	0.33	2.06	4.57
				1.5	0.34	3.05	6.56
				2	0.36	3.82	7.82
				2.5	0.36	4.49	8.45
				3	0.37	4.95	8.39
100	125	50	62.5	1	0.39	2.03	4.50
				1.5	0.40	3.10	6.71
				2	0.40	4.01	8.21
				2.5	0.41	4.76	8.89
				3	0.42	5.36	8.81
100	150	50	75	1	0.75	1.66	3.70
				1.5	0.72	2.61	5.69
				2	0.71	3.49	7.27
				2.5	0.71	4.19	8.09
				3	0.72	4.76	8.24
100	175	50	87.5	1	1.14	1.44	3.22
				1.5	0.93	2.89	6.23
				2	0.87	3.68	7.47
				2.5	0.93	4.49	8.36
				3	0.97	4.73	8.00